



City Research Online

City, University of London Institutional Repository

Citation: Zhang, K. (2017). Turbulent combustion simulation in realistic gas-turbine combustors. (Unpublished Doctoral thesis, City, University of London)

This is the draft version of the paper.

This version of the publication may differ from the final published version.

Permanent repository link: <https://openaccess.city.ac.uk/id/eprint/17689/>

Link to published version:

Copyright: City Research Online aims to make research outputs of City, University of London available to a wider audience. Copyright and Moral Rights remain with the author(s) and/or copyright holders. URLs from City Research Online may be freely distributed and linked to.

Reuse: Copies of full items can be used for personal research or study, educational, or not-for-profit purposes without prior permission or charge. Provided that the authors, title and full bibliographic details are credited, a hyperlink and/or URL is given for the original metadata page and the content is not changed in any way.



**School of Mathematics,
Computer Science and
Engineering**

**Turbulent Combustion Simulation in Realistic Gas-
Turbine Combustors**

by

Kai Zhang

Thesis Submitted for the Degree of Doctor of Philosophy
in the Mechanical Engineering and Aeronautics
Department

City, University of London

May 2017

TABLE OF CONTENTS

TABLE OF CONTENTS.....	2
LIST OF FIGURES	6
LIST OF TABLES	10
ACKNOWLEDGEMENTS.....	11
DECLARATION.....	12
ABSTRACT	13
NOMENCLATURE.....	15
Chapter 1 Introduction.....	22
1.1 Motivation	22
1.2 The Gas Turbine in Power Generation Industry and Aviation.....	24
1.3 CFD in Gas Turbine Combustor	30
1.4 Current Contribution	33
1.5 Thesis Outline	35
Chapter 2 Literature Review	38
2.1 Introduction	38
2.2 Combustion Research Work in Simple Combustor-like Burners	39
2.2.1 Experimental and numerical work.....	39
2.2.2 Summary of research work on turbulent jet flames.....	50

2.3 Combustion Research Works in Realistic Gas Turbine Combustor	
Geometry	52
2.4 Turbulent Flow Simulations	61
2.5 Overall Summary	68
Chapter 3 Mathematical Model	71
3.1 Introduction	71
3.2 Turbulence Models	73
3.2.1 SSTKW model	73
3.2.2 Reynolds stress model (RSM)	75
3.2.3 SST k-omega scale-adaptive simulation (SSTKWSAS)	76
3.3 Combustion Models	78
3.3.1 Mixture fraction theory	78
3.3.2 Laminar flamelet theory (LFM)	81
3.3.3 Presumed probability density function (Presumed PDF)	84
3.3.4 Non-premixed combustion discipline	88
3.3.5 Partially-premixed combustion discipline	90
Chapter 4 Numerical Methods and Experimental	
Configurations	96
4.1 Numerical Methods	96
4.2 Experimental Configurations	100
4.3 Reaction Mechanism and Look-Up Table	104

Chapter 5 Combustion Simulation in a Representative Rich Burn Gas Turbine Combustor	106
5.1 Introduction	106
5.2 Behaviour of Flow Field and Scalar Variables	107
5.3 Statistical Results	116
5.4 Conclusions	121
Chapter 6 Turbulence Modelling in a Representative Rich Burn Gas Turbine Combustor	123
6.1 Introduction	123
6.2 Behaviour of Flow Field and Scalar Variables	124
6.3 Statistical Results	137
6.4 Conclusions	141
Chapter 7 Closure: Conclusions and Recommendations	143
7.1 Summary	143
7.2 Overall Conclusions	144
7.3 Recommendations for Future Work.....	145
REFERENCE LIST	147
APPENDIX A	169
APPENDIX B.....	174
APPENDIX C	180

APPENDIX D183

APPENDIX E.....197

LIST OF FIGURES

Figure 1.1: Power Jets W.1, Type: Turbojet [2].	25
Figure 1.2: J-series gas turbine developed by Mitsubishi Heavy Industries, Ltd [3].	25
Figure 1.3: Rolls-Royce Trent 900 engines, Type: Turbofan [4].	26
Figure 1.4: Modern Gas Turbine, Type: Turbojet [5].	26
Figure 1.5: Modern Gas Turbine, Type: Turboprop [6].	26
Figure 1.6: Modern Gas Turbine, Type: Turbofan [7].	27
Figure 1.7: Modern Gas Turbine, Type: Afterburner Turbojet [8].	28
Figure 1.8: Can-annular type gas turbine combustor [9].	29
Figure 1.9: Annular type gas turbine combustor [10].	29
Figure 1.10: A modern meshing method applied on Racing Car [11].	31
Figure 2.1: Laminar flamelet in a typical turbulent flame.	40
Figure 2.2: Turbulence and stretch effect on laminar flamelet. Red vertical lines represent the effect of turbulence/PDF, various peaks of parabolic curves represents the effect of stretch/strain rate.	42
Figure 2.3: A sample laminar flamelet under the effect of turbulence.	43
Figure 2.4: Left: Piloted flame [44]. Right: Sketch of a test facility for the swirling flame of SM1 and SM2 [45].	45
Figure 2.5: A typical swirling flame [62].	46
Figure 2.6: A typical lifted flame [65].	47
Figure 2.7: Sketch of the several combustors in past experimental works [100-102].	54

Figure 2.8: (a) Experimental layout of model Tay [114]. (b) Realistic experimental setup [109-111].	55
Figure 2.9: Air flow split of the model Tay combustor. (a) Small swirler configuration [114]. (b) Large swirler configuration [109-111].	57
Figure 2.10: Velocity streakline with and without the fuel injector component sitting on the cone section of the can type gas turbine combustor. (a) Without fuel injector. (b) With fuel injector [115].	59
Figure 2.11: Temperature distributions from: (left) prediction (five levels between pink = 2200K and blue = 315K) [115], (right) experiment [114].	61
Figure 2.12: SSTKWSAS simulation for ITS combustion chamber. Top: Configuration. Bottom left: Q-criterion of Non-reacting flow. Bottom right: Q-criterion of Reacting flow [136].	65
Figure 2.13: Q-criterion contour plot for aerodynamic flow, left: SSTKW model. Right: SSTKWSAS model [136].	66
Figure 3.1: Laminar flamelet iso-surface, mixture fraction space.	82
Figure 3.2: Probability density function definition.	85
Figure 3.3: Regime diagram for non-premixed combustion [148].	88
Figure 3.4: Regime diagram for premixed combustion [149].	92
Figure 3.5: Laminar flame speed vs. mixture fraction [152].	93
Figure 4.1: Hexahedral mesh of geometry.	97
Figure 4.2: Grid independence study.	98
Figure 4.3: Configuration of model can type combustor.	100
Figure 4.3: (Continued).	101
Figure 4.4: Relationship between temperature and mixture fraction at different scalar dissipation.	105

Figure 5.1: Streaklines of flow field coloured by mixture fraction. (a) ZTFSC model, (b) Non-premixed model, (c) ECFM model. Black solid line: stoichiometric mixture fraction=0.0639.....	108
Figure 5.1: (Continued).....	109
Figure 5.2: Intensity of CRZ in primary region represented by vorticity = 9776.83/s for (a) ZTFSC model, (b) ECFM model.....	110
Figure 5.2: (Continued).....	111
Figure 5.3: Progress variable (reaction progress) contour. (a) ZTFSC model, (b) Non-premixed model, (c) ECFM model.....	112
Figure 5.4: Temperature contours at axial position of 20mm, 50mm, 80mm, 130mm, and exit of combustor 210mm. (a) ZTFSC model, (b) Non-premixed model, (c) ECFM model.....	113
Figure 5.4: (Continued).....	114
Figure 5.5: Temperature in the primary zone: horizontal midplane. (a) ZTFSC & RSM model, (b) LES & Non-premixed model, Colour scale: five levels between pink = 2200K and blue = 315K [115].....	115
Figure 5.6: Profile of temperature and mixture fraction in the horizontal midplane of the combustor.....	118
Figure 5.7: Profile of species mole fraction in the horizontal midplane of combustor (x=20mm).	119
Figure 5.7: (Continued).....	120
Figure 6.1: Instantaneous iso-surface of swirling strength = 2222.24/s (Left) and statistically averaged reaction progress contours (right). (a) and (b): SSTKW. (c) and (d): RSM. (e) and (f): SSTKWSAS.	125

Figure 6.2: Mean of mixture fraction on horizontal midplane of combustor (y=0mm) (a) SSTKW, (b) RSM, (c) SSTKWSAS.....	126
Figure 6.2: (Continued).....	127
Figure 6.3: Instantaneous streakline plots of PVC at 2222.24/s and 4444.48/s. (a) and (b): SSTKW. (c) and (d): RSM. (e) and (f): SSTKWSAS.	128
Figure 6.3: (Continued).....	129
Figure 6.3: (Continued).....	130
Figure 6.4: Time-mean temperature contours on horizontal midplane of combustor (y=0mm) (a) SSTKW, (b) RSM, (c) SSTKWSAS.....	131
Figure 6.5: Instantaneous streakline plots of PVC at 4444.48/s (SSTKWSAS).	132
Figure 6.5: (Continued).....	133
Figure 6.6: Instantaneous temperature field at horizontal midplane (SSTKWSAS).....	135
Figure 6.6: (Continued).....	136
Figure 6.7: Profile of temperature and mixture fraction in the horizontal midplane of the combustor (y=0mm).	139
Figure 6.8: Profile of species mole fraction in the horizontal midplane of combustor.....	139
Figure 6.8: (Continued).....	140

LIST OF TABLES

Table 3.1: Boundary conditions for passive scalars.....	80
Table 3.2: A look-up table to correlate mean quantities with mean mixture fraction and its variance	87
Table 4.1: Experimental conditions [114].	104
Table 4.2: Numerical boundary conditions.....	104

ACKNOWLEDGEMENTS

Firstly, I would like to express my sincere gratitude to my co-supervisor Professor Ali Ghobadian for his continuous professional and priceless support during the time towards the completion of my Ph.D. His deep insights helped me in all the time of research and writing of this thesis. Without his unfailing support and patience, I would not be able to see the glorious landscape of the world of turbulence combustion.

I would also like to give my special thanks to Prof Jamshid Nouri as my main supervisor who gave me the opportunity to carry out my doctoral research and for the financial support by providing me with the part-time teaching position at City, University of London. His smile and encouragement have assisted me in overcoming many difficulties met during my Ph.D. study.

My heartfelt thanks to all members of my family, my father, mother and young brother for their continuous support and solicitude. Finally, I must express my very profound gratitude to my wife Minghui Yu for accompanying with me in the last ten years and for giving birth to my lovely son in the final year of my Ph.D. study.

London, March 2017.

DECLARATION

I hereby declare that the presented work in this thesis is my own or was developed in a joint effort with other members of the research group as it is stated and referenced in the text accordingly!

I grant powers of discretion to the University Librarian to allow this thesis to be copied in whole or in part without further reference to me. This permission covers only single copies made for study purposes, subject to normal conditions of acknowledgment.

London

(Kai Zhang)

ABSTRACT

The work presented in this thesis addresses issues involving the accurate and efficient numerical modelling of turbulence combustion with an emphasis on an industrially representative Tay model combustor. This combustor retained all essential features of a modern aero-engine rich burn combustor and thus the turbulence combustion within this combustor is much more complicated than those observed in the combustor-like burners typically considered in laboratory experiments.

A comparative study of two combustion models based on a non-premixed assumption or a partially premixed assumption using the previously proposed models Zimont Turbulent Flame Speed Closure (ZTFSC) and Extended Coherent Flamelet Method (ECFM)) is presented in a first step. Comprehensive chemical reactions containing 244 reactions and 50 species are taken into account using a tabulated detailed chemistry approach and an assumed shape PDF to account for turbulence effects. The purpose of this study is to validate and compare the effectiveness of these models in predicting complex combustion and to improve upon for the defects observed in previous predictions of the same combustor. It is concluded that the use of models invoking the partially premixed combustion assumption can provide much more accurate results than models using a non-premixed combustion assumption especially in the primary zone of the combustor where turbulence combustion interaction is strong. In addition, certain shortcomings of steady RANS type models are identified as a result of strong unsteady effects and their inability to resolve the turbulence spectrum.

Following this, two URANS models and the scale resolving simulation (SRS) approach such as a shear stress transport, K-omega, scale adaptive simulation (SSTKWSAS) combined with the partially premixed method identified in the first step are employed in a second step to further improve the accuracy achieved and to provide evidence and guidance in terms of the trade-off between accuracy and computational cost for complex turbulent combustion simulations. The second generation SRS model (SSTKWSAS) is applied to the complicated flow environment of a realistic combustor for the first time. The present work highlights the superiority of the combination of the SSTKWSAS approach and a partially premixed combustion model in terms of both accuracy and efficiency for predicting such combustion problems.

NOMENCLATURE

ABBREVIATIONS

CFD	Computation fluid dynamic
SRS	Scale resolving simulation
RAF	British air force
PDE	Partial differential equations
FPVA	Flamelet/progress variable approach
ZTFSC	Zimont Turbulent Flame Speed Closure
ECFM	Extended Coherent Flamelet Method
LES	Large eddy simulation
CMC	Conditional Moment Closure
PDF	Probability density function
JPDF	Joint probability density function
TJPDF	Transported joint probability density function
IEM	Interaction by exchange with the mean
LMSR	Linear mean-square estimation
MC	Modified curl
EMST	Euclidean minimum spanning tree
SLFM	Steady laminar flamelet method
USLFM	Unsteady laminar flamelet method
SM	Swirling methane flame
CNG	Compressed natural gas
WRZ	Wall recirculation zone
CRZ	Centre recirculation zone
RSM	Reynolds stress model
DES	Detached eddy simulation

RANS	Reynolds averaged Navier-Stokes
URANS	Unsteady reynolds averaged Navier-Stokes
SAS	Scale adaptive simulation
KSKL	K square root KL model
SSTKWSAS	Shear stress transport, K-omega, scale adaptive simulation
KW	K-omega model
KE	K-epsilon model
3D	Three-Dimensional
LFA	Laminar flamelet assumption
TFS	Turbulent flame speed
ISP	Intermediate Steady Propagation
SSTKW	Shear stress transport, K-omega
FADM	Flame area density method
BCD	Bounded central differencing
CFL	Courant–Friedrichs–Lewy
Pre-PDF	Presumed probability density function
PVC	Precessing vortex core
AFR	Air-fuel ratio

SYMBOLS

ϕ	Conserved quantities
ϕ_b	Burnt species mass fraction
ϕ_u	Unburnt species mass fraction
ρ	Density
θ	Vane angle
θ'	Calculated vane angle
ρ_u	Unburnt density
\vec{u}	Velocity vector
u_k	Summation notation of 3D velocity
$\overline{u_k}$	Reynolds averaged summation notation of 3D velocity
τ_{ij}	Reynolds stress tensor
μ_t	Fictitious turbulent eddy viscosity
k	Turbulent kinetic energy
w	Turbulent dissipation rate
δ_{ij}	Kronecker delta
$\overline{u'Z'}$	Reynolds averaged 'Turbulent scalar flux'
$\overline{u'_i u'_j}$	Reynolds averaged 'Reynolds stress'
\bar{u}	Reynolds averaged velocity
$\alpha_{..}$	Turbulent diffusivity/thermal diffusivity
$\sigma_{..}$	Turbulent Prandtl number
G_k	Turbulent kinetic energy generation
G_w	Turbulent dissipation rate generation
Y_k	Dissipation of turbulent kinetic energy
Y_w	Dissipation of turbulent dissipation rate
μ_{eff}	Effective eddy viscosity

$\Gamma_{..}$	Blending function
$D_{T,ij}$	Turbulent diffusion
$D_{M,ij}$	Molecular diffusion
P_{ij}	Reynolds stress production
Φ_{ij}	Pressure strain
$\varepsilon_{i,j}$	Reynolds stress dissipation
ε	Scalar dissipation rate
a	Speed of sound
γ	Ratio of specific heats C_p/C_v
C_p	Specific heat at constant pressure
C_v	Specific heat at constant volume
R_{ij}	Correlation tensor
τ	Point to Point time difference
r	Point to Point space difference
$x^{(1)}$	Spatial coordinate for 2 nd point
$t^{(1)}$	Temporal coordinate for 2 nd point
$N_{..}\{x, t\}$	Transport equations for velocity fluctuation at different time and position
L_{vK}	Von Karman length scale
κ	Von Karman constant
Q_{SAS}	Additional source term in SSTKWSAS model
Δ	Size of local cells
Y_{fuel}	Instantaneous mass fraction of fuel
Y_{ox}	Instantaneous mass fraction of oxidizer
Y_k	Species mass fraction for species k
ω_{fuel}	Reaction rate of fuel

$\dot{\omega}_{ox}$	Reaction rate of oxidizer
$\dot{\omega}_T$	Reaction rate for temperature
$\dot{\omega}_k$	Reaction rate for species k
$\overline{\dot{\omega}_c}$	Mean reaction rate of progress variable
T	Temperature
Q	Heat released by the complete combustion of 1kg fuel.
λ	Thermal conductivity
D	Diffusion coefficient
Le	Lewis number
Y_{fuel}^0	Fuel mass fraction at fuel inlet
Y_{ox}^0	Oxidizer mass fraction at oxidizer inlet
T_{fuel}^0	Temperature at fuel inlet
T_{ox}^0	Temperature at oxidizer inlet
Z	Mixture fraction
\mathbf{Z}	Normalized elemental mixture fraction
Z_i	Elemental mixture fraction
$Z_{i,fuel}$	Mixture fraction at fuel inlet
$Z_{i,ox}$	Mixture fraction at oxidizer inlet
$\overline{\mathbf{Z}'^2}$	mean mixture fraction variance
s	Stoichiometric ratio
S	Swirl number
$d1$	Inner diameter of swirler
$d2$	Outer diameter of swirler
$\bar{\rho}$	Density weighted method averaged ‘density’
\tilde{u}_i	Density weighted method averaged ‘velocity’
\tilde{Y}_k	Density weighted method averaged ‘species mass fraction for k’

$\overline{u_i''Z''}$	Density weighted method averaged ‘Turbulent scalar flux’ for Z
$\overline{u_i''Y_k''}$	Density weighted method averaged ‘Turbulent scalar flux’ for Y
a_s	Strain rate
X	Scalar dissipation
X_{st}	Stoichiometric scalar dissipation
$p(f)$	Probability density function
SR	Strain rate
Γ	Gamma function
Re_t	Turbulence Reynolds number
u'	Velocity fluctuation
Da	Damköhler number
Da^{fl}	Flame Damköhler number
Da^{LFA}	Damköhler number of laminar flamelet assumption
Da^{ext}	Damköhler number of laminar flame extinction
τ_t	Turbulent time scale
τ_c	Chemical time scale
l_t	Turbulence length scale
C	Progress variable/Reaction progress
Sc_t	Turbulent Schmidt number
$Y_{i,eq}$	Equilibrium mass fraction for product species
Ka	Karlovitz number
η	Kolmogorov size/turning efficiency
l_F	Flame diffusion layer thickness
l_η	Flame reactive layer thickness
v'_η	Turn-over velocity of eddies

S_L	Laminar flame speed
U_t	Turbulent flame speed
U_l	Laminar flame speed
Σ	Flame area density
S_Σ	Source term in transport equation of flame area density
G	Stretch factor
ω	Tangential velocity
C_d	Constants/Discharge coefficient
b	Blockage factor
m_a	Air mass flow rate
m_g	Fuel mass flow rate
P	Pressure

Chapter 1

Introduction

1.1 Motivation

Since the 1830s when Charles Babbage designed the 1st modern computer, these have gradually become an indispensable tool for people's life. Computational power underwent particularly rapid development in the 1940s, attributed to the development of electronic digital computing devices. In almost the same period, modern computation fluid dynamics (CFD) comes into our vision as Lewis Fry Richardson started to use the finite difference method and meshing methods in his numerical calculations. Since the 1990s, accompanied by further developments of modern computers, computer aided CFD methods have become an important tool in resolving problems associated with aerospace, automotive and power generation industries.

However, the CFD technique has major difficulties in providing numerical solutions to complicated engineering problems not only because of the complex geometries used in industry but also because of our desire to use models which better capture the underlying physics and to improve numerical accuracy. One of the very difficult industrial problems nowadays is the design of aircraft engines which is well-known as the crown jewel of the aerospace industry. Three main components have formed a simple working system for the modern gas turbines used for aircraft engines, the compressor, the combustor and the turbine. The ignition of fuel-air mixtures in the gas turbine combustor provides thrust to the entire aircraft as well as supplies energy for

the work done in the turbine and compressor. Six elementary components are always integrated into the combustor, the fuel injector, swirler, primary holes, dilution/secondary holes, an exit nozzle, and a porous wall for cooling purpose.

Although the development of CFD techniques has greatly reduced the efforts engineers need to design new generations of engines, improvements are still required to develop better models of the underlying physics, especially the description of turbulent combustion involved in operating gas turbine combustors. The six elementary components each represent complicated challenges and thus exert great difficulties for numerical modelling of industrial representative gas turbine combustors. To avoid these difficulties, many researchers have only considered turbulent combustion in simplified combustor-like burners without all of essential components presented. Although much progress has been done in understanding, there is still limited research which has considered how to simulate industrially representative gas turbine combustors accurately and efficiently. Past efforts to simulate turbulent combustion in realistic gas turbine combustors have always lacked appropriate accuracy and the computational time requirement of physical modelling has usually been unacceptably large.

Therefore, this thesis focuses on an issue which is of great interest to industrial engineers as well as academic researchers, i.e. the simulation of the turbulent combustion within a realistic gas turbine combustor accurately and efficiently by (i) employing a partially premixed combustion model and (ii) adopting a new generation of scale resolving simulation (SRS) turbulence models called SSTKWSAS. Further details of these will be given below. The models used

represent an effort to include details of turbulent combustion physics which are rarely taken into account or more often simply abandoned in previous simulations of realistic combustors.

1.2 The Gas Turbine in Power Generation Industry and Aviation

The advent of Gas-Turbines for military purposes tracks back to 1940s, and it was subsequently used for aviation and later for ground level power [1]. Sir Frank Whittle, a British Air Force (RAF) engineer, known as the inventor of the first workable British aero-propulsion gas turbine and Germany's Dr. Hans Von Ohain are credited independently with the first jet powered aircraft.

Following on from their excellent works in the 1940s, people witnessed a rapid development of gas turbines from the early aviation use of the Whittle W1 and W2 engines (Figure 1.1) to the modern industrially used high power combined cycle gas turbines such as the 1600°C J-series engine developed by Mitsubishi Heavy Industries, Ltd (Figure 1.2). An example of the largest four-engine jet used in civil aviation is the Airbus A380 manufactured by European Union manufacturer Airbus and first tested in 2005 equipped with a Rolls-Royce Trent 900 engines (Figure 1.3), which are able to provide a thrust of up to 360KN for each engine.

Three main components are used to form a simple working gas turbine, the compressor, the combustor, and the turbine. The compressors are responsible for compressing the air drawn in from the atmosphere and delivering this into the combustor where combustion is initiated by igniting a mixture of injected fuel and air. The high pressure, high temperature burnt gas provides energy to

rotate the turbine which in turn drives the compressor through a shared central shaft. The remaining thermal energy generated from burning the fuel-air mixtures is turned into mechanical energy in a propulsion nozzle to provide reverse thrust. Because the compressor and turbine are linked together through the central shaft, this combined system is typically referred to as turbo machinery.

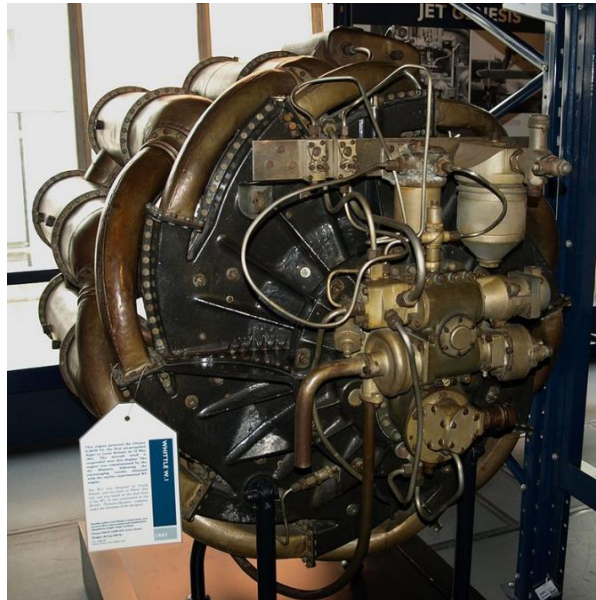


Figure 1.1: Power Jets W.1, Type: Turbojet [2].



Figure 1.2: J-series gas turbine developed by Mitsubishi Heavy Industries, Ltd [3].



Figure 1.3: Rolls-Royce Trent 900 engines, Type: Turbofan [4].

Based on different requirements and working conditions, several types of gas turbine engines for aviation have been designed: the turbojet, turboprop, turbofan, and after-burning turbojet.

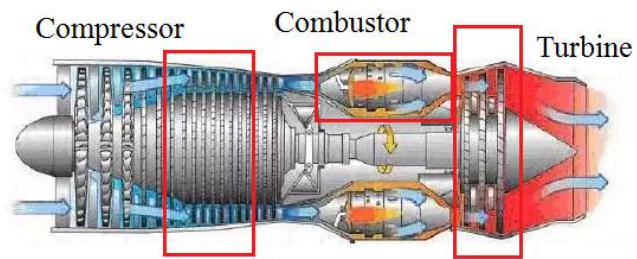


Figure 1.4: Modern Gas Turbine, Type: Turbojet [5].

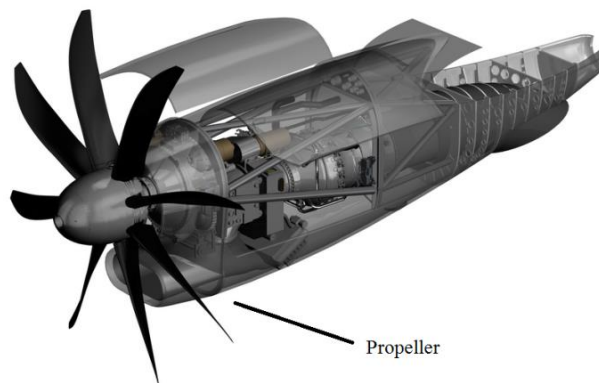


Figure 1.5: Modern Gas Turbine, Type: Turboprop [6].

The simplest gas turbine engine (Figure 1.4) is the turbojet which uses the basic three components to provide thrust at moderate airspeed. On the other hand, turboprop (Figure 1.5) design contains a propeller which sits in front of the whole engine to provide stronger thrust at a lower speed. A turbofan design (Figure 1.6), combines the benefits of turbojet and turboprop, and is the most modern version of aircraft turbine engines. The bypass ratio between the mass flow rate of air drawn through the fan to the mass flow rate of air through the engine core partially decides the range of applications of the engine. Engines with low bypass ratio (low frontal area) are applied mainly to military combat aircraft where high speed and hence low frontal area is required, while those with high bypass ratio are used in commercial passenger aircraft or transport aircraft due to the greater thrust generated and greater payload capability. The afterburning turbojet (Figure 1.7), strictly speaking, is not a unique type of aircraft engine. It is designed to increase the combat ability of military aircraft by adding extra fuel into the exhaust stream to produce additional thrust.

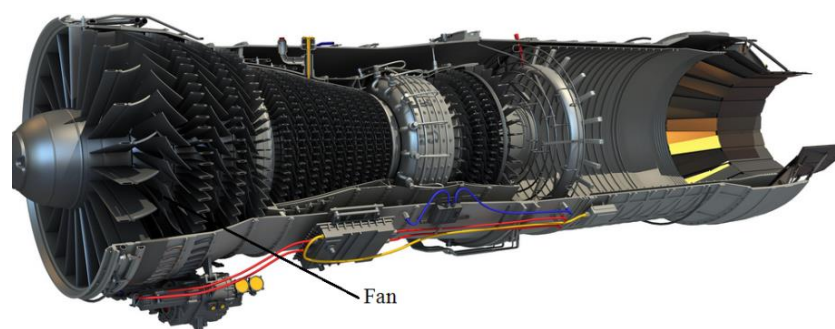


Figure 1.6: Modern Gas Turbine, Type: Turbofan [7].

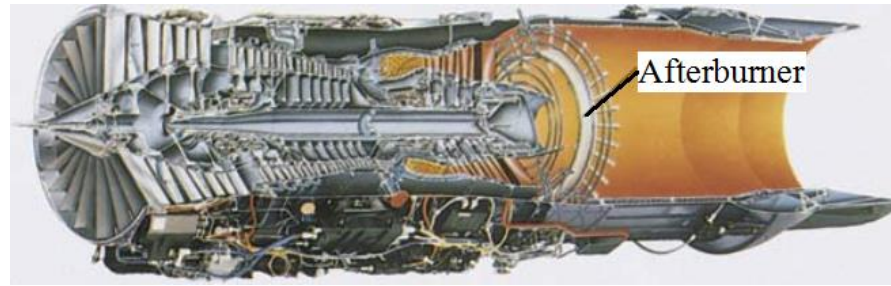


Figure 1.7: Modern Gas Turbine, Type: Afterburner Turbojet [8].

One of the most difficult components to design in any type of gas turbine is the combustion chamber in which the high pressure and temperature working condition require extra attention. Many kinds of combustor chambers have been designed over recent decades to achieve the following main purposes:

- To improve the burning efficiency of fuel and oxidizers.
- To control, i.e. lower the pollutant emissions such as carbon monoxide (CO), nitrogen oxide, sulphur dioxide (SO₂) etc.
- To improve the stability of combustion and the expected life of aircraft engines.
- To minimize the size of the combustion chamber and reduce the weight of the whole engine.

To achieve the above goals, an understanding of the complex flow physics within the gas turbine combustor is required. There are three major geometries used for combustor chambers: the can type, the can-annular type and the annular type. In early years, the can-type combustor was proposed first due to its ease of design, maintenance, and testing. However, it is heavier and of efficiency lower compared to the other types. This is because the can type combustor (as shown in Figure 1.1) are self-contained type of combustor.

Each ‘can’ has its own liner, fuel injector, and casing. The can-annular type combustor has abandoned casing for each individual liner and an annular ring is used as casing (Figure 1.8). The annular type combustor, with its smaller size, higher efficiency, and better-controlled exit temperature is widely used for modern gas turbines. Not only casings are replaced by annular rings, simple and continuous liners are used to replace the old design (Figure 1.9).

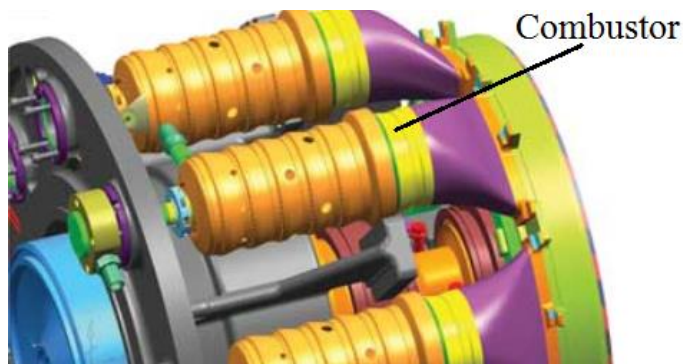


Figure 1.8: Can-annular type gas turbine combustor [9].

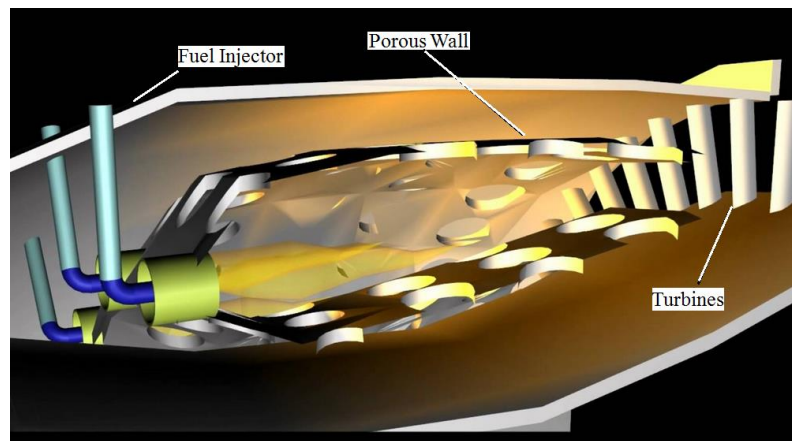


Figure 1.9: Annular type gas turbine combustor [10].

Regardless of different designs of combustors, six elementary components are always integrated into the combustor, the fuel injector, swirler, primary holes, dilution/secondary holes, exit nozzle, and porous wall for cooling purpose. Each individual component introduces significant complexity into the flow characteristic of the combustor. The swirler and primary holes, which are

responsible for the creation of a strong recirculation region in the head of combustor (primary zone), influence the local air-fuel ratio, temperature, emission and flame stability during combustion. The porous wall, designed to allow cooler air to pass through, prevents the combustor walls from overheating and being damaged. The secondary zone, in between the primary zone and the dilution holes, is responsible for oxidizing CO to CO₂ and completing the combustion process. The exit temperature profile is mainly controlled by the dilution holes to prevent damage to the downstream turbine blades.

1.3 CFD in Gas Turbine Combustor

To understand the interactions of each individual component and to design combustors more efficiently, CFD techniques are widely used in both academia and industry. More complex turbulent combustion models, though widely proposed, require more validation against experimental data, which is one of the main focuses of the present thesis.

As has been mentioned already, modern computational fluid dynamics (CFD) is first observed when Lewis Fry Richardson started to use the finite difference method on simple Cartesian meshes. Modern meshing method allows much more complicated geometry flow problems to be considered (Figure 1.10).

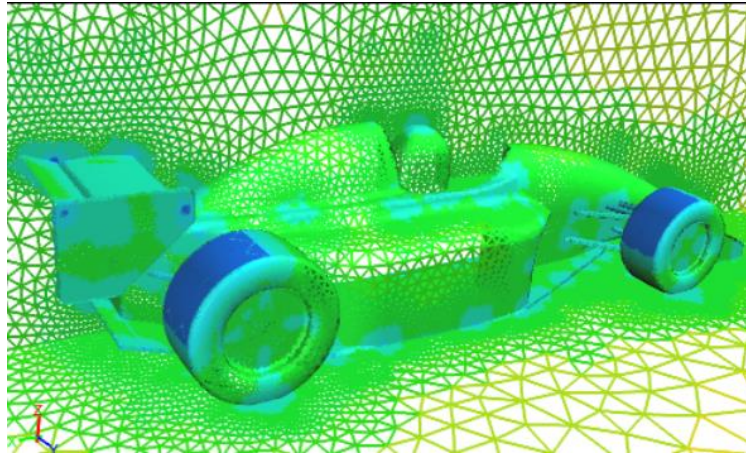


Figure 1.10: A modern meshing method applied on Racing Car [11].

The basic idea of CFD is to provide numerical solutions to the conservation equations which are derived from conservation laws for mass, momentum, energy and other flow properties. The numerical solutions of these partial differential equations (PDE) achieved at points surrounded by small control volumes can be used to describe the fluid flow. Although the basic idea is simple, the accuracy of the achieved numerical solutions can be challenging. Various techniques have been proposed and developed to reduce errors such as physical modelling errors, numerical discretization errors and iteration convergence errors. Amongst all these possible errors, physical modelling errors are crucial in capturing real world physics as these require empirical input to calibrate model constants.

In the case of laminar flows, the Navier-Stokes equations are accepted to be accurate in describing the continuous flow. However, in turbulent, reacting or multi-phase flows extra models and their empirical constants are necessary. In the case of turbulence, the quasi-random motion of quantities relative to their time-averaged value increases the complexity substantially. The deviation of these motions from the mean forms the so-called turbulent spectrum through

which the turbulence kinetic energy is transmitted. Across the turbulence/energy spectrum, eddies of the largest length scale receive energy from the mean flow and are eventually dissipated by viscosity at the smallest (Kolmogorov) length scale. The ratio of largest to smallest length scale in a typical flow is proportional to $Re^{3/4}$ [159] and since the typical Reynolds numbers of industrial flows are greater than a few thousands, a huge spectrum results and thus solving the whole spectrum of turbulence is not feasible/affordable currently.

Two methods are available to be used to reduce the effort required to solve turbulent flow problems. The ensemble averaged Navier-Stokes equations maybe closed completely using empirical models (Reynolds Averaged Navier-Stokes or RANS approach). Alternatively, a filtering method is used to remove and model the smaller scales and the part of the turbulent spectrum containing the large scales is solved numerically. The implementation of these models always involves complex LES turbulence closures or complex unsteady numerical schemes which can significantly increase the computational time. The trade-off between computational time and accuracy is obviously of great concern to both researchers and engineers.

As to CFD of the gas turbine combustor, the accuracy of its numerical simulation is highly challenging as it is dependent on the two very difficult problems of modelling both turbulence and combustion (which are interrelated and control fuel/air mixing and chemical reaction). Typical values of Reynolds number in gas turbine combustors can range from several hundred thousand to several million and multiple chemical reactions are involved in the combustion

of hydrocarbon fuels which is currently only poorly understood. Even if the species reaction rate in the Reynolds-Averaged transport equation for species can be approximately described by an exponential Arrhenius equation, the time-mean of the equation does not equal to the multiplication of the time-mean values of each individual species due to its non-linearity. Therefore, turbulent combustion models are also required to provide closure to all mean species equations in addition to the need for a turbulence model. Thus, possible combustion modelling error poses extra difficulties for the simulation of gas turbine combustors.

To improve the reliability of the simulations, a turbulence modelling approach which is able to resolve numerically the majority of turbulence scales in the turbulence spectrum together with a combustion model which can incorporate at least some of the chemical reactions must be properly chosen to allow a more realistic prediction of turbulent combustion.

1.4 Current Contribution

The work presented in this thesis makes the following specific contributions to the field of CFD simulation of realistic industrial used gas turbine combustor:

- The performance of two partially premixed combustion models using a flamelet/progress variable approach (the FPVA method) is, for the first time, applied to a complex combustor flow.
- The reasons for the weak performance of the traditionally used non-premixed combustion models are discussed fully with respect to their application in combustors.

- The reasons for the better performance of partially premixed combustion model, the Zimont Turbulent Flame Speed Closure method (ZTFSC) are discussed.
- A comparative study of two partially premixed combustion models ZTFSC and ECFM (the Extended Coherent Flamelet Method) is performed for the first time. It is demonstrated that the former model outperforms the latter by predicting closer temperature agreement with experimental results.
- A possible explanation is proposed regarding why the ZTFSC model outperformed the ECFM model since the two models both employ the FPVA method.
- A more effective and efficient method (comparing to those used in previous work) for simulating complex gas turbine combustors is proposed by employing a 2nd moment Reynolds stress closure turbulence model (RSM) in conjunction with the ZTFSC combustion model.
- As a lower-order alternative to the RSM turbulence model, the so-called second generation scale adaptive simulation (SRS) approach of Menter et al [126] is for the first time successfully applied to the simulation of complex gas turbine combustor in conjunction with the ZTFSC combustion model. The superior performance of this approach with respect to efficiency and ability to resolve the turbulence spectrum are documented.

- The conclusions are then drawn that, by employing the SRS plus ZTFSC combustion model approach, turbulence combustion in complex gas turbine combustors can be captured with much higher accuracy, although lower computational efficiency compared to application of RSM and ZTFSC.
- Finally, it is suggested that an accurate flame shape/temperature in the primary region of the combustor can only be achieved by taking into account the partially premixed regimes using the FPVA method regardless of the turbulence model chosen. Particular turbulence models can only improve the prediction locally but not in an overall sense.

1.5 Thesis Outline

In **Chapter 2**, a literature review of numerical simulations in combustor-like burners and complex industrial used gas turbine combustor geometries is presented. The underlying assumptions in the various combustion models originally designed to simulate simple jet flames, swirling flames, lifted flames etc. in simple combustor-like burners are introduced first, followed by a discussion of the defects of these models when used to simulate complex gas turbine combustors. Then a short literature review on the development and application of the new approach to scale resolving turbulence models is presented in order to show the capability of this in at least partially resolving the turbulence spectrum without an explicit dependence on local cell size. Questions and gaps which need to be answered and filled that have emerged

from previous experimental and numerical researches are highlighted at the end of this chapter from the viewpoint of both turbulence and combustion.

In **Chapter 3**, the governing equations, mathematical formulations, and closure approaches of the models for solving the turbulence combustion problem in the current thesis are derived and presented. As the main focus of this thesis is the investigation of the performance of different combustion models, a classification of existing combustion models in terms of their underlying assumptions is comprehensively discussed.

In **Chapter 4**, the numerical methods used in the current study are presented and the reasons for choosing these methods explained. The experimental configuration used for this thesis is also introduced briefly, with details concerning the original experimental study and other relevant research work. The reaction mechanism and its look-up table are presented in the final section of this chapter to demonstrate the impact of scalar dissipation.

In **Chapter 5**, combustion simulations of a complex gas turbine combustor are presented in four sections starting with a short introduction and followed by illustration of flow field and scalar variable behaviour inside the combustor. Subsequently, a statistical comparison between current predictions, experimental results, and previous predictions from the literature is provided. Finally, conclusions and discussions are given in the last section.

In **Chapter 6**, a comparative study of the behaviour of several turbulence models in predicting gas turbine combustor flow whilst invoking the same combustion models as in the last chapter is conducted. This chapter is also split into four sections.

Finally, in **Chapter 7**, to provide closure to the entire thesis, a brief summary of the main conclusions drawn from this work is presented together with future work recommendations.

Chapter 2

Literature Review

2.1 Introduction

In this chapter, the main focus is to examine past contributions of other researchers' work on CFD simulation of gas turbine combustors as well as findings in simulating simple burner flames. In addition, some significant experimental research work is also presented since these have laid the most solid and steady foundation for judging the success of CFD simulation.

Chapter 2 is presented in four subsections as follow:

First, the findings from past research work, which has focused on revealing the turbulent combustion physics in a combustor-like burner, is presented, and followed by a discussion of their contribution in establishing combustion modeling methods from simple jet flames to flames with strong local extinctions and re-ignition. Then, the major findings and main issues encountered in these research works are highlighted and addressed to provide a concise description.

Second, both CFD and experimental work carried out by other researchers focusing on some complex gas turbine combustor geometries are presented. The merits and drawbacks of the combustion models that were discussed in the first section are discussed further with respect to complex gas turbine combustors.

Third, a short literature review of the developments and applications of the second generation scale resolving approach (discussed in detail below) is presented and discussed.

Finally, brief critical reviews of the above research findings in both simple combustor-like burners and complex combustors are provided to highlight the deficiencies, gaps, and questions which remain to be answered.

2.2 Combustion Research Work in Simple Combustor-like Burners

2.2.1 Experimental and numerical work

Since the 1970s, researchers have realized that the main scalar quantities such as CO_2 and H_2O , temperature, and the flow field for simple turbulent reacting flows [12, 13] can be accurately predicted by flame sheet models [14] using the frozen or shifting equilibrium method, while the concentration levels of slow forming radicals such as NO_x are not well captured by this approach. The modeling of finite-rate chemistry thus became an important research topic in both academia and industry, particularly in turbulent non-premixed flames where moderate Damköhler numbers (ratio of mixing time to chemical reaction time) result in an increase in complexity due to the strong interaction between mixing and chemical scales. To understand the underlying physics of turbulent combustion, ongoing collaborations between several universities and industries have moved from simple jet flames of hydrogen or hydrocarbon fuels to more complicated swirling flames, lifted flames, piloted flames or bluff-body flames, which involve enclosed complex turbulence-chemistry interactions such as recirculation, local extinction or blow-off have.

Various modelling techniques for turbulent reactive flow have been proposed, the most widely used currently are the Flamelet Method that the turbulent flame is viewed as a mixture of laminar flamelet structures (see Figure 2.1) [15-17] and the Conditional Moment Closure (CMC) method [18, 19]. The former assumes all instantaneous quantities are a known function of the aerodynamic strain rate and the mixture fraction, where the latter assumes that scalar quantities are strongly correlated with particular value of the mixture fraction which needs to be updated by providing a set of transport equations for conditional moments. The CMC approach is thus far more expensive than the Flamelet Method.

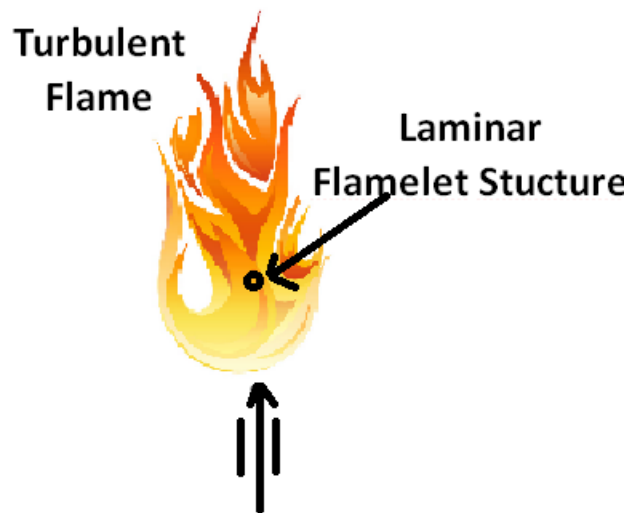


Figure 2.1: Laminar flamelet in a typical turbulent flame.

Both methods rely on knowledge of the statistical distribution of the mixture fraction, usually represented via the probability density function (PDF) [20, 21] to impose turbulence effects and evaluate the averaged scalar quantities produced during the combusting process. Figure 2.2 shows the turbulence and stretch effect on laminar flamelet that when flame is stretched with a higher value of strain rate (a in the figure), maximum temperature at stoichiometric

mixture fraction is reduced; While when turbulence effect (under effect of PDF) is applied, the mixture fraction may vary accordingly and hence showing different temperature. Two possible PDF approaches are available to express the turbulence effects, either by directly assuming the shape of the PDFs which are used as weighting functions to tune the mean values of species mass fractions, density and temperature, or alternatively by solving a transport equation for the joint PDF (TJPDF) of scalar and velocity fields which then closes the highly nonlinear reaction term completely without modelling. The latter method can also be treated as an independent combustion model including sub-mixing-models such as Interaction by IEM (Exchange with the Mean) [22], or Linear Mean-Square Estimation (LMSE) [23], MC (Modified Curl) model [24] or EMST (Euclidean Minimum Spanning Tree) mixing model [25]. These have been widely tested in both simple and complicated reacting flows [26-29], however, the TJPDF method was proposed as partially more applicable for calculating slow chemistry [30, 31] at the low Damköhler numbers. The $N+2$ dimensions (temperature, pressure, and N species) of the PDF transported approach made this method computationally much more expensive than both Flamelet and CMC methods.

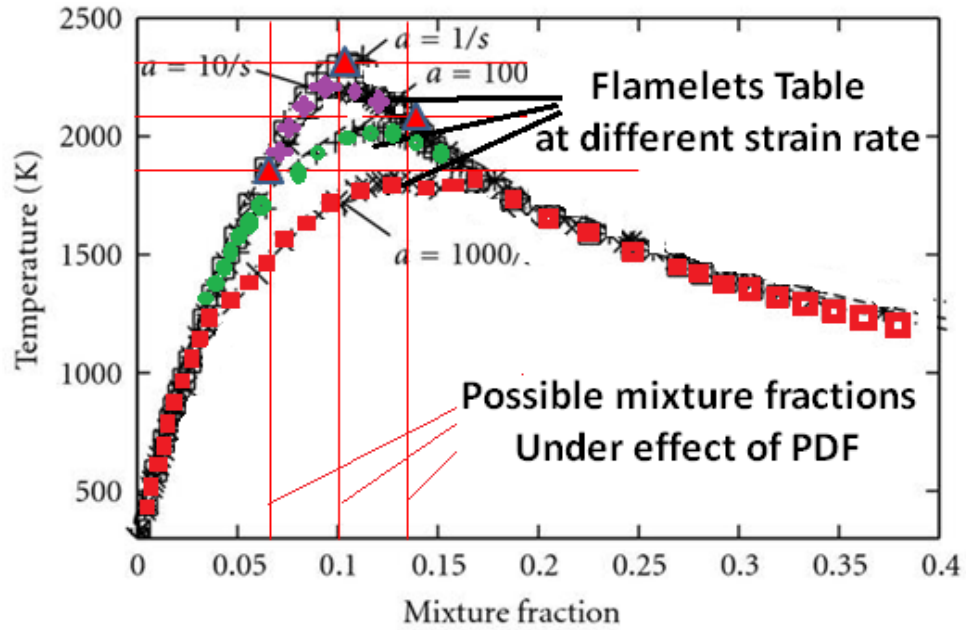


Figure 2.2: Turbulence and stretch effect on laminar flamelet. Red vertical lines represent the effect of turbulence/PDF, various peaks of parabolic curves represents the effect of stretch/strain rate.

Thus, in the early 1970s, many researchers preferred to use the strained laminar flamelet method to predict practical turbulent non-premixed flames in which significant departure from chemical equilibrium from slow radical formation and flame lifting was expected [16, 32, 33]. Although satisfactory results were achieved, minor and slow forming radicals such as OH and NO_x were still not accurately predicted [34, 35].

In 1988, Haworth et al [36] compared the performance of the TJPDF method with a steady laminar flamelet method (SLFM) in predicting a CO/H₂/N₂-air turbulent jet flame. The agreement between SLFM and experiment was comparable to that observed using the TJPDF approach, and SLFM showed some advantages near the nozzle of the flame (fuel rich), but was less satisfactory for the region downstream of the flame (chemical equilibrium). This was speculated to be caused by over-prediction of the laminar flame

thickness compared to the estimated Kolmogorov length scale (smallest turbulent eddies). When the smallest turbulent eddies penetrate the reactive layer of the laminar flame thickness as shown in Figure 2.3, the inner flamelet layer is broken up, and SLFM approach is no long valid.

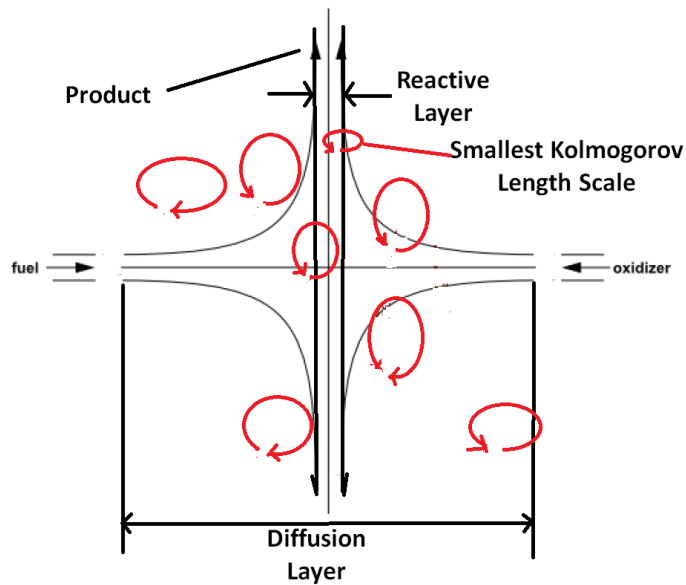


Figure 2.3: A sample laminar flamelet under the effect of turbulence.

In 1988, the same jet flame [37] was predicted by an SLFM method modified on an ad hoc basis to account for the inaccurate assumption made that the flamelet lifetime was assumed to be much longer than the time scale of changes in the scalar dissipation rate [38]. This analysis suggested that downstream of flame, the laminar flamelets cannot reach quasi-equilibrium as rapid as was thought to be and this implied that the non-zero response time of the flamelet structure to the rapidly decaying strain rate must be taken into account. A similar issue was noticed by Barlow and Carter [39] in their measurement of the concentration of major species such as CO_2 and H_2O , minor species such as OH and NO , mixture fraction, and temperature in a turbulent non-premixed helium-diluted hydrogen jet flame. It was shown that

the turbulent flame structure, which is very thin near the burner nozzle became wider at the front of the flame.

In 1998, Pitsch et al [40] used SLFM and a transient/modified SLFM method to predict an H₂/N₂ jet diffusion flame with local extinction and re-ignition. Although the major species concentrations and even OH concentration were accurately captured, both methods failed in predicting NO concentrations, although the modified SLFM provided relatively better NO level prediction. It was concluded that the necessity to include transient effects was due to the fact that the diffusion time of a flamelet became much greater than the flamelet lifetime from fuel rich region approaching to outer quasi-equilibrium flame tip as the scalar dissipation rate decreased with x^{-4} where x was the distance from the burner base. The inclusion of transient effects led to the well-known Unsteady Laminar Flamelet Model (USLFM) [41-43].

Although USFLM performed better than SLFM in predicting slow forming species, local extinction and re-ignition of the flame (which can occur often in practical burners) increased the prediction difficulties. Such phenomena have been observed experimentally by Barlow and Frank [44] in a C₂H₂/H₂/air/CO₂/N₂ piloted flame (Figure 2.4). Local extinction due to high speed cold main jet flow (25%CH₄ and 75%air) near the burner base was overcome by addition of a piloted flame, which prevented lift-off and blowout.

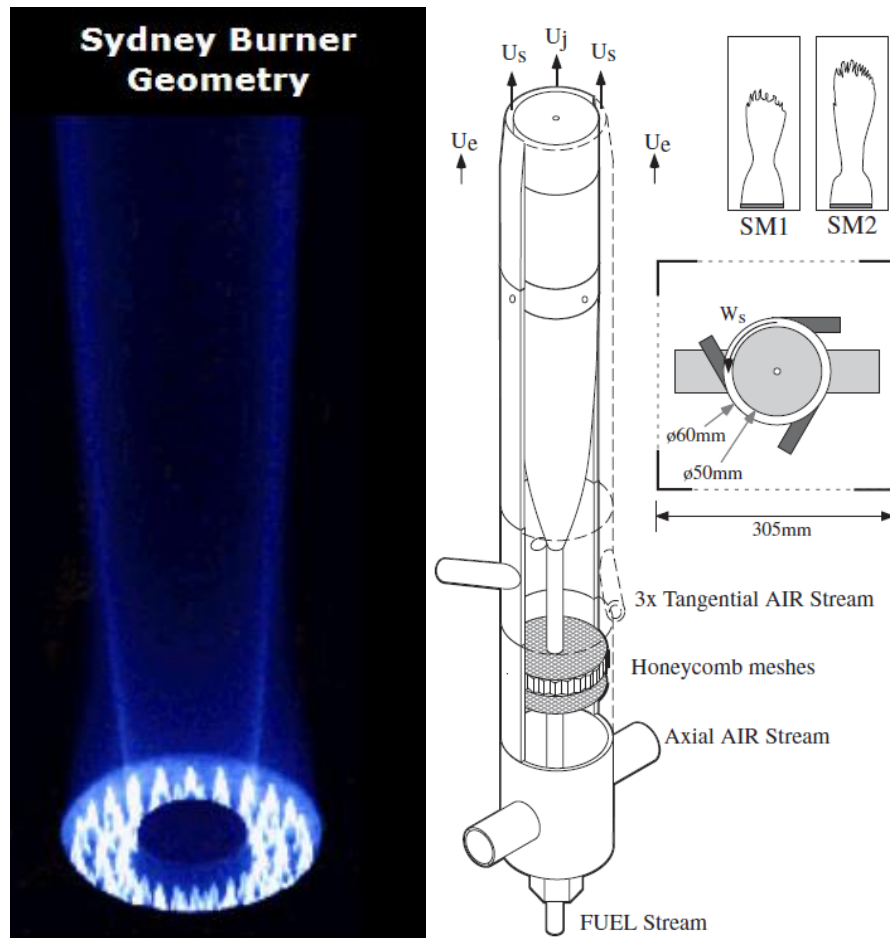


Figure 2.4: Left: Piloted flame [44]. Right: Sketch of a test facility for the swirling flame of SM1 and SM2 [45].

On the other hand, other researchers have shown that local extinction can be captured by the USLFM method but re-ignition cannot [46-49]. The major difficulty of flamelet methods in predicting re-ignition was related to the lack of interaction between the unburnt mixture (local cold spots) and the burnt mixture (incoming hot spots) [50]. Although other researchers (e.g. Xu and Pope [51], Tang et al [52]) have shown the potential of the TJPDF method in predicting flame local extinction and re-ignition conditions, as noted above, its high computational cost and limitation to slow chemistry has meant it is rarely used. Other numerical investigations [53-55] have also validated the performance of various turbulence and more combustion models against

experimental data [56-60] of flames with strong local extinction and re-ignition.

Having tested various turbulent combustion models in simple jet flames, researchers then started to focus on more complicated reacting flows such as lifted and swirling flames. In 2002, Kalt et al [45] introduced a new burner in which stabilised, highly swirling turbulent non-premixed methane flames were produced (Figure 2.4). Local extinction and the presence of local non-burning gas samples were seen to occur frequently in flames far from global blow-off, especially with a higher fuel jet velocity flame. The reason for this was identified as a distinguished feature of highly swirling flames. Figure 2.5 shows a virtual swirling flame which can be generated by a swirler fitted in the burner, the flame surfaces are highly corrugated as in a typical swirling flame.

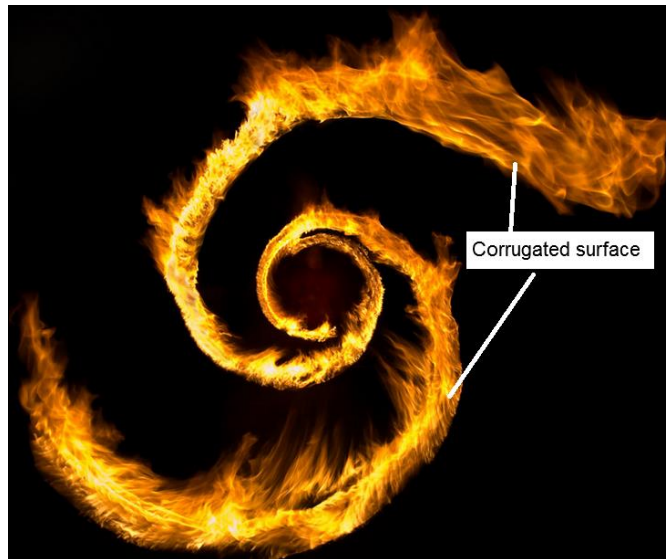


Figure 2.5: A typical swirling flame [62].

Al-Abdeli and Masri [63] in 2003 investigated the stability characteristics of a swirling flame in a similar burner to Kalt et al [45] using different fuels (CNG, CNG-air, CNG-H₂) and swirl numbers. It was noted that at high swirl number, the flame easily lifted off the burner's base while at low swirl number, the

flame remained stable at the base but blew off in the downstream neck region of the burner. Improvements in blow-off limits occurred when the swirl number reaches a certain threshold of about 0.6. Similar conclusions were also made by Masri et al in 2004 [64] when spontaneous Raman-Rayleigh-LIF technique was used to measure the concentration of reactive species in a highly swirling, turbulent non-premixed flame. The increase of swirl number was confirmed to widen the range of blow-off and more locally unburnt fluid samples appeared within the recirculation zone. These findings from the above researchers may imply increased difficulty to predict highly swirling flow using both SLFM and USLFM methods due to their weaker ability in describing local extinction and re-ignition phenomenon.

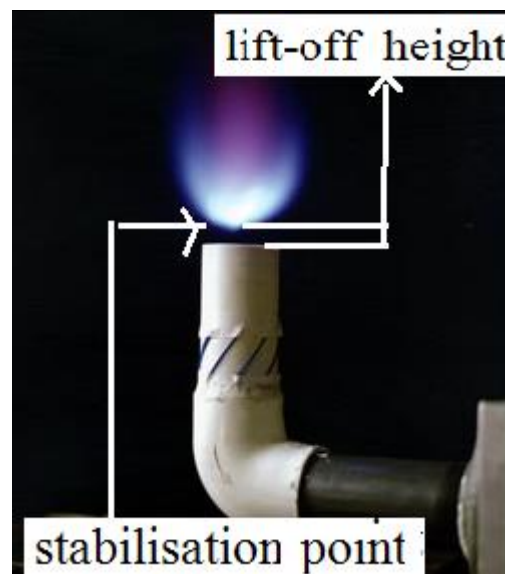


Figure 2.6: A typical lifted flame [65].

On the other hand, many experiments have been conducted since the 1960s to understand the basic mechanisms of lift-off height (Figure 2.6) and blow-off limit in turbulent non-premixed flames under different operating conditions [66-68]. Recent research has focused on understanding the local extinction and re-ignition mechanisms and developing models to describe these phenomena

[69-71]. The flame lift-off and stability mechanisms were divided into two categories: the premixed burning velocity dominated category, and the non-premixed jets quenching limit dominated category. The former assumed that a lifted flame is stabilised at a position where the local flow velocity is equal to the premixed burning velocity [72]. The latter assumed that the competition between physical and chemical time scales dominates the stabilisation of a lifted flame [73, 74]. If chemical time scales are smaller than flow residence time, i.e. large Damköhler number, the flame is stabilised. If there is an increase of strain rate which is inversely proportional to flow residence time, the flame becomes unstable. In other words, the 2nd category relates flame stabilisation and blow-off to flame quenching so that the stable flame sits at a point (Figure 2.6) within the range defined by higher dissipation rate and flame quenching limit.

Many combustion models have been tested in predicting lifted flames [75-79]. Many of these employed the TJPDF [64, 80, 81] and CMC [82-87] methodologies, although the two methods are assumed less popular than flamelet methods due to the computational cost aspect addressed before.

In recent years, to solve the problems experienced with SLFM and USLFM, the principles involved in both the stability mechanisms mentioned above were combined and embedded into the flamelet method in order to predict local extinction and re-ignition in lifted flames. The re-ignition phenomenon in a lifted flame is not as obviously included as local extinction since, if the first stability mechanism is correct, hot combustion products must be responsible for re-ignition of the cold mixture. In addition, if the second

mechanism is also correct, the behaviour between chemical reaction time and flow residence time must also be taken into account when dealing with re-ignition.

Thus, Pierce and Moin [88-90] recently proposed a partially premixed combustion model based on the combined mechanisms described above to predict local extinction and re-ignition. Their model was based on a flamelet/progress variable approach (FPVA) so that the scalar properties are now a function of both mixture fraction and progress variable, which describes the extent of reaction in the local mixture. The effect of strain rate as included in the 2nd mechanism was taken into account through implicitly varying the amount of progression made in chemical reactions. In other words, the progress variable varies with scalar dissipation/strain rate. Their methods is similar to that used by Janicka and Kollmann [91] who solved two transport equations for mixture fraction and a reactive scalar, and closed the chemical reaction term using the transported PDF method. A similar idea was also used by Bruel et al [92] using a presumed-shape PDF method.

Since 2000, many researchers have developed variants of the FPVA method to predict local extinction and re-ignition in non-premixed flames [93-99]. The main differences in these methods were the implementation detail of chemical reactions and scalar state relationships, and the chosen PDF method. Although very good agreement between predictions and experiments was achieved, it must be noted that almost all of these predictions were performed in a simple geometry combustor-like burner in order to isolate the various turbulent combustion phenomena from each other and to capture targeted mechanisms

effectively and efficiently to reduce the difficulty of meshing a complex flow configuration. Despite their success, insufficient validation has been provided using these improved FPVA methods for more complex reacting flows, such as those including turbulent multi-jets, and the highly swirling, non-premixed conditions of industrially representative gas turbine combustors.

In such combustors, combined mechanisms influenced by the effects of swirling flow (which result in widened blow-off limit and increased number of unburnt spots) and high fuel jet velocity (which leads to strong interaction of local extinction and re-ignition), require more representative validation against experiments. Besides, the multi-jet inflows in such combustors create a turbulence environment involving many partially predominantly premixed flamelets, which increases the difficulties in choosing a proper combustion model. More details on this are presented below in **Section 2.3**.

2.2.2 Summary of research work on turbulent jet flames

Several important findings and issues involved in predicting turbulent jet flames in combustor-like burners are listed here again for clarity:

- CMC, TJPDF and the flamelets method have been widely employed in predicting simple jet flames. The first two are more accurate in predicting slow chemical reactions, local extinction, and re-ignition while the latter is weaker in predicting lifted and swirling reacting flows due to the lack of interaction between the unburnt mixture (local cold spots) and the burnt mixture (incoming hot spots).
- Although CMC and TJPDF display superior performance to the

flamelet methods, they are far more time consuming than the flamelet methods. In addition, the TJPDF has been identified to be less effective in predicting fast chemical reactions at high Damköhler numbers due to the inaccurate modeling of molecular diffusion (mixing models).

- The steady and unsteady flamelet approach (SLFM and USLFM) are expected to be equally accurate in predicting major species concentration and temperature distributions in simple jet flames (no extinction and re-ignition) while the latter is more accurate in predicting fuel-lean flames and NO_x concentrations since transient effects of the flamelet structure are considered.
- These transient effects are known to be important due to several reasons: firstly, the flamelet lifetime can be much shorter than its diffusion scale corresponding to the rate of change of scalar dissipation rate closer to the tips of flames. Secondly, a turbulent flame structure which is very thin near the nozzle of the burner becomes wider at the forefront of the flame. Third, the scalar dissipation rate decreases with x^{-4} where x is the distance from the burner base (long time needed for scalar dissipation rate to take effect in flamelets).
- To compensate for defects of SLFM and USLFM methods, the FPVA method has been developed by combining the two stability mechanisms established for lifted and blow-off flames. The first assumes that lifted flame is stabilised at a position where the local flow velocity is equal to the premixed burning velocity, and the second assumes that the competition between physical and chemical time scales dominates the stabilisation of lifted flame.

- Although the FPVA method has been shown to be effective in predicting local extinction and re-ignition in simple jet flames, there is a lack of studies regarding its applicability in the complicated flow configurations which occurs in industrially representative gas turbine combustors generalises several combustion mechanisms together.

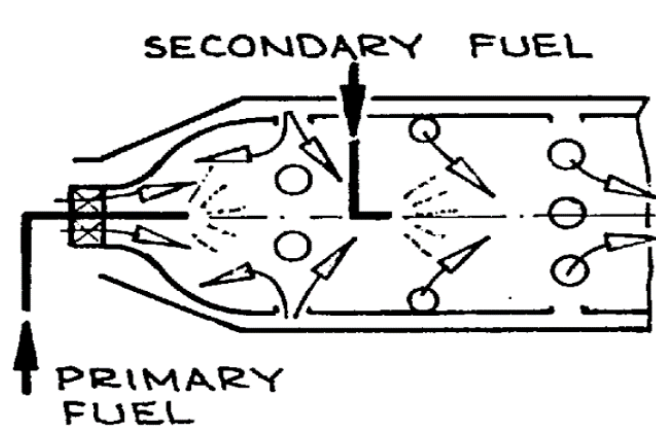
2.3 Combustion Research Works in Realistic Gas Turbine Combustor Geometry

In a realistic gas turbine combustor, several major complexities make the modelling of non-premixed combustion problematic:

- The very strong swirling flow which is used to stabilise the flame and widen the range of blow-off increases the frequency of interactions between the unburnt mixture (local cold spots) and the burnt mixture (incoming hot spots).
- The high fuel jet velocity and strong swirling flow increase the possibility of flame lift-off.
- The penetration of the high momentum primary jets prevents the flame from penetrating to the downstream and increases the flame residence time. Local re-ignition can thus occur more often than in simple lifted and piloted flames.
- The porous wall inflow air although usually assumed not to be involved in any reactions, can contribute to the re-ignition mechanism.
- The interaction between the wall recirculation zone (WRZ) and centre recirculation zone (CRZ) may lead to more aggressive mixing, resulting in more complex combustion mechanisms.

- The multi-jets configuration induces various turbulence length scales which can have a large impact on assumptions made in combustion models, for example, the thin reaction layer flamelet structure assumption requires the Kolmogorov scale of turbulence to be larger than the flamelet reaction layer thickness.
- In realistic gas turbine combustors, because of the multi-jet and a dilution jet, the actual flame is almost inevitably partially premixed although in the past a non-premixed flame has usually been assumed.

Since the 1970s, many experimental works (for example, see Figure 2.7) have been carried out in realistic gas turbine combustor geometries [100-107]. The most popular and complete experimental datasets that have been subsequently used were those published by researchers from Imperial College London [108-117].



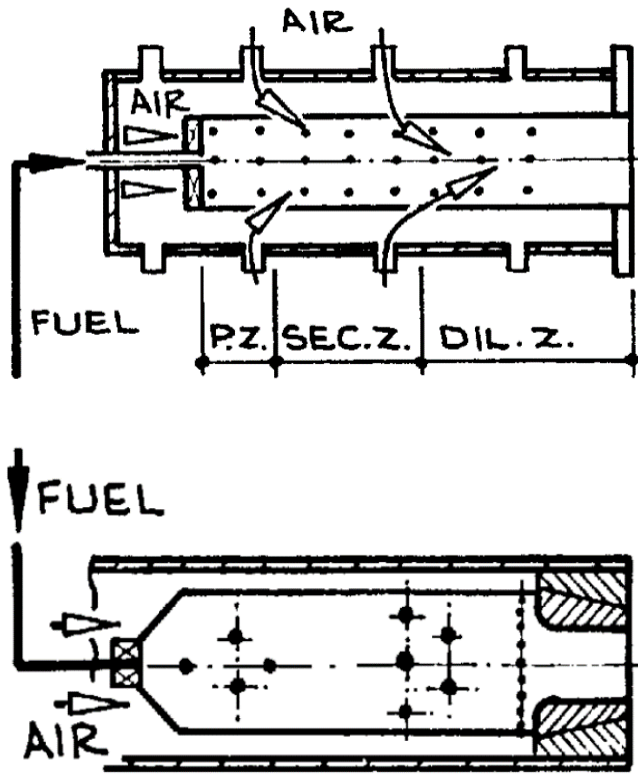
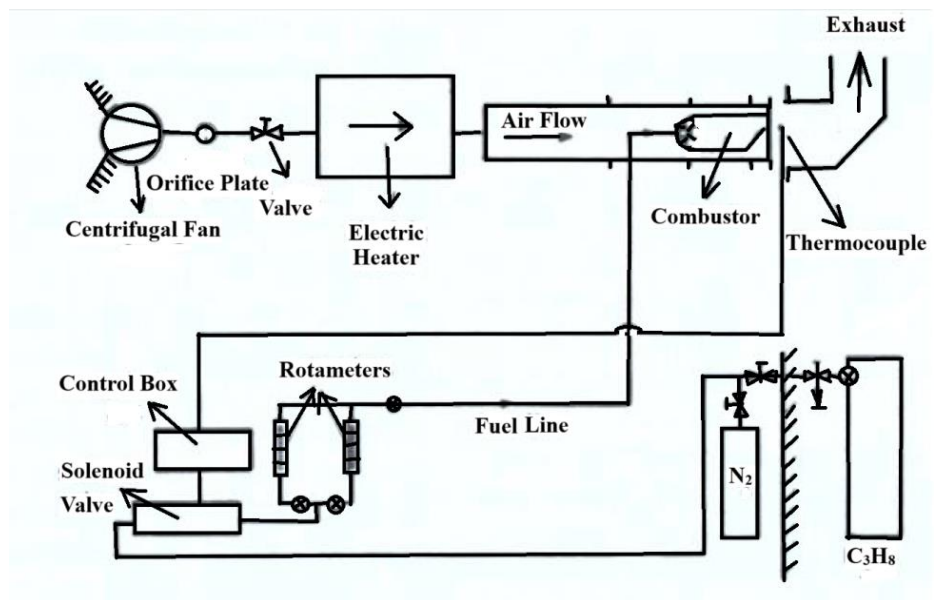
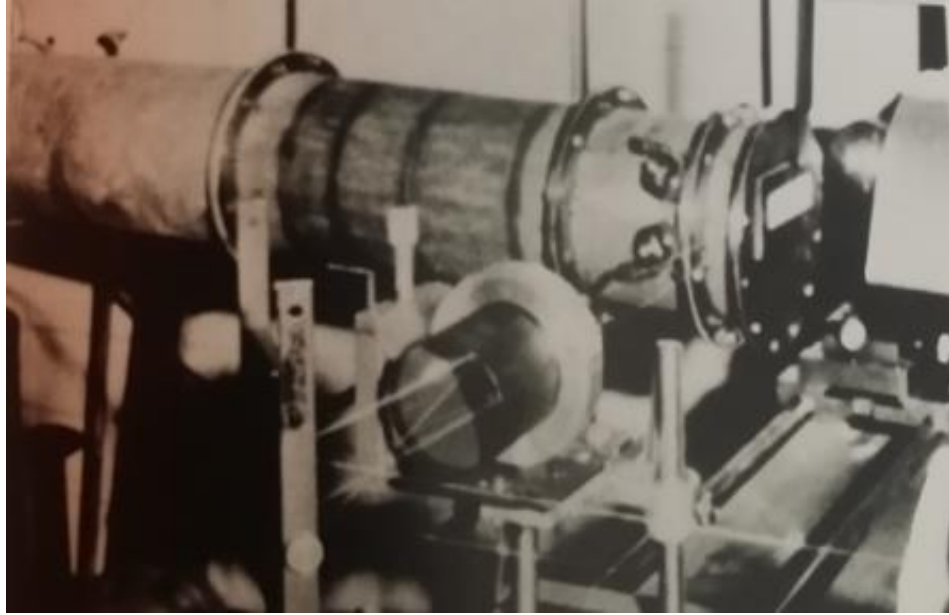


Figure 2.7: Sketch of the several combustors in past experimental works [100-102].



(a)



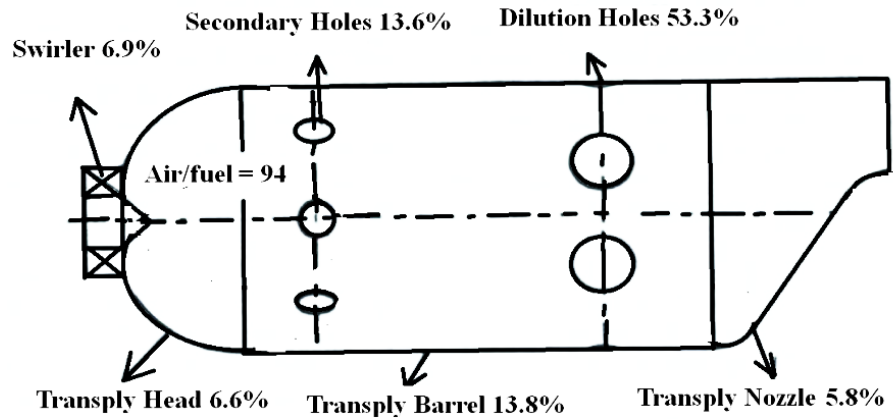
(b)

Figure 2.8: (a) Experimental layout of model Tay [114]. (b) Realistic experimental setup [109-111].

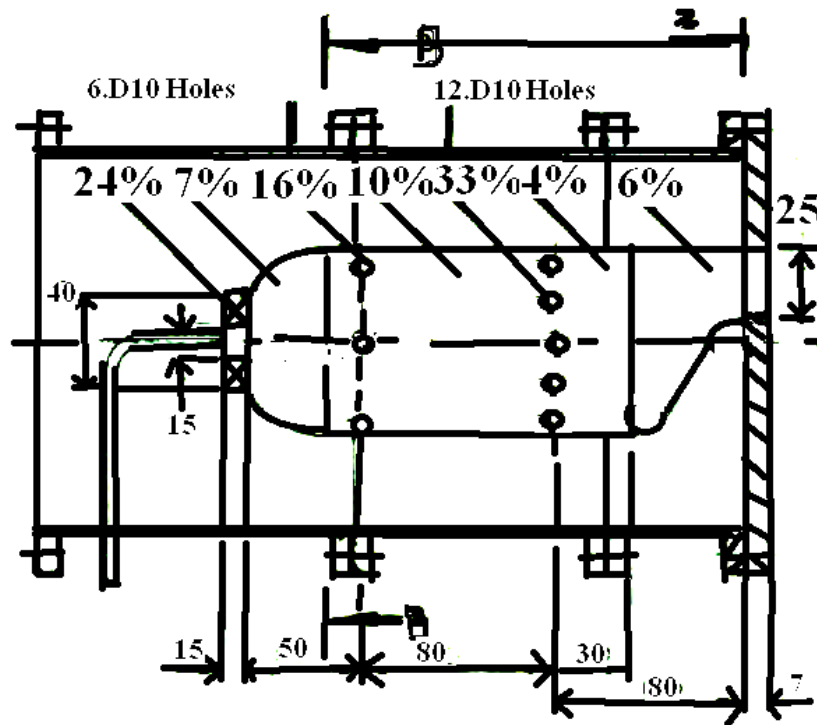
Most of the relevant experimental data in the literature have used industrially representative combustor geometries from can type combustor due to the ease of design, maintenance, and testing to more complicated modern combustors. In 1986, Heitor and Whitelaw [110] reported both isothermal and combusting flow characteristics of a can type gas turbine combustor (Figure 2.8). It was shown that in the primary region, combustion increased the strength but decreased the width of the CRZ whereas in the downstream region, combustion attenuated the magnitude and strength of swirl due to the axial acceleration of the flow. Very strong chemical non-equilibrium was noticed in the primary region where physical rather than chemical kinetic processes dominated the combustion. A partial equilibrium model was employed to predict the main scalar quantities in the primary region of the combustor where the fuel rich mixture, which exceeded the flammability limit, was assumed to be diluted with pure fuel. Although the main scalar quantities and

temperature were captured reasonably accurately, it was speculated that to predict pollutant concentrations better, flamelet methods might offer a better choice. In downstream locations, the local non-equilibrium became more severe and a constrained equilibrium model (such as a stretched flamelet method) was needed.

In 1988, to understand the combustion characteristics further, Tse [118] carried out experimental studies (Figure 2.8a) in both annular and can-type combustors. The can-type combustor possessed the same geometry as the combustor used by Jones and Toral [109], Heitor and Whitelaw [110], and Bicen and Jones [111], although a smaller swirler was used to achieve a more fuel rich condition in the primary region of the combustor. The nature of the flames with these two swirlers (Figure 2.9) was thus different, with the large swirler unable to retain the flame in the primary region. With the smaller swirler, the flame in the primary region was held by the stronger impingement of the primary jets, which then contributes more to the CRZ. To improve the understandings of this combustor, many subsequent studies have been conducted in both experimental and computational areas.



(a)



(b)

Figure 2.9: Air flow split of the model Tay combustor. (a) Small swirler configuration [114]. (b) Large swirler configuration [109-111].

Bicen et al [114] compared the performance of the two different swirlers combustors and realised that a reduction of swirl flow from 25% to 7% increased the combustion efficiency by 19%, attributing this to a more complete consumption of fuel in the primary region (for the same air-fuel

ratio). An increased amount of air from the primary jets was observed to contribute to the combustion process since the radial penetration of these jets increased from 50% (larger swirler) to 100% of the combustor radius. A numerical study using the chemical equilibrium assumption showed that in the fuel-rich primary region of the combustor, the CO and H₂ levels were over-predicted by up to five and seven times.

In a succeed investigation, Bicen et al [119] carried out experiments at two different air fuel ratios and swirl numbers. It was shown that the CRZ in the primary zone was driven by the combined effects of primary jets and swirl air. The air injected through swirler, porous wall and primary jets was insufficient to dilute the central parts of the primary region that the predominantly fuel rich conditions were diluted. More importantly, it was noted that the upstream flow of primary jets was decreased by 60% when a lower air-fuel ratio and weaker swirler were used.

In 1992, McGuirk and Palma [112] summarised the influence of numerical parameters in simulating the same combustor. The inlet boundary conditions were carefully examined and improved boundary conditions were proposed when no experimental data were available. The contribution of this work will be discussed further in **Chapter 4** since the current work employed the same boundary conditions.

Jones in 2002 [117] employed the computationally very expensive large eddy simulation (LES) method and a non-premixed combustion model (mixture fraction, zero stretching SLFM and a presumed Beta-PDF shape) to predict the reacting flow in the same combustor, avoiding the infinitely fast chemistry

assumption employed in very simple models of chemical equilibrium (mixed is burnt) methods [110]. Due to inappropriate boundary condition for the fuel injector component, the temperature prediction in the primary region of combustor was far from the experimental results although better agreement was observed in the downstream region of the combustor.

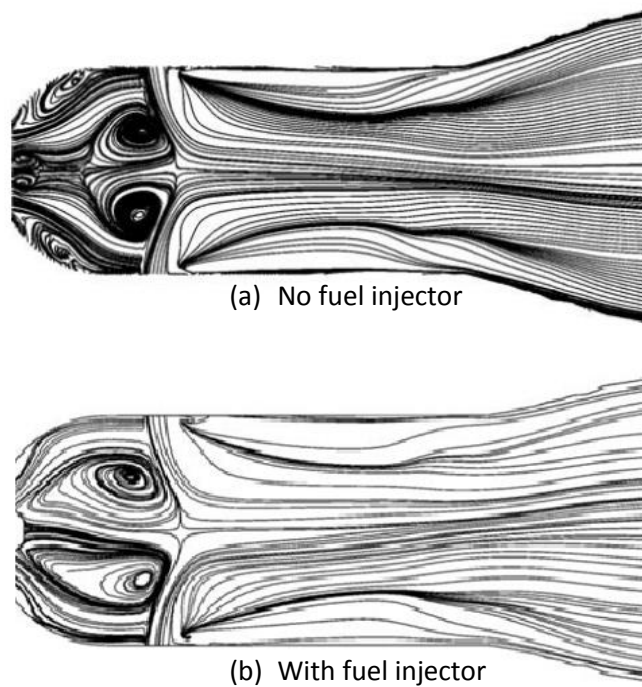


Figure 2.10: Velocity streakline with and without the fuel injector component sitting on the cone section of the can type gas turbine combustor. (a) Without fuel injector. (b) With fuel injector [115].

In 2004, Di Mare et al [115] improved the representation of the fuel injector flow in their LES predictions, employing same combustion model as Jones [117], and the resulted in better temperature agreement with experiment in the primary region. The predicted velocity streaklines in Figure 2.10 show two completely different CRZ flow fields with the two fuel injectors. However, despite the improvements achieved, the flame shape/pattern was still inconsistent with the experimental results that the side flame stripe observed in

their study was not seen in the experiment as shown in Figure 2.11. It was suggested that local extinction and re-ignition should be taken into account since the species concentrations near the fuel injector were badly predicted, especially for CO which was identified to be highly influenced by the ‘fast’ reaction assumption inherent in the SLFM method. A full report of this study can be found in the thesis of Di Mare [116].

Other than these, the recent prediction by Menzies in 2009 [120] again showed the difficulties of using a non-premixed combustion model in an SLFM method for predicting the reacting flow in the primary region (partially near fuel injector). Kriger et al in 2015 [108] also predicted the reacting flow in the large swirler combustor using the same combustion method and a (much cheaper than LES) Reynolds stress turbulence model (RSM), but predicted results were again far from experimental results.

Overall, as far as the author is aware, there have been no comparative studies between non-premixed combustion models (mixture fraction/flamelet method) and partially premixed combustion models (FPVA method) in spite of the fact that the former has not performed well and the latter has not been tested in a realistic gas turbine combustor problem.

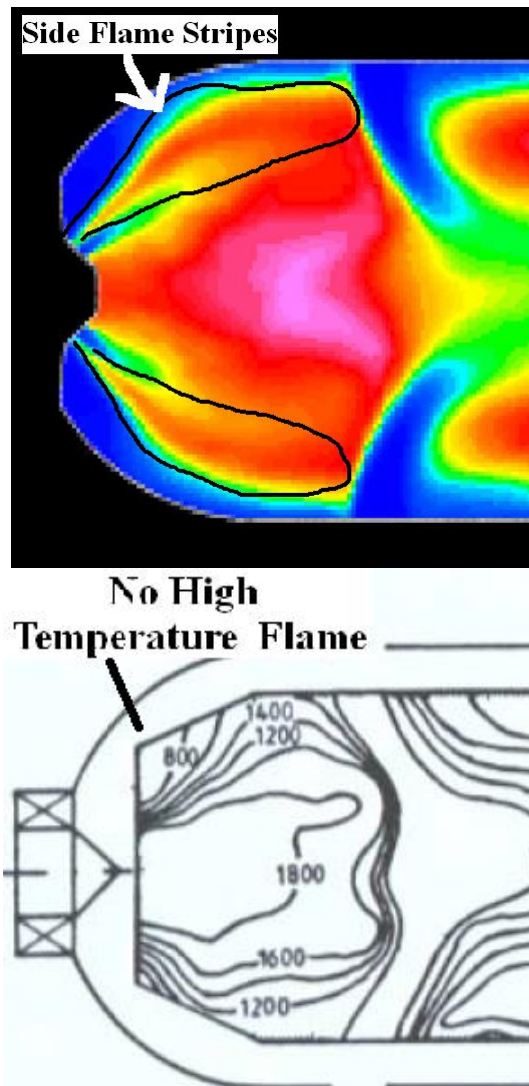


Figure 2.11: Temperature distributions from: (left) prediction (five levels between pink = 2200K and blue = 315K) [115], (right) experiment [114].

2.4 Turbulent Flow Simulations

Turbulent flow simulation, relying especially on partially resolved turbulent spectrum i.e. the large eddy simulation (LES) approach, has become an important research topic over the past few decades.

Despite the growth popularity of the LES, it has so far limited impact on industrial flow simulations because of its high-resolution requirement in high Reynolds number near-wall flows. In an attempt to reduce computational cost

and avoid the high resolution needed for LES in near-wall regions, an alternative method was proposed by Spalart et al [121-123], i.e. hybrid method of Detached Eddy Simulation (DES). This employs a Reynolds Averaged Navier-Stokes (RANS) in the attached boundary layer and an LES approach in detached flow regions. However, the explicit dependence on local grid spacing makes the implementation of this approach most easily realized in structured meshes. In other words, the switch between RANS and LES regions requires the comparison of predicted turbulent length scale in the RANS-approach with the local grid spacing. In complex geometry engineering flows, unstructured meshes are often used and this requires more practical DES-like approaches. Whilst these have recently become available, DES in unstructured mesh is still in the development stage.

As an alternative to LES, the scale adaptive simulation (SAS) methodology was derived by Menter et al [126] in 2003. This was based on Rotta's derivation of the transport equation for the two-point, two-time velocity correlation in 1950s [124, 125]. An exact transport equation for KL was developed from the two-point velocity correlation equation where K is the turbulent kinetic energy and L is the integral length scale of turbulence. The so-called K-KL model, based on Rotta's formulation was hardly used only recently due to several problems with the 2nd and 3rd order derivative of velocity appearing in the source term of KL transport equation. However, Menter et al [126] have proposed that Rotta's formulation can be used to allow the turbulence spectrum to be resolved down to the grid limit and to provide a smooth transition between RANS (stable flow regions with small variations of strain rate) and LES-like behaviour (unstable flow regions with large variation

of strain rate) without an explicit dependency on the local grid spacing as in the DES. The problem with the 2nd order derivative of velocity abandoned in the 1950s is recovered in Menter's approach, which was the main distinguishing factor of the model compared to traditional two-equation models.

Several case studies have been performed by Menter et al [127-132] showing the superiority of the SAS modelling approach. A linear dependence of the integral of $R_{ij,r}$ with respect to r on the 2nd order derivative of velocity was employed by Menter and Egorov [128] and a quadratic dependency was considered by Menter et al [132] to account for the inhomogeneity of turbulence. Two formulations of SAS-approach have been developed in the last decade. In 2004, Menter and Egorov [128] introduced the variable of \sqrt{KL} as an alternative to the length-scale equation as it provides direct proportionality to the eddy viscosity and is referred to as K square root KL model (KSKL). In 2005, an SAS-approach was reformulated for the use in conjunction with Menter's shear stress transport K-omega model [141] (SSTKW) and is referred to as SSTKWSAS. The SSTKWSAS model was used for two industrial applications in [131], the 3-D acoustic cavity and the ITS combustion chamber. For the 3-D acoustic cavity test case, the main acoustic modes were predicted to be in good agreement with experiment even though only coarse mesh was used.

The non-reacting and reacting flow in the ITS combustion chamber (a burner-like simple combustion chamber) was predicted with a partially premixed combustion model (premixed methane-air). Unsteadiness in the chamber was

introduced by the highly swirling flow at the chamber inlet. Although with only limited experimental data for comparison, the predicted temperature using the SSTKWSAS approach provided better agreement with experiment compared to the purely time-averaged SSTKW model.

In 2010, Mentor and Egorov [133] summarised the development of the SAS methodology and presented a few test cases. The test case of a periodic hill flow was presented as described in the LES study by Fröhlich et al [134]. The result showed the ability of the SAS approach to achieve solution from LES-like to RANS-like according to the pre-set time step size Δt and mesh resolution (the eddy viscosity was auto adjusted accordingly). The second test case corresponding to flow separation around a triangular cylinder (experiment of Sjunnesson et al [135]) confirmed the ability of the SAS approach to provide a partially resolved turbulence spectrum down to the mesh and time step resolution. For coarse mesh or large time steps, SAS automatically reverts to a RANS mode and was shown to provide a convenient path below this and in scale-resolving flow simulations.

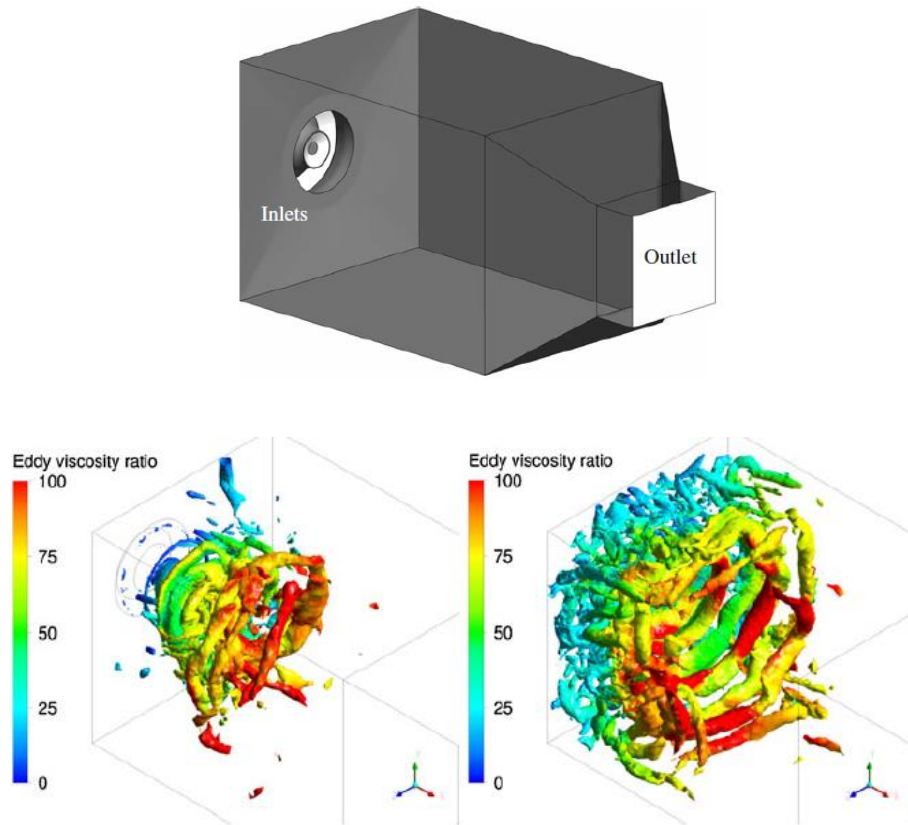


Figure 2.12: SSTKWSAS simulation for ITS combustion chamber. Top: Configuration. Bottom left: Q-criterion of Non-reacting flow. Bottom right: Q-criterion of Reacting flow [136].

More complex engineering test cases were also presented by Egorov et al [136]; for example an internal flow with heat and mass transfer, buoyancy and combustion, an aerodynamic flow with massive separation and aero-acoustic applications. Large eddy structures in a reacting and a non-reacting combustor-like burner test case (see Figure 2.12) proved the capability of SAS approach to resolve turbulent large scale unsteadiness. Lower eddy viscosity predicted by SSTKWSAS model in an aerodynamic flow test case (Figure 2.13) presented superior performance of this model compared to conventional SSTKW model. Turbulence kinetic energy cascades at a much lower rate compared to other RANS models.

Overall, it was shown that the SAS methodology can be employed in a wide range of engineering problems and that it provides qualitatively improved result compared to traditional RANS or URANS models. The SAS-approach was identified as a valuable method as it returns RANS solutions under the coarse mesh and large time steps, but has great advantages over existing hybrid RANS/LES methods such as DES.

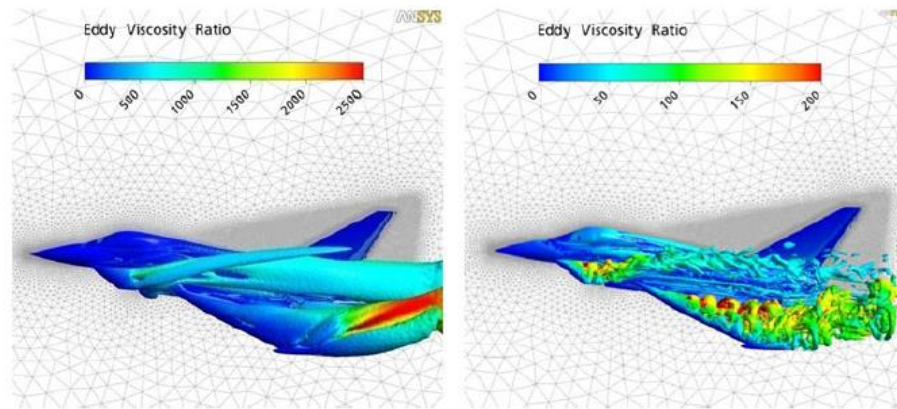


Figure 2.13: Q-criterion contour plot for aerodynamic flow, left: SSTKW model. Right: SSTKWSAS model [136].

Nevertheless, the engineering problem of interest here - turbulent combustion in an industrially representative combustor has so far not been simulated using SAS methodology. As far as the author is aware, except for the test case of above mentioned ITS combustion chamber [131], the only combustor that has been investigated using SAS was presented by Fossi et al [137]. The 3-D reacting turbulent two-phase flow field of a scaled swirl-stabilized gas turbine combustor was numerically simulated by the SAS approach and compared with solution from a URANS approach. The main flame trends predicted by the SAS approach coupled with tabulated flamelet based chemistry were seen to be reasonably accurate compared with the experimental result. URANS simulation using the same combustion model led to poor predictions of global

flame trends. However, both of the above simulations were conducted for geometrically simple combustor like burner configuration and these do not provide sufficient confidence of the capability of SAS for industrially representative combustors in which local extinction and re-ignition may appear more frequently.

In a recent work by Di Mare et al [115], an inconsistent flame shape was predicted comparing experimental data and LES results using non-premixed combustion model. Although predicted reacting flow fields in downstream locations were in better agreement with measurement, 26,432h of wall-clock time for one prediction using 64 processing elements in a Cray T3E computer makes LES not feasible for engineering design of industrial combustors although it should be realised that their work was done in 2004 and computer capability and cost-effectiveness have certainly increased.

In 2016, Zhang et al [138] predicted the same combustor using a Reynolds Stress Model (RSM) in conjunction with partially premixed combustion method. The flame shape in the primary region was in good agreement with experimental data, but temperature discrepancies were also observed. It was concluded that potentially by using a less dissipative scale-resolving simulation (SRS) method such as the SSTKWSAS model, the predicted temperature might be in better agreement with experimental result and the CPU time requirement for prediction would be far less than that required by LES.

Thus, based on the above review of the simulations of combustors, it is concluded that a study comparing URANS approach and a scale-resolving

simulation (SSTKWSAS) models of turbulence combined with a partially premixed combustion model (described below) would be a useful analysis to be carried out to demonstrate the capability of SAS methodology for this type of engineering flow. The previous Tay model combustor measurements were used as an excellent and well-defined test case for this study.

2.5 Overall Summary

Having discussed previous relevant experimental and computational works, a short overview is provided below as well as a list of defects/gaps and questions which remain to be answered:

Overview:

- In simple burner flames with no strong local extinction and re-ignition, various combustion models have been developed of which the most widely used are non-premixed combustion models such as SLFM and USLFM.
- The FPVA method was developed to overcome the defects of the SLFM and USLFM methods, which were identified as being inappropriate for strong local extinction and re-ignition combustion problems in swirling or lifted flames.
- LES method using SLFM have been tested to simulate a rich burn industrially representative can-type combustor and although reasonable downstream temperature agreement was achieved, the flame shape/pattern and the majority of species concentrations near the fuel injector were not correctly captured.

- RSM methods using SLFM have been employed to simulate a similar can type combustor that the predicted result was far from experiment across the whole combustor.
- Partially premixed combustion models such as the FPVA method or its variants have not yet been used in simulating industrially representative combustor so their performance is still unknown for such application.

Gaps/Defects and outstanding questions to be answered:

- How good is the partially-premixed FPVA method compared to the non-premixed flamelet method in simulating temperature and species concentrations in industrially representative combustors?
- How does the complex flow configuration in such combustors influence the different combustion mechanisms present? (e.g. the importance of local extinction and re-ignition, unburnt and burnt mixtures)
- How well does the progress variable approach embedded in the FPVA method control the chemical reactions in the primary region of the combustor?
- What is the performance of the variants of the FPVA method that have been proposed (the so-called flame surface area method and the turbulent flame speed method)
- How good are scale-adaptive simulation methods such as the SSTKWSAS model compared to Large Eddy Simulation (LES) in complex combustor flow and what are the trade-offs between accuracy

and efficiency?

- How do the SAS or RANS approaches influence the selection of the progress variable in FPVA method since a thin reaction zone assumption has been employed in the majority of combustion methods?

The present calculations are to answer the above questions and detail discussions are provided in **Chapters 5 and 6**.

Chapter 3

Mathematical Model

3.1 Introduction

In this chapter, the mathematical equations of several turbulence and combustion models are presented and discussed in terms of their merits and drawbacks in predicting realistic gas turbine combustor in which complicated turbulent combustion mechanisms are mixed together. The basic conservation equations for continuity, momentum and enthalpy share the general form:

$$\frac{\partial \rho \phi}{\partial t} + \nabla \cdot (\rho \vec{u} \phi) = \text{Source Terms} \quad (3.1)$$

Where ρ is the density and ϕ represents the conserved quantities. To account for highly unsteady turbulence effect in either reacting or non-reacting flows, Reynolds-averaging is usually applied to the general equation and models are required to provide closure to the unknown Reynolds stresses in non-reacting flow and the turbulent scalar fluxes in reacting flow resulting from the non-linearity of the convection term. Besides, the closure of the mean chemical reaction term is also one of the main difficulties in reacting flows.

In non-reacting flow, the majority of turbulence models employ the so-called Boussinesq eddy viscosity assumption to model the Reynolds stresses. The assumption for the 2nd order correlation states that the Reynolds stress tensor is proportional to the mean strain rate tensor taking the form:

$$\tau_{ij} = \overline{u'_i u'_j} = -\frac{\mu_t}{\rho} \left(\frac{\partial \overline{u}_i}{\partial x_j} + \frac{\partial \overline{u}_j}{\partial x_i} - \frac{2}{3} \frac{\partial \overline{u}_k}{\partial x_k} \delta_{ij} \right) + \frac{2}{3} k \delta_{ij} \quad (3.2)$$

Where μ_t represents the turbulent eddy viscosity in analogy to laminar viscosity and requires extra modelling. In reacting flow, a common practice to provide closure for turbulent scalar fluxes uses the gradient diffusion hypothesis:

$$\overline{u_i'Z'} = -\alpha_z \left(\frac{\partial \bar{Z}}{\partial x_i} \right) \quad (3.3)$$

Where α_z represents turbulent diffusivity and is defined as $\alpha_z = \mu_t / \rho \sigma_t$, and the turbulent Prandtl number σ_t usually takes the value of 0.85.

To calculate the turbulent eddy viscosity, traditionally two equation turbulence models have been employed with two extra variables to reflect the length and time scale of turbulent eddies, and to formulate the turbulent eddy viscosity. The two extra variables also have governing equations with the general form of equation 3.1 and are mainly classified into two groups: K-epsilon (KE) and K-omega (KW) turbulence models. The standard two-equation K-epsilon model proposed by Launder and Spalding [139] has been widely accepted for most practical engineering problems.

However, it is also accepted that the KE model lacks any mechanism to reflect the effects and behaviour of highly swirling flow. It is thus not employed in this thesis due to the presence of swirling motion in the simulated combustor. Instead, three turbulence models are employed: SSTKW (Shear stress transport K-omega) [141], RSM (Reynolds stress model) [143] and SSTKWSAS (K-omega, shear stress transport, scale adaptive simulation) [133]. Their merits and drawbacks will be discussed in the next section

followed by a very detail description of the mathematical formulation of non-premixed and partially premixed combustion models.

In this thesis, a chemical kinetic scheme of 244 chemical reactions and 50 species as recommended in [140] is employed to simulate propane-fuel combustion in an industrially representative gas turbine combustor by using species and temperature profiles derived in a laminar opposed-flow diffusion flame and expressed in the mixture fraction space. The steady laminar flamelets are tabulated beforehand for scalar dissipation rate from a chemical equilibrium value of 0/s to a flame extinction/quenching value of 58/s. This avoids high computational power resources required if solving the species in physical space [15].

3.2 Turbulence Models

3.2.1 SSTKW model

The shear stress transport K-omega model (SSTKW) developed from the basis of the standard K-omega model shows superior advantages compared to standard K-epsilon model [141]. Instead of using turbulent dissipation rate as in the K-epsilon model, the SSTKW model employs turbulent vorticity (or turbulent frequency) to represents the time scale of turbulent eddies. The equations for the SSTKW model and the formulation of eddy viscosity are:

$$\frac{\partial \rho k}{\partial t} + \frac{\partial \rho k \bar{u}_i}{\partial x_i} = \frac{\partial}{\partial x_j} \left[\mu_{eff} \frac{\partial k}{\partial x_j} \right] + G_k - Y_k \quad (3.4)$$

$$\frac{\partial \rho \omega}{\partial t} + \frac{\partial \rho \omega \bar{u}_i}{\partial x_i} = \frac{\partial}{\partial x_j} \left[\mu_{eff}^* \frac{\partial \omega}{\partial x_j} \right] + G_\omega - Y_\omega + D_\omega \quad (3.5)$$

$$\mu_t = \frac{\rho k}{\omega} \frac{1}{\max\left[\frac{1}{\alpha^*}, \frac{S\Gamma_2}{a_1\omega}\right]} \quad (3.6)$$

Where G_k and G_ω represents the generation of turbulent kinetic energy and turbulent vorticity respectively. Y_k and Y_ω represent the dissipation of k and ω , and D_ω represents a cross-diffusion term due to the transformation of the standard K-omega model from the standard K-epsilon model. The main difference between SSTKW and the standard KW model is due to the use of two blending functions Γ_1 and Γ_2 in calculating μ_{eff}^* and μ_{eff} , where $\mu_{eff} = \mu + \mu_t/\sigma_k$ and $\mu_{eff}^* = \mu + \mu_t/\sigma_\omega$. μ_t is calculated according to equation 3.6, while σ_k and σ_ω represent the turbulent Prandtl numbers for k and ω . The formulation of μ_t reverts to the one in the standard KW model when the blending function Γ_2 equals to zero.

The calculation of the two Prandtl numbers in the SSTKW model also differs from the standard KW model by involving the blending function of Γ_1 :

$$\sigma_k = \frac{1}{\frac{\Gamma_1}{\sigma_{k,1}} + (1-\Gamma_1)/\sigma_{k,2}} \quad (3.7)$$

$$\sigma_\omega = \frac{1}{\frac{\Gamma_1}{\sigma_{\omega,1}} + (1-\Gamma_1)/\sigma_{\omega,2}} \quad (3.8)$$

Where $\sigma_{k,1}$, $\sigma_{k,2}$, $\sigma_{\omega,1}$ and $\sigma_{\omega,2}$ are model constants.

The two blending functions Γ_1 and Γ_2 are designed to activate a standard K-omega model in the near wall region, and a modified K-epsilon model away from the wall.

3.3.2 Reynolds stress model (RSM)

As an alternative to using the Boussinesq assumption to provide ‘closure’ to the Reynolds Averaged Navier-Stokes equations (RANS), the most widely used RANS model is the RSM model. The RSM model is developed to overcome the major defect of two equation models in which a scalar eddy viscosity is assumed.

With RSM, six Reynolds stresses τ_{ij} appeared the in 3D RANS equations and thus are solved directly with the help of an equation for the turbulent vorticity. However, the accuracy of this model is still limited by assumption made to close the Reynolds stress transport equations and by the seventh equation which implied a single time scale of turbulence: dissipation rate ε , or turbulent vorticity ω .

The transport equations for the Reynolds stress take the form:

$$\frac{\partial \rho \tau_{ij}}{\partial t} + \nabla \cdot (\rho \overline{u_k} \tau_{ij}) = D_{T,ij} + D_{M,ij} + P_{ij} + \phi_{ij} - \varepsilon_{i,j} \quad (3.9)$$

Where $D_{M,ij}$ is molecular diffusion, P_{ij} is stress production and these require no extra modelling. The other three terms: $D_{T,ij}$, turbulent diffusion, ϕ_{ij} , pressure strain and $\varepsilon_{i,j}$, dissipation all need to be modelled to close the equations.

The turbulent diffusion term is modelled as in equation 3.10, where the Prandtl number σ_k takes the value of 0.82 as suggested by Lien and Leschziner [142]:

$$D_{T,ij} = \frac{\partial}{\partial x_k} \left(\frac{\mu_t}{\sigma_k} \frac{\partial \tau_{ij}}{\partial x_k} \right) \quad (3.10)$$

The tensor $\varepsilon_{i,j}$ is modelled as:

$$\varepsilon_{i,j} = \rho\varepsilon \frac{2}{3} \delta_{ij} \left(1 + 2 \frac{k}{a^2}\right) \quad (3.11)$$

Where $a = \sqrt{\gamma RT}$ is the speed of sound, γ is the ratio of specific heats C_p/C_v .

ε is computed with a modified version of equation 3.5 by replacing ω with ε and changing the model constants to those in the standard K-epsilon model.

The eddy viscosity in this equation is computed from $\mu_t = \rho C_\mu \frac{k^2}{\varepsilon}$ where $C_\mu = 0.09$ and $k = \frac{1}{2} \overline{u'_i u'_i}$. Two methods for modelling the pressure strain term Φ_{ij} have been suggested in the past, a linear pressure strain model (RSM-linear) and a quadratic pressure strain model (RSM-quadratic). The former is used for the current work [143-145].

3.3.3 SST k-omega scale-adaptive simulation (SSTKWSAS)

Despite the capabilities of eddy viscosity and RSM in simulating many engineering flows, in their steady RANS formulations, they often do not perform well in flows that possess large scale unsteady features (e.g. high swirl flows) since all unsteadiness is averaged out in steady turbulence model based RANS. To overcome this problem and to relax the effect of computational high cost and sensitivity to mesh, the SAS-approach which was developed by Menter et al [126] and is of scale resolving simulation (SRS) approach is used in the current work. The approach has been demonstrated to provide a smooth transition between RANS and LES like behaviour without an explicit influence of mesh resolution on the RANS mode of this model.

The SSTKWSAS model is implemented on the basis of conventional two-equation SSTKW model and originates from the idea of Rotta's two-point, two-time velocity correlation [124, 125]. The macro/integral length scale and time scale are defined by re-formulating the transport equation for the correlation tensor R_{ij} (See Appendix A for a detailed derivation):

$$R_{ij}(x, t, r, \tau) = \overline{u'_i(x, t)u'_j(x^{(1)}, t^{(1)})} \quad (3.12)$$

$$L_{ij,k}(x, t) = \frac{1}{2\overline{u'_i(x, t)u'_j(x, t)}} \int_{-\infty}^{\infty} R_{ij}(x, t, r_k, 0) dr_k \quad (3.13)$$

$$T_{ij}(x, t) = \frac{1}{2\overline{u'_i(x, t)u'_j(x, t)}} \int_{-\infty}^{\infty} R_{ij}(x, t, 0, \tau) d\tau \quad (3.14)$$

Where $x^{(1)} = x + r$ and $t^{(1)} = t + \tau$. The transport equation for R_{ij} is derived by summing up the following pair of equations:

$$D^{(i)}\{R_{ij}\} = \overline{u'_j(x^{(1)}, t^{(1)})N_i\{x, t\}} \quad (3.15)$$

$$D^{(j)}\{R_{ij}\} = \overline{u'_i(x, t)N_j\{x^{(1)}, t^{(1)}\}} \quad (3.16)$$

Where $N_i\{x, t\}$ and $N_j\{x^{(1)}, t^{(1)}\}$ are the transport equations for the instantaneous velocity fluctuation at different times and positions.

With the aid of the transport equation for R_{ij} and invoking the definition of length scale in equation 3.13, the transport equation for $\emptyset = \text{KL}$ can be formulated in which the original von Karman length scale of $L_{vK} = \kappa \left| \frac{\partial u / \partial y}{\partial^2 U / \partial^2 y} \right|$ appears in a source term and is the major distinguishing factor of the SAS approach compared to traditional RANS models. The von Karman constant κ takes the value of 0.41. By transforming the transport equation for

\emptyset to the traditional SSTKW model, the newly reformulated equation of SSTKWSAS model differs from equation 3.4 and 3.5 by the additional SAS source term Q_{SAS} appearing in the ω equation:

$$Q_{SAS} = \max\left[\rho\eta_2\kappa S^2\left(\frac{L}{L_{vk}}\right)^2 - C \cdot \frac{2\rho k}{\alpha_\emptyset} \max\left(\frac{1}{\omega^2} \frac{\partial\omega}{\partial x_j} \frac{\partial\omega}{\partial x_j}, \frac{1}{k^2} \frac{\partial k}{\partial x_j} \frac{\partial k}{\partial x_j}\right), 0\right] \quad (3.17)$$

Where $\eta_2 = 3.51$, $\alpha_\emptyset = 2/3$, $C = 2$, and length scale of turbulence $L = \sqrt{k}/C_\mu^{1/4} \cdot \omega$ [133].

Moreover, in contrast to traditional two-equation models, the appearance of a source term including the original von Karman length scale provides an interesting source of turbulent length scale. It was observed in [133] that by having this term, a different and better behaviour of the URANS result can be produced for 2-equation closures. However, it was also observed that insufficient damping of the smallest unsteady scales leads to numerical instability. This occurs because that the predicted eddy viscosity is too small to dissipate the energy of the smallest eddies defined by the resolution of the mesh. To avoid this problem, a limiter Δ is calculated from the cubic root of the local cell size and used to reformulate the von Karman length scale and ensure that $L_{vk}^{new} > C\Delta$ [127].

3.3 Combustion Models

3.3.1 Mixture fraction theory

To predict turbulent diffusion flames using detailed chemistry, mixture fraction theory is one of the most popular methods. The method was originally derived from a single chemical reaction ‘laminar diffusion flame’ where the

conservation equations for mass fraction of fuel and oxidizer, and temperature can be written as:

$$\frac{\partial \rho Y_{fuel}}{\partial t} + \nabla \cdot (\rho u_k Y_{fuel}) = \nabla \cdot (\rho D \nabla Y_{fuel}) + \omega_{fuel} \quad (3.18)$$

$$\frac{\partial \rho Y_{ox}}{\partial t} + \nabla \cdot (\rho u_k Y_{ox}) = \nabla \cdot (\rho D \nabla Y_{ox}) + s \omega_{fuel} \quad (3.19)$$

$$\frac{\partial \rho T}{\partial t} + \nabla \cdot (\rho u_k T) = \nabla \cdot \left(\frac{\lambda}{c_p} \nabla T \right) + \frac{Q}{c_p} \omega_{fuel} \quad (3.20)$$

Where D is the diffusivity and λ is the thermal conductivity. The fuel reaction rate ω_{fuel} is related to the reaction rate for temperature by $\omega_T = -Q \omega_{fuel}$ where Q is defined as the heat released by the complete combustion of 1kg fuel. The fuel and oxidizer reaction rate are related by $\omega_{ox} = s \omega_{fuel}$ where s is the stoichiometric ratio. The Lewis number $Le = \lambda / \rho c_p D$ has been defined as unity in this thesis.

Combining equation 3.18 to 3.20, a general equation for a passive scalar may be derived for specific scalar quantities Z as:

$$\frac{\partial \rho Z}{\partial t} + \nabla \cdot (\rho u_k Z) = \nabla \cdot (\rho \alpha_Z \nabla Z) \quad (3.21)$$

Where the three quantities Y_{fuel} , Y_{ox} and T are related to the passive scalar by:

$$Z_1 = s Y_{fuel} - Y_{ox}; Z_2 = \frac{c_p T}{Q} + Y_{fuel}; Z_3 = s \frac{c_p T}{Q} + Y_{ox} \quad (3.22)$$

Passive Scalar	Fuel Inlet $Z_{i,fuel}$	Oxidizer Inlet $Z_{i,ox}$
Z_1	$s Y_{fuel}^0$	$-Y_{ox}^0$

Z_2	$\frac{C_p T_{fuel}^0}{Q} + Y_{fuel}^0$	$\frac{C_p T_{ox}^0}{Q}$
Z_3	$s \frac{C_p T_{fuel}^0}{Q}$	$s \frac{C_p T_{ox}^0}{Q} + Y_{ox}^0$

Table 3.1: Boundary conditions for passive scalars.

The three scalar quantities follow the same transport equation but have different boundary conditions as shown in Table 3.1 (Y_{fuel}^0 and Y_{ox}^0 are fuel and oxidizer mass fractions at flow inlets).

A normalized elemental mixture fraction is then defined as:

$$\mathbf{Z} = \frac{Z_i - Z_{i,ox}}{Z_{i,fuel} - Z_{i,ox}} \quad (3.23)$$

Where Z_i is the elemental mixture fraction for element i , the range of \mathbf{Z} is therefore from zero (when $\mathbf{Z} = Z_{i,ox}$) to unity (when $\mathbf{Z} = Z_{i,fuel}$). The mixture fraction transport equation can then be written similarly as:

$$\frac{\partial \rho \mathbf{Z}}{\partial t} + \nabla \cdot (\rho \mathbf{u}_k \mathbf{Z}) = \nabla \cdot (\rho \alpha_z \nabla \mathbf{Z}) \quad (3.24)$$

Where $\alpha_z = \mu / \sigma_z$, and the Prandtl number for \mathbf{Z} (σ_z) takes the value of 0.85.

Expressing \mathbf{Z} using the boundary conditions provided in Table 3.1 gives:

$$\mathbf{Z} = \frac{s Y_{fuel}^0 - Y_{ox} + Y_{ox}^0}{s Y_{fuel}^0 + Y_{ox}^0} = \frac{\frac{C_p T}{Q} + Y_{fuel} - \frac{C_p T_{ox}^0}{Q}}{\frac{C_p T_{fuel}^0}{Q} + Y_{fuel}^0 - \frac{C_p T_{ox}^0}{Q}} = \frac{\frac{C_p T}{Q} + Y_{ox} - s \frac{C_p T_{ox}^0}{Q} - Y_{ox}^0}{s \frac{C_p T_{fuel}^0}{Q} - s \frac{C_p T_{ox}^0}{Q} - Y_{ox}^0} \quad (3.25)$$

While, turbulence effects are not considered in above equations. In reality, turbulence always leads to the values of quantities such as temperature, mixture fraction, or velocity to deviate from their mean values. Hence, to

include turbulence effects into the above equations, either density weighted averaging method which has consider the density fluctuation or Reynolds averaging method can be used to re-write the above equations. The former method has been used for the simulations in the present work, and resulted in the following equations:

$$\begin{cases} \frac{\partial \bar{\rho} \bar{Y}_k}{\partial t} + \frac{\partial}{\partial x_i} (\bar{\rho} \tilde{u}_i \bar{Y}_k) = \frac{\partial}{\partial x_i} \left(\overline{\rho D \frac{\partial Y_k}{\partial x_i}} \right) - \frac{\partial}{\partial x_i} (\bar{\rho} \overline{u_i'' Y_k''}) + \bar{\omega}_k \\ \frac{\partial \bar{\rho} \bar{Z}}{\partial t} + \frac{\partial}{\partial x_i} (\bar{\rho} \tilde{u}_i \bar{Z}) = \frac{\partial}{\partial x_i} \left(\overline{\rho D \frac{\partial Z}{\partial x_i}} \right) - \frac{\partial}{\partial x_i} (\bar{\rho} \overline{u_i'' Z''}) \end{cases} \quad (3.26)$$

Where $\bar{\rho} \overline{u_i'' Z''}$ and $\bar{\rho} \overline{u_i'' Y_k''}$ are derived from the convection term. For simplicity, the symbol $\bar{\rho}$ is replaced with ρ and $\overline{u_i'' Z''}$ is replaced with $\overline{u_i' Z'}$ in the following sections although density weighted variables are always used..

3.3.2 Laminar flamelet theory (LFM)

The dependency of all species mass fractions on mixture fraction and temperature is such that $Y_k = f(\mathbf{Z}, T)$ (see equation 3.25) although it should be realized that this applies to instantaneous quantities. The actual dependency of temperature and species on mixture which defines the flamelet structure has not been provided and hence 1D-thin (large $\partial Y_k / \partial \mathbf{Z}$), laminar flamelets are assumed to be embedded in the turbulent flow field [15-17].

The flamelet structure can then be interpreted by transforming the transport equation for the equation 3.27 from physical space to mixture fraction space using the chain rule of differentiation $\left(\frac{\partial}{\partial t} = \frac{\partial}{\partial t} + \frac{\partial \mathbf{Z}}{\partial t} \frac{\partial}{\partial \mathbf{Z}} \right)$ and the continuity equation, and neglecting the gradient of species mass fraction along the flame surface $\frac{\partial Y_k}{\partial \mathbf{Z}} = 0$ (see Figure 3.1). This leads to equation 3.28.

$$\frac{\partial \rho Y_k}{\partial t} + \nabla \cdot (\rho u_k Y_k) = \nabla \cdot (\rho D \nabla Y_k) + \dot{\omega}_k \quad (3.27)$$

$$\rho \frac{\partial Y_k}{\partial t} = \dot{\omega}_k + \rho D \left(\frac{\partial Z}{\partial x} \frac{\partial Z}{\partial x} \right) \frac{\partial^2 Y_k}{\partial Z^2} \quad (3.28)$$

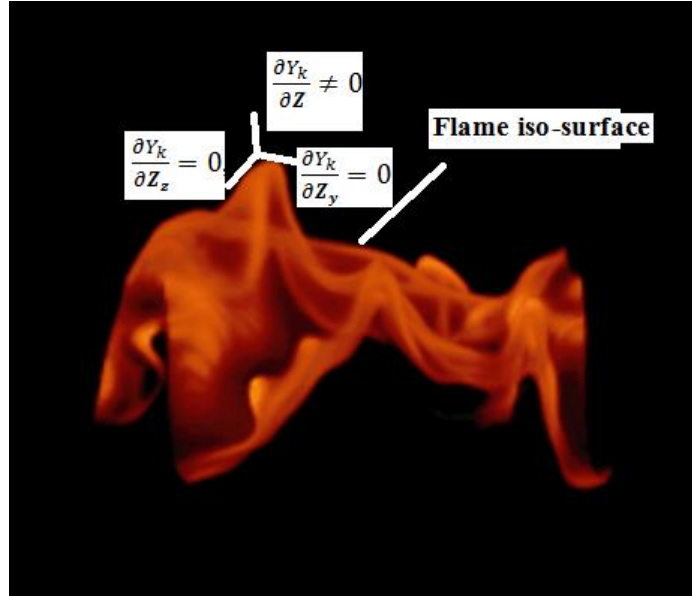


Figure 3.1: Laminar flamelet iso-surface, mixture fraction space.

The most often used flow field to study laminar flamelet in non-premixed flames is by the geometry consisting of opposed, axisymmetric fuel and oxidizer jets. If the velocity of jets is increased or the distance between the two jet inlets decreased, the flame is said to be strained and departs from chemical equilibrium. An increasing high speed of jets can extinguish the flame since this can introduce excess oxidizer which can blow the flame off if the diffusion rate is much higher than reaction rate. The strain rate is defined as $a_s = v/2d$ (v : jet velocity, d : distance between jets), but is often replaced by the scalar dissipation rate written as:

$$X = 2D|\nabla Z|^2 \quad (3.29)$$

Where D is the diffusion coefficient; Zero or low scalar dissipation represents the status of chemical equilibrium.

From equation 3.29, equation 3.28 can be re-written as:

$$\rho \frac{\partial Y_k}{\partial t} = \omega_k + \frac{1}{2} \rho X \frac{\partial^2 Y_k}{\partial Z^2} \quad (3.30)$$

The temperature equation can be written similarly as:

$$\rho \frac{\partial T}{\partial t} = \omega_T + \frac{1}{2} \rho X \frac{\partial^2 T}{\partial Z^2} \quad (3.31)$$

Thus, the diffusion flame is said to be controlled by two mechanisms: mixing and reaction. Equation 3.24 may be solved to describe the dependency of mixture fraction on space and time and equation 3.31 is solved to describe the rate of chemical reactions controlled by the diffusion rate of reactants into the flame reaction region and the scalar dissipation rate X , i.e. $T = f(\mathbf{Z}, X, t)$, $Y_k = f(\mathbf{Z}, X, t)$.

In steady laminar flamelet approach (SLFM), the first term on the L.H.S. of equations 3.30 and 3.31 is neglected. This approach is also applicable to fast chemical reactions, implying that turbulence-induced chemical non-equilibrium is mainly due to aerodynamic strain:

$$\begin{cases} \dot{\omega}_k = -\frac{1}{2} \rho X \frac{\partial^2 Y_k}{\partial Z^2} \\ \dot{\omega}_T = -\frac{1}{2} \rho X \frac{\partial^2 T}{\partial Z^2} \end{cases} \quad (3.32)$$

For an unsteady flamelet (USLFM), the first term is retained. As discussed in **Chapter 2**, SLFM and USLFM are often found to be of similar equally accuracy in predicting major species concentration and temperature

distribution in simple jet flames (no extinction and re-ignition), while the latter is more accurate in predicting fuel-lean flames and NO_x concentrations.

However, both methods lack mechanisms to account for local extinction and re-ignition due to the assumption of thin reaction regions and fast chemistry. To take into account of local extinction and re-ignition, the FPVA method is employed to allow the partially premixed combustion and will be discussed in **Section 3.3.5**. The SLFM method has been used in this thesis together with the employed 244 chemical reactions mechanism detailed in Appendix D.

3.3.3 Presumed probability density function (Presumed PDF)

The LFM described above produces a description of the species/temperature distribution in the flame structure as a function of the instantaneous mixture fraction. In order to account for turbulence-chemistry interaction, a presumed Beta-PDF method for \mathbf{Z} is employed in this thesis. Probability density function $p(\mathbf{Z})$ describes the likelihood of the fraction of time that is spent for the mixture fraction to occur in the range denoted by $\Delta\mathbf{Z}$ about any value of \mathbf{Z} . The area under the probability density function over the range $\Delta\mathbf{Z}$ is equal to the fraction of time that the mixture fraction is located in the band of $\Delta\mathbf{Z}$ (Figure 3.2). A mathematical equation can therefore be written as:

$$p(f)\Delta\mathbf{Z} = \lim_{T \rightarrow \infty} \frac{1}{T} \sum_i t_i \quad (3.33)$$

Where T is the total time scale and the sum of t_i in the range of T defines the total amount of time the mixture fraction has spent in the range $\Delta\mathbf{Z}$.

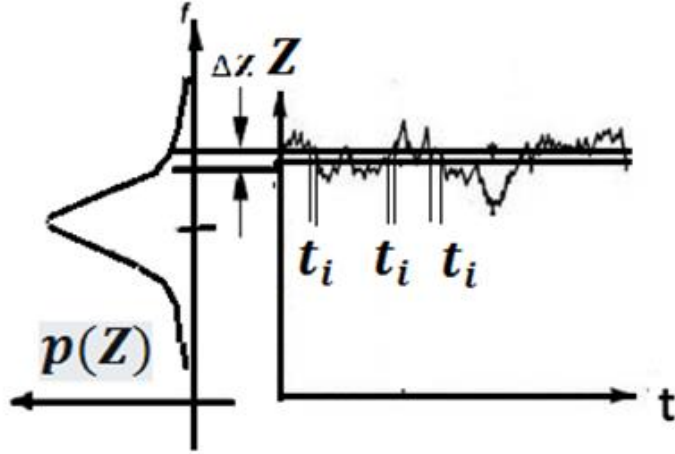


Figure 3.2: Probability density function definition.

Expanding this idea to the two variables PDF, $p(\mathbf{Z}, X_{st})$ then used to evaluate the time averaged-quantities which are dependent on \mathbf{Z} and X_{st} :

$$\begin{cases} \bar{T} = \iint p(\mathbf{Z}, X_{st}) T(\mathbf{Z}, X_{st}) d\mathbf{Z} dX_{st} \\ \bar{Y}_k = \iint p(\mathbf{Z}, X_{st}) Y_k(\mathbf{Z}, X_{st}) d\mathbf{Z} dX_{st} \end{cases} \quad (3.34)$$

The ideal gas law may then be used to calculate the time-averaged density:

$$\frac{1}{\bar{\rho}} = \iint p(\mathbf{Z}, X_{st}) \frac{1}{\rho(\mathbf{Z}, X_{st})} d\mathbf{Z} dX_{st} \quad (3.35)$$

The X_{st} is defined as the instantaneous stoichiometric scalar dissipation at $\mathbf{Z} = \mathbf{Z}_{st}$ and their relationship is provided as [15]:

$$X_{st} = \frac{SR * \exp(-2[\operatorname{erfc}^{-1}(2 * \mathbf{Z}_{st})])}{\pi} \quad (3.36)$$

Where SR is the aerodynamic strain rate defined as in opposed, axisymmetric fuel and oxidizer jets. The use of X_{st} rather than X is to link the aerodynamic strain rate with the stoichiometric mixture fraction which defines the thickness of reaction zone. The increase of strain rate will increase the gradient of stoichiometric mixture fraction since when flame is strained the width of the

flame reaction zone diminishes. When X_{st} approaches zero, the chemistry is recognized as in equilibrium and local quenching/extinction appears when $X > X_{st,critical}$.

The 2D PDF $p(\mathbf{Z}, X_{st})$ used in this thesis assumes statistically independency between \mathbf{Z} and X_{st} , i.e. $p(\mathbf{Z}, X_{st}) = p(\mathbf{Z}) * p(X_{st})$. Although this assumption seems crude, it is believed that sufficient accuracy has often been achieved. The Beta-PDF method has been used in this thesis so that the shape of $p(\mathbf{Z})$ is dependent on the mixture fraction \mathbf{Z} and its fluctuation $\overline{\mathbf{Z}'^2}$:

$$P(\mathbf{Z}) = \frac{\Gamma(a+b)\mathbf{Z}^{a-1}(1-\mathbf{Z})^{b-1}}{\Gamma(a)\Gamma(b)} \quad (3.37)$$

Where Γ is the gamma function and is defined as:

$$\Gamma(a) = \int_0^\infty \bar{\mathbf{Z}}^{a-1} e^{-\bar{\mathbf{Z}}} d\bar{\mathbf{Z}} \quad (3.38)$$

The two variables a and b are PDF parameters and are expressed as:

$$\begin{cases} a = \bar{\mathbf{Z}} \left[\frac{\bar{\mathbf{Z}}(1-\bar{\mathbf{Z}})}{\overline{\mathbf{Z}'^2}} - 1 \right] \\ b = (1 - \bar{\mathbf{Z}}) \left[\frac{\bar{\mathbf{Z}}(1-\bar{\mathbf{Z}})}{\overline{\mathbf{Z}'^2}} - 1 \right] \end{cases} \quad (3.39)$$

Equation 3.39 indicates that to determine the Beta function shape, an additional transport equation for mixture fraction variance $\overline{\mathbf{Z}'^2}$ must be solved:

$$\frac{\partial}{\partial t} (\rho \overline{\mathbf{Z}'^2}) + \nabla \cdot (\rho u_k \overline{\mathbf{Z}'^2}) = \nabla \cdot (\alpha_{z'} \nabla \overline{\mathbf{Z}'^2}) + C_g \mu_t (\nabla \bar{\mathbf{Z}})^2 - \rho \bar{X} \quad (3.40)$$

Where $\alpha_{z'} = \mu_t / \sigma_t$ and model constants σ_t (Prandtl number), C_g are defined to be 0.85 and 2.86.

A Dirac-delta function is applied to $p(X_{st})$ so that the fluctuation of X_{st} is neglected implying $p(X_{st}) = \delta(X_{st} - \overline{X_{st}})$ and the mean scalar dissipation is defined as $\overline{X_{st}} = C_d \overline{Z'^2} \varepsilon / k$ in which $C_d = 2.0$ [146]. The Dirac-delta function assumes that when $X_{st} - \overline{X_{st}} = 0$, $p(X_{st}) = +\infty$, when $X_{st} - \overline{X_{st}} \neq 0$, $p(X_{st}) = 0$. A more physical approach might be to use a log normal distribution proposed by Effelsberg and Peters [147] but it is not employed in this work.

	$\overline{Z_1}$	$\overline{Z_2}$	$\overline{Z_3}$
$X_1 = \overline{X_{st,1}}$ $\propto \overline{Z_1'^2} \varepsilon / k$	$\overline{T(\overline{Z_1}, \overline{Z_1'^2})}$, $\overline{Y_k(\overline{Z_1}, \overline{Z_1'^2})}$	$\overline{T(\overline{Z_2}, \overline{Z_1'^2})}$, $\overline{Y_k(\overline{Z_2}, \overline{Z_1'^2})}$	$\overline{T(\overline{Z_3}, \overline{Z_1'^2})}$, $\overline{Y_k(\overline{Z_3}, \overline{Z_1'^2})}$
$X_2 = \overline{X_{st,2}}$ $\propto \overline{Z_2'^2} \varepsilon / k$	$\overline{T(\overline{Z_1}, \overline{Z_2'^2})}$, $\overline{Y_k(\overline{Z_1}, \overline{Z_2'^2})}$	$\overline{T(\overline{Z_2}, \overline{Z_2'^2})}$, $\overline{Y_k(\overline{Z_2}, \overline{Z_2'^2})}$	$\overline{T(\overline{Z_3}, \overline{Z_2'^2})}$, $\overline{Y_k(\overline{Z_3}, \overline{Z_2'^2})}$
$X_3 = \overline{X_{st,3}}$ $\propto \overline{Z_3'^2} \varepsilon / k$	$\overline{T(\overline{Z_1}, \overline{Z_3'^2})}$, $\overline{Y_k(\overline{Z_1}, \overline{Z_3'^2})}$	$\overline{T(\overline{Z_2}, \overline{Z_3'^2})}$, $\overline{Y_k(\overline{Z_2}, \overline{Z_3'^2})}$	$\overline{T(\overline{Z_3}, \overline{Z_3'^2})}$, $\overline{Y_k(\overline{Z_3}, \overline{Z_3'^2})}$
...

Table 3.2: A look-up table to correlate mean quantities with mean mixture fraction and its variance

Finally, a look-up table (see Table 3.2) can be built to correlate any mean quantities with the two variables \overline{Z} and $\overline{Z'^2}$ only. The mean mixture fraction and its variance ($\overline{Z'^2} = \frac{1}{C_x} \frac{k}{\varepsilon} \overline{X_{st}'}$) are used to determine different shapes of PDF and these shapes can thus be integrated to find the mean values for quantities such as species mass fraction and temperature.

3.3.4 Non-premixed combustion discipline

In the non-premixed flame, fuel and oxidizer are injected into the combustion chamber separately. The reaction rate is mainly controlled by the rate of mixing of fuel and oxidizer, and therefore, the generated flame is also called a diffusion flame. The non-premixed combustion is said to be a rate limited process as the regimes of modelling for such combustion require the consideration of both reaction time and mixing time, which are limited via the Damköhler number $Da = \tau_t/\tau_c$. Poinso et al [148] introduced a regime diagram for non-premixed flames according to the Damköhler number and the turbulence Reynolds number $Re_t = u'l_t/\nu$ as shown in Figure 3.3.

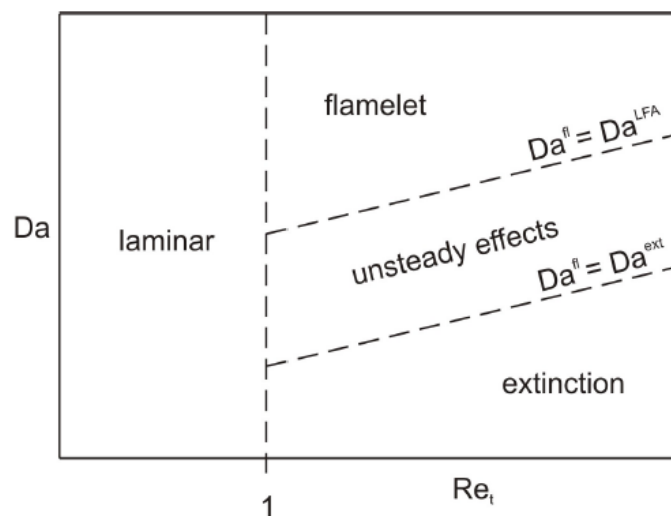


Figure 3.3: Regime diagram for non-premixed combustion [148].

The figure divides the turbulent non-premixed combustion problem into three regimes.

A) When the chemical reaction time is much smaller than the mixing time, i.e. for fast chemistry, the reactive layer of the flame is thinner than the diffusion layer. The smallest possible Kolmogorov size can only be equal to the

diffusion layer thickness and thus has no effect on the inner reactive layer, and the turbulent flame is assumed to be composed of laminar flamelets. The flamelet region is bounded by the flame Damköhler number and the Damköhler number of the laminar flamelet assumption (LFA), $Da^{fl} = Da^{LFA}$. The flame Damköhler number is defined by the ratio of flow time scale to chemical time scale, and the former can be estimated using the averaged scalar dissipation rate.

B) For larger chemical time scale, the reactive layer is thickened to the size of the Kolmogorov length scale, the LFA is no longer valid, and unsteadiness effects are to be expected.

C) When the chemical reaction is very slow, the fast diffusion of the mixture into the reactive layer leads to not combusted mixtures and the flame tends to extinguish. The extinction region is bounded by $Da = Da^{ext}$. The flamelet method is no longer valid as has been discussed previously in **Chapter 2**.

In this thesis, the fast chemistry assumption is made in regime A in Figure 3.3, the mixture fraction/SLFM combustion model is used for the simulation of turbulent combustion. The non-premixed combustion model has been widely used in simulating diffusion flames due to its relatively higher accuracy and efficiency though it is unable to predict extinction and re-ignition well.

3.3.5 Partially-premixed combustion discipline

To fully capture the turbulent combustion physics such as extinction and re-ignition, the FPVA approach has been used in this thesis as a partially premixed combustion model and its performance compared with that achieved from non-premixed combustion models.

The FPVA method is recognised as able to simulate local extinction and re-ignition in combustor-like burners as discussed in **Chapter 2**, although limited simulations have been done in realistic gas turbine combustor in which the local extinction and re-ignition can be very much stronger. A partially-premixed model is able to track two mixture status, either combusted or not combusted. For combusted mixtures, regime A in non-premixed combustion model is employed to decide the flame properties. For unburnt mixtures, a simple non-reacting mixing problem can be easily solved. The only question is how to decide the status of the local mixtures. To achieve this, an extra transport equation for the reaction progress variable is employed to track the flame front position.

The FPVA method compensates for the deficiencies of a non-premixed model since the mixture fraction contains no intrinsic information about the progress of chemical reactions. In FPVA, the local status of the mixture is distinguished includes the solving for the progress variable C with mean reaction rate $\bar{\omega}_c$. The transport equations for the mixture fraction and progress variable are:

$$\begin{cases} \frac{\partial \bar{\rho Z}}{\partial t} + \nabla \cdot (\rho \bar{u}_k \bar{Z}) = \nabla \cdot (\rho \alpha_z \nabla \bar{Z}) \\ \frac{\partial \bar{\rho C}}{\partial t} + \nabla \cdot (\rho \bar{u}_k C) = \nabla \cdot (\rho \alpha_c \nabla C) + \rho \bar{\omega}_c \end{cases} \quad (3.41)$$

Where $\alpha_z = \mu_t/\sigma_t$, and the turbulent Prandtl number σ_t takes the value of 0.85, $\alpha_c = \mu_t/Sc_t$ and the turbulent Schmidt number Sc_t takes the value of 0.7. The progress variable C is defined as:

$$C = \frac{\sum_{i=1}^n Y_i}{\sum_{i=1}^n Y_{i,eq}} \quad (3.42)$$

Where Y_i is the mass fraction of product species and $Y_{i,eq}$ is the equilibrium mass fraction for each product species. The density weighted scalar quantities such as species mass fractions in a thin flame can then be calculated from:

$$\bar{\phi} = C \int_0^1 \phi_b(\mathbf{Z})p(\mathbf{Z})d\mathbf{Z} + (1 - C) \int_0^1 \phi_u(\mathbf{Z})p(\mathbf{Z})d\mathbf{Z} \quad (3.43)$$

Where $p(\mathbf{Z})$ represents the presumed PDF (see equation 3.37). When C=1, mixtures are fully burnt so regime A in non-premixed combustion is adopted, when C=0, a pure mixing problem is assumed. In addition, when the mixture is fully burnt (C=1), the strained steady laminar flamelet method has been used as discussed above for ϕ_b , the density weighted scalar quantities are not only a function of mixture fraction, but also the scalar dissipation rate in equation 3.34.

In order to solve for C from equation 3.41, modelling must be provided for the mean reaction rate term $\bar{\omega}_c$. Five regimes (see Figure 3.4 and the detailed explanation in **Appendix B**) have been proposed to describe the behaviour of the flame under the influence of turbulence and chemical reaction. In this thesis, two regimes are employed to provide closure to the term $\bar{\omega}_c$, the Zimont Turbulent Flame Speed Closure Method or the Extended Coherent Flamelet Method (ECFM).

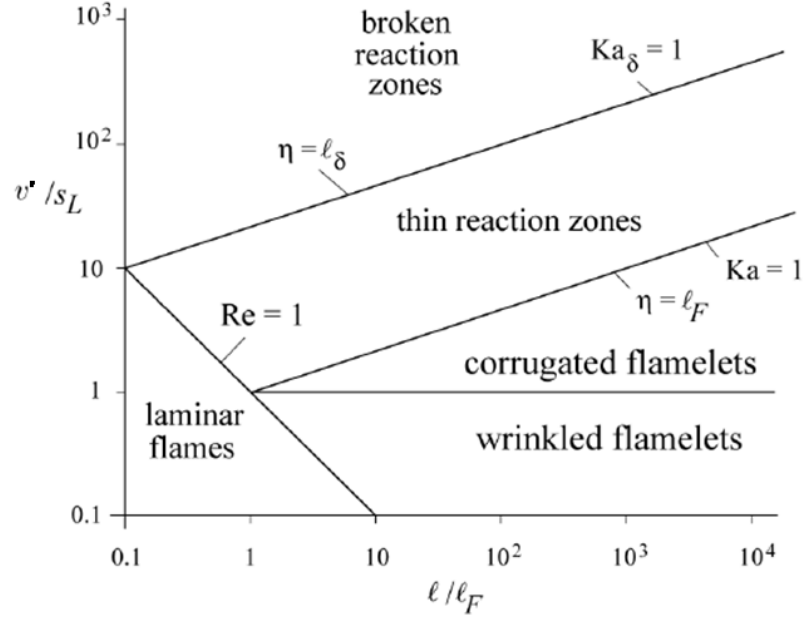


Figure 3.4: Regime diagram for premixed combustion [149].

Zimont Turbulent Flame Speed Closure (ZTFSC) Method: The mean reaction rate in equation 3.41 can be modelled as [150]:

$$\rho \overline{\dot{\omega}_c} = \rho_u U_t |\nabla C| \quad (3.44)$$

Where ρ_u is the density of the unburnt mixture and U_t is the turbulent flame speed which must be evaluated. The ZTFSC model belongs to a class of turbulent flame speed (TFS) model. Other models to decide TFS are available [15] but are not used here.

The ZTFSC method computes the turbulent flame speed by considering a wrinkled and thickened flame front which locates the regime in the region of thin reaction zones in Figure 3.4. The thin reaction zone regime assumes that the Kolmogorov size is smaller than the diffusion layer and penetrates the flame zone, but is still larger than the reactive layer, so the theory of laminar flamelets still applies. The thin reaction zone is quantified by a Karlovitz

number, Ka , larger than unity where Ka is defined as the ratio between the flame time scale and the Kolmogorov time scale. The ZTFSC method thus computes the turbulent flame speed via:

$$U_t = Au'^{3/4}U_l^{1/2}\alpha^{-1/4}l_t^{1/4} = Au'(\tau_t/\tau_c)^{1/4} \quad (3.45)$$

Where A takes the value of 0.52 as recommended by Zimont et al [150], and u' represents the root mean square (RMS) velocity. U_l , the laminar flame speed can be calculated either based on the fitted to correlation by Metghalchi and Keck [151] or from the curve fitted in Figure 3.5 the analytic approximation of the laminar flame speed predicted using a detailed kinetic mechanism of 82 elementary reactions [152]. The latter is used in the present work. α in equation 3.45 is the unburnt thermal diffusivity and l_t is the turbulent length scale calculated from $l_t = C_D k^{3/2}/\varepsilon$ (C_D equals 0.37), k represents turbulent kinetic energy, and ε represents turbulence dissipation rate.

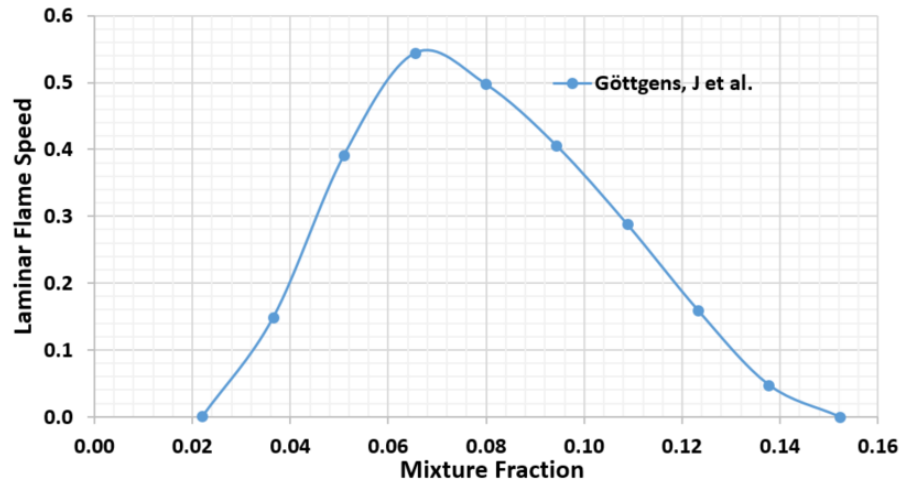


Figure 3.5: Laminar flame speed vs. mixture fraction [152].

The regime used by ZTFSC model is also called an Intermediate Steady Propagation (ISP) combustion regime where the flame front consumes fuel at

a speed proportional to the ratio between the turbulent time scale $\tau_t = l_t/u'$ and the chemical time scale $\tau_c = \alpha/U_l^2$. The stretch effect is considered in the ZTFSC model by multiplying $\rho\bar{\omega}_c$, the mean reaction term with a probability stretch factor G, details of this are not discussed here, but may be found in [153].

Extended Coherent Flamelet Method (ECFM): Having discussed the thin reaction zone regime used in the ZTFSC model, it is interesting to consider the region where Ka is smaller than unity in Figure 3.4. Two regimes of wrinkled and corrugated flamelets exist in this region and the ECFM approach is used to account for flame front corrugation by introducing a transport equation for flame area density (a flame area density method, FADM), denoted by Σ . For the wrinkled flamelets regime, the ratio of the local turbulence velocity fluctuation to the laminar flame speed is smaller than unity, indicating that turbulent eddies are unable to deform the flame front, and hence only slight wrinkling can occur. However, this is not valid for most engineering applications where the turbulent intensity is relatively large. The ratio of local turbulence velocity fluctuation to laminar flame speed is usually larger than one and the flame front is corrugated. In both of these regimes, the smallest turbulent eddies are assumed to be larger than the flame front thickness so the effect of turbulence is to wrinkle or corrugate the laminar flame sheet. As the reactive layer of the flame is not perturbed by the smallest eddies, the flame is quasi-laminar and the theory of laminar flamelets applies.

The increased flame area due to corrugation increases the fuel consumption rate and flame speed, and the transport equation for flame area density proposed in [154] is introduced to capture this effect.

$$\frac{\partial \rho \Sigma}{\partial t} + \nabla \cdot (\rho \overline{u_k \Sigma}) = \nabla \cdot (\rho \alpha_\Sigma \nabla \Sigma) + S_\Sigma \quad (3.46)$$

Where $\alpha_\Sigma = \mu_t / Sc_t$ and the turbulent Schmidt number Sc_t takes the value of 0.7. S_Σ is composed of four production terms and one dissipation term but details are provided in [154]. Various models have been proposed to close these terms, and the closure method provided by Colin et al [155] is employed in the present work. The computed flame area density is then used to provide closure to the mean reaction rate term $\overline{\dot{\omega}_c}$ in equation 3.41 using:

$$\rho \overline{\dot{\omega}_c} = \rho_u U_l \Sigma \quad (3.47)$$

More details of on how to calculate the fluid properties in the above equations are presented in **Appendix C**.

Chapter 4

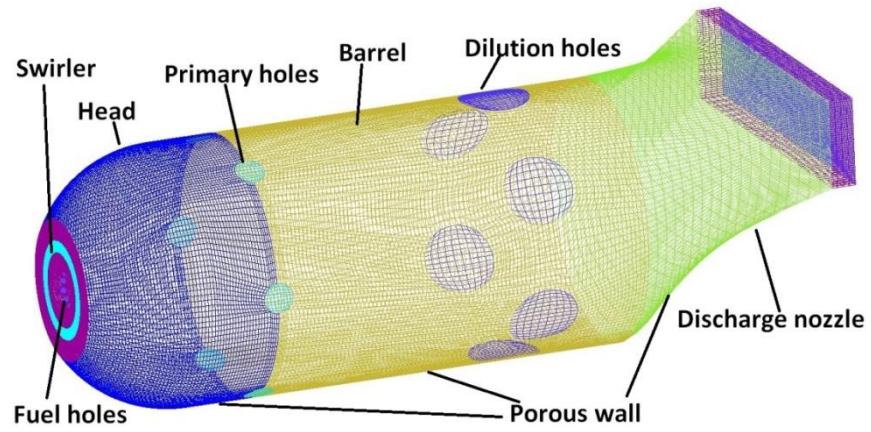
Numerical Methods and Experimental Configurations

4.1 Numerical Methods

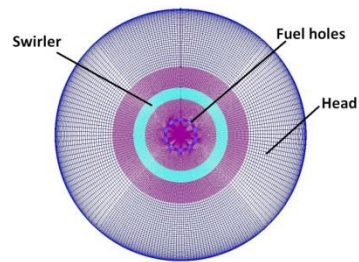
In this thesis, to simulate the gas turbine combustor flows effectively and efficiently, a segregated semi-implicit simple algorithm has been used in an incompressible pressure-velocity coupling scheme. The transport equations, which are density weighted, are solved using the commercial CFD code, Ansys Fluent 14.5 (a finite volume based method) [156]. Hexahedral rather than tetrahedral mesh is constructed using Ansys ICEM to improve the accuracy of prediction on a given mesh size (Figure 4.1).

Grid independence is checked by a mesh refinement strategy applied mainly in the primary region of the combustor (blue region in Figure 4.1a) where spatial gradients in flow properties are largest (unsteady RSM turbulence model and ZTFSC combustion model were used). The first refinement over 0.7 million mesh is performed in the region from $x=10\text{mm}$ to $x=40\text{mm}$ and the 2nd refinement is done by refining a smaller region from $x=10\text{mm}$ to $x=30\text{mm}$ (see dimensions in Figure 4.3). The number of the 3D cells is increased by a factor of eight each time the refinement is performed. Three meshes having 0.7, 1.2 and 2 million nodes are hence generated and tested, and the last one of 2 million mesh was chosen to ensure highest accuracy. Figure 4.2 shows a comparison of the temperature profile at $x=20\text{mm}$ (near the fuel injection nozzle) in the horizontal mid-plane of the combustor. The difference between 1.2 and 0.7 million mesh is not great, although the profile shape is different in

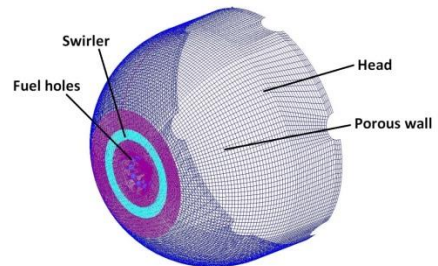
the central region probably due to convergence error (although convergence check by tracking velocity of a point in this region has not shown obvious errors) and the difference is smaller between 2 and 1.2 million mesh.



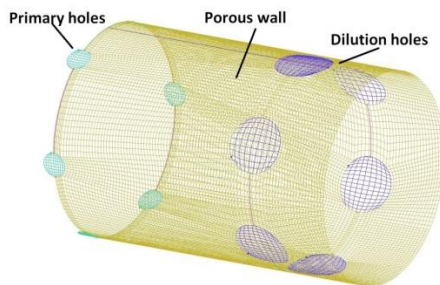
(a) Combustor



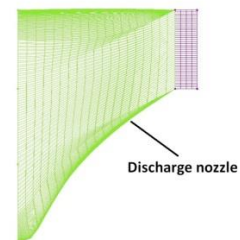
(b) Head (Left view)



(c) Head (Isometric view)



(d) Circular Barrel



(e) Discharge nozzle

Figure 4.1: Hexahedral mesh of geometry.

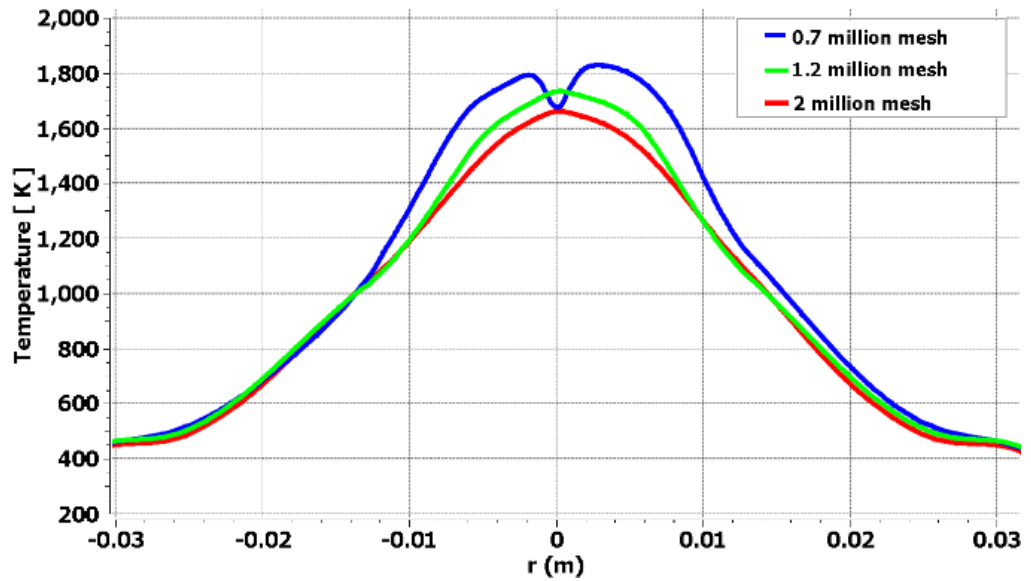


Figure 4.2: Grid independence study.

The current thesis presents the simulation of realistic can type gas turbine combustor in separate two sections or studies. First, the RANS (steady-RSM) model has been used whilst exploring different combustion models. Secondly, the SRS (SSTKWSAS) and URANS (unsteady RSM and SSTKW) models are employed combined with the combustion model found to be more accurate in the first study. The numerical methods used are similar for both studies: second order upwind has been applied to the progress variable, mean mixture fraction, mixture fraction variance for spatial discretisation method [157]. The bounded central differencing (BCD) scheme of Jasak et al [158] was used for momentum discretisation in the SSTKWSAS predictions, and the 2nd order upwind method in both RANS and URANS set of predictions. The different convection discretisation methods used is due to the fact that the SSTKWSAS model was found to predict lower eddy viscosity to the limit (allowing stability for eddies) supported by the grid resolution, which thus requires lower-dissipative numerical methods to ensure all dissipation experienced is due to the turbulence model itself.

Since transient simulations are carried out in the 2nd study, a bounded 2nd order implicit method is used for temporal discretisation. The residence time for the simulation is around 0.01s (see Di Mare [116]); the average cell size corresponding to the 2 million mesh is about 2.26e-5m, and the time step size is chosen to be 1e-04s, with a velocity magnitude at flame location of around 10m/s. This corresponds to a relatively large Courant number $CFL \approx 45$. Although this large time step size is used in the 2nd study, since the SSTKWSAS model does not explicitly depend on the local cell size, the model is seen to have provided a better performance than a traditional URANS simulation and certainly much less computationally expensive than LES simulation where a time step size of 1e-07 has typically been employed in the literature [116].

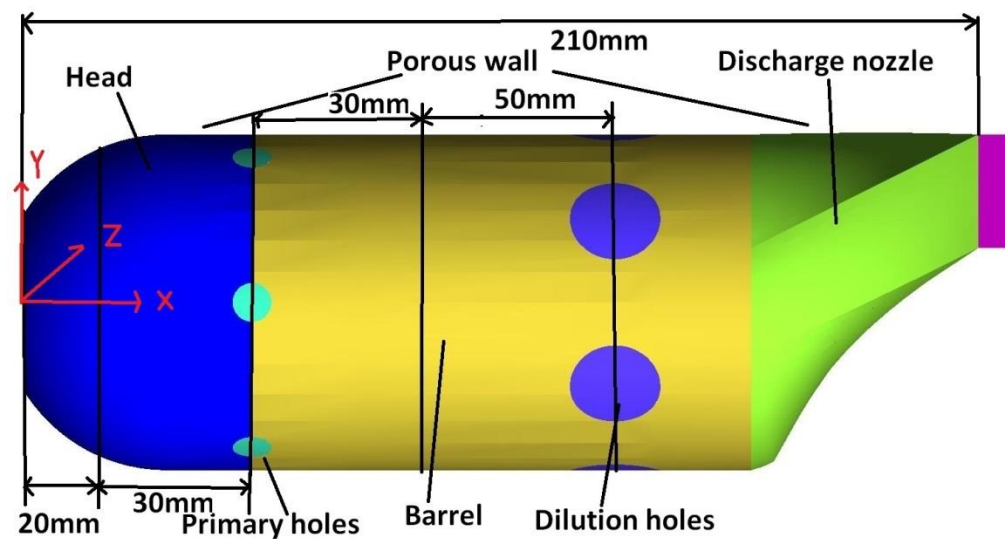
The computations employing the SSTKWSAS approach were carried out at City, University of London on a 20 processing element Solon cluster. A total wall-clock time of 160h was necessary to compute 16000 time steps (roughly equivalent to 160 turnover times) with the time-averaged statistics accumulated over 10000 time steps. Averaging starts after 100 turnover times and comparison of solution averaging after 140 and 160 turnover times show no differences, hence the averaged result over 160 turnover times is used.

The computations in the 1st study were carried out on the same cluster. The steady RSM model-based simulation greatly reduces the computational time, so that a total wall clock time of only 10 hours were spent for one prediction (2 million mesh). Past predictions based on LES require a total wall clock time of 26,432 hours using 64 processing elements of the Cray T3E at the

University of Manchester which is unaffordable in most industrial applications (1 million mesh) though this prediction was carried out in 2004 [115].

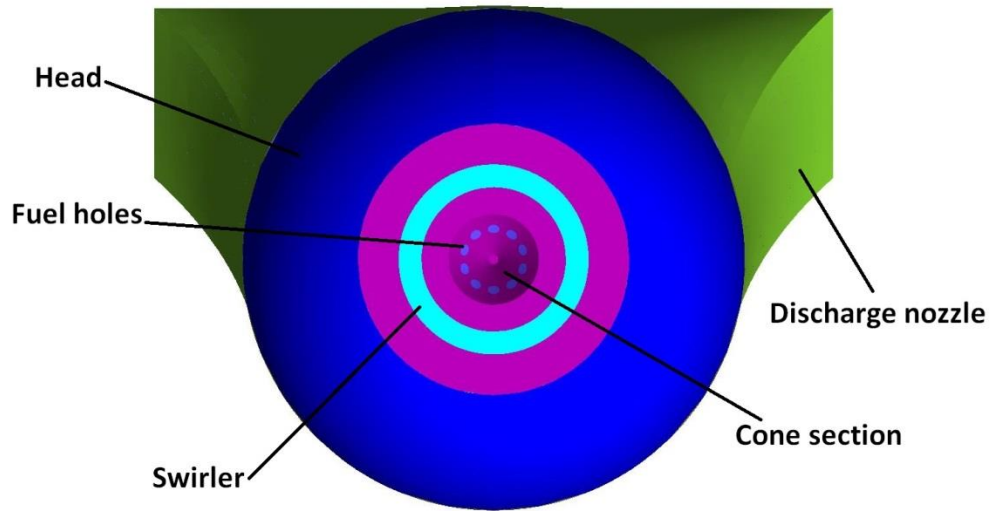
4.2 Experimental Configurations

Figure 4.3 shows the geometry of the model can-type combustor described in Bicen, Tse and Whitelaw [114]. It represents a reduced scale model of a Tay combustor retaining the essential components of the hemispherical head, cylindrical barrel, circular to rectangular discharge nozzle (dimension not reported in [114]), swirler, fuel device, primary holes and secondary/dilution holes. The wall of the combustor including head, barrel, and discharge nozzle are made of ‘Transply’, a kind of porous material.

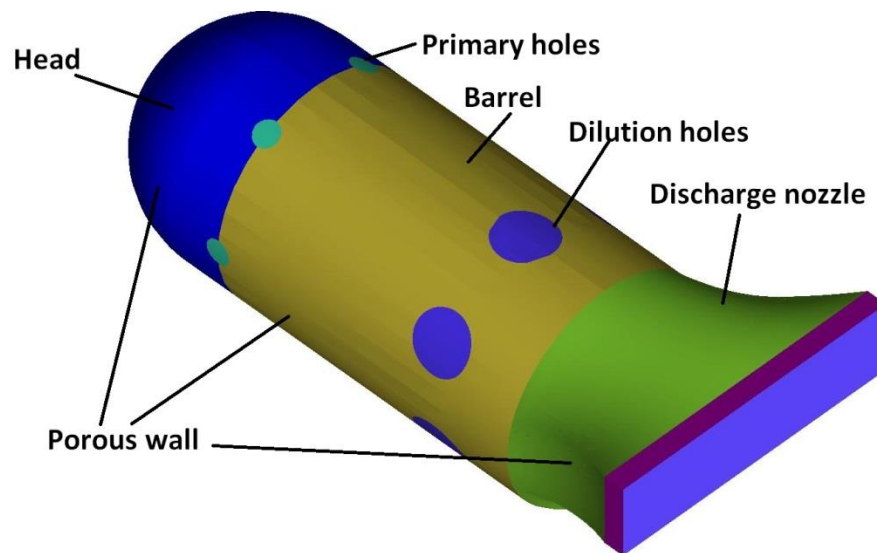


(a) Front view

Figure 4.3: Configuration of model can type combustor.



(b) Left view



(c) Isometric view

Figure 4.4: (Continued).

According to the experiment, six primary holes and six dilution holes are equally distributed around the cylindrical barrel of 75 mm diameter with the primary holes having a diameter of 10mm, and the dilution holes 20mm. However, it was shown by McGuirk and Palma [112] that the velocity profile of flow through the primary holes has a significant impact on the flow field in

the primary region. Different peak values of the flow profile assumptions of radial velocity in the hole affect the central part of combustor by promoting a stronger penetration of the jets. It was recommended in [112] that an artifice such as the reduction of the hole diameter by 14%, corresponding to a discharge coefficient C_D of 0.74 seems to be a good compromise given that no measurements are available about shape of the velocity profile. The use of a reduced diameter from 10mm to 8.6mm decreases the predicted maximum axial velocity for location closer to the injection nozzle and provides better agreement with the experimental data.

The swirler, mounted on the hemispherical head, comprises 18 curved vanes and designed with a thickness of 0.56mm. To reduce the complexity of meshing, the swirler vanes are not used by the current work. Instead, an annular swirler that is used such that the measured effective area at the swirler exit is reproduced and the corresponding axial velocity component determined via the known swirler mass flow rate. The tangential velocity ω is obtained by considering the turning efficiency of the vanes and associated blockage effects following the procedures for determining swirler boundary conditions suggested in [157, 159]:

$$\omega = \eta \frac{\dot{m}_a}{A_{se} \rho C_d (1-b)} \tan \theta \quad (4.1)$$

Where the blockage factor b is taken as 0.1, and the turning efficiency η is 0.92. A value of 0.75 is assigned to the discharge coefficient, C_d . The flow characteristics of the swirler used in the original experiment and the current predictions are available in Bicen and Palma [113]. The swirl number was calculated based on the equation for the straight vane swirler:

$$S = \frac{2}{3} \frac{1-(d_1/d_2)^3}{1-(d_1/d_2)^2} \tan\theta' \quad (4.2)$$

Where $d_1=10.64\text{mm}$ and $d_2=28\text{mm}$ are the inner diameter and outer diameter of the annular swirler, and θ' is the geometric real angle excluding the effects of blockage factors, discharge coefficient and turning efficiency. Thus, the swirler angle used is 54 degrees calculated via the ratio of tangential component of flow (0.809) and axial component of flow (0.588). The swirl number is around 1.01 corresponding to a high swirling strength.

The propane fueling device has 10, 1.7mm diameter holes equally distributed on the central cone section shown in Figure 4.3b and the velocity magnitude of the fuel jet is approximately 46.4m/s. Preliminary test calculations in [112] report some influence of the fuel hole distribution around the cone section on the symmetry of flow with respect to the combustor axis, but the effect of this has to be neglected here due to insufficient information about the exact positioning of the holes.

A summary of the experimental conditions used in this thesis is given in Table 4.1. According to the experiment, 6.9% of the total air flow was injected through the swirler, 13.6% through primary holes and 53.3% through dilution holes into the combustor. To simplify the porous wall problem, a fixed mass flow rate of 6.6% of the total air was assigned to the hemispherical head (blue), 13.8% to the cylindrical barrel (yellow), and 5.8% to circular to the rectangular discharge nozzle (green) (colours referring to Figure 4.3c). Table 4.2 shows the numerical boundary conditions used for the present simulations.

Exp	m_a	m_g	Swirler	P	T_{inlet}	AFR
	(g/s)	(g/s)	Vane	(atm)	(K)	
			Angle			
1	100	1.76	45°	1	315	57

Table 4.1: Experimental conditions [114].

	Primary jets	Dilution jets	Swirler jets	Fuel jets	porous wall jet (Head)	porous wall jet (Barrel)	porous wall jet (Nozzle)
m (Kg/s)	0.0136	0.0533	0.0069	0.00176	0.0066	0.0138	0.0058
T (K)	315	315	315	315	315	315	315
n_{O_2}/n_{N_2}	0.21/ 0.79	0.21/ 0.79	0.218/ 0.79	0.218/ 0.79	0.21/ 0.79	0.21/ 0.79	0.21/ 0.79
C_3H_8	-	-	-	1	-	-	-

Table 4.2: Numerical boundary conditions.

4.3 Reaction Mechanism and Look-Up Table

The propane air reaction mechanism used here consists of 244 chemical reactions and 50 species excluding the reactions for NO_x due to the inability of SLFM to capture slow chemical reactions. The full chemical reactions are given in Appendix D.

As explained in **Chapter 3.3.3**, a look-up table was built based on the scalar dissipation rate (or mixture fraction variance $\overline{X_{st}^2} = C_d \overline{Z'^2} \varepsilon/k$) and the mean mixture fraction. The relationship between temperature and mixture fraction is presented in Figure 4.4 which also shows the effects of scalar dissipation rate. A total of 60 flamelets were constructed for the current prediction starting with

an initial scalar dissipation of 0/s, followed by 0.01/s and increased with a step of 1/s until the flame extinguishes above the limit of 58/s.

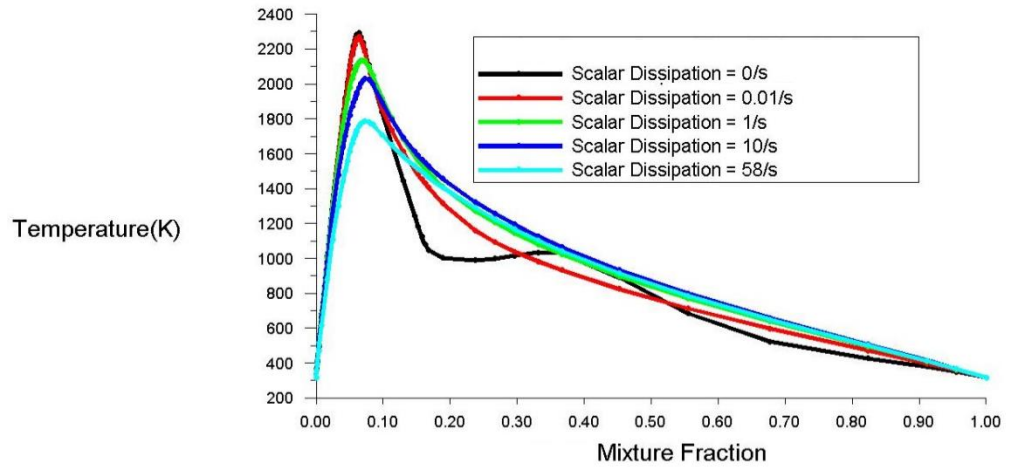


Figure 4.5: Relationship between temperature and mixture fraction at different scalar dissipation.

Chapter 5

Combustion Simulation in a Representative Rich Burn Gas

Turbine Combustor

5.1 Introduction

As discussed in **Chapter 2**, the non-premixed combustion model using mixture fraction/SLFM has been shown to perform well in simulating simple jet flames while flames such as lifted, piloted, and swirling flames with strong local extinction and re-ignition are not described well due to several unrealistic assumptions. An important defect of the non-premixed combustion model is that the chemical reactions, which are responsible for local extinction and re-ignition, cannot be detected by simple mixture fraction theory which does not account for the progress of chemical reactions or limit the chemical reaction rate. To solve this problem, the FPVA method has been designed and validated using many experimental jet flames data with great success.

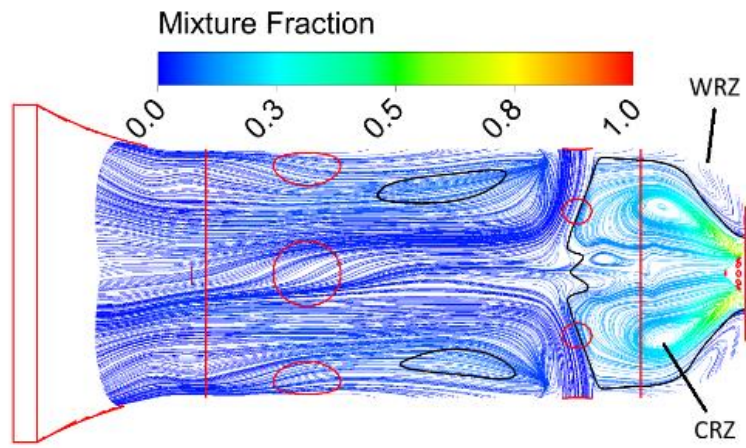
However, due to the limited experimental data and the difficulties of meshing an industrially representative gas turbine combustor, the method has never been applied to this problem. Past predictions (Jones [117], Menzies [120], and Krieger et al [108]) have all used the non-premixed combustion model approach (mixture fraction/SLFM) for prediction of complex gas turbine combustors. The flame shape in the primary region was not captured although good agreement with experimental data was achieved in the downstream combustor. It is likely that in such complex combustor, extinction and re-

ignition may appear much more frequently than that in simple jet flames. No investigations have been done to address these issues.

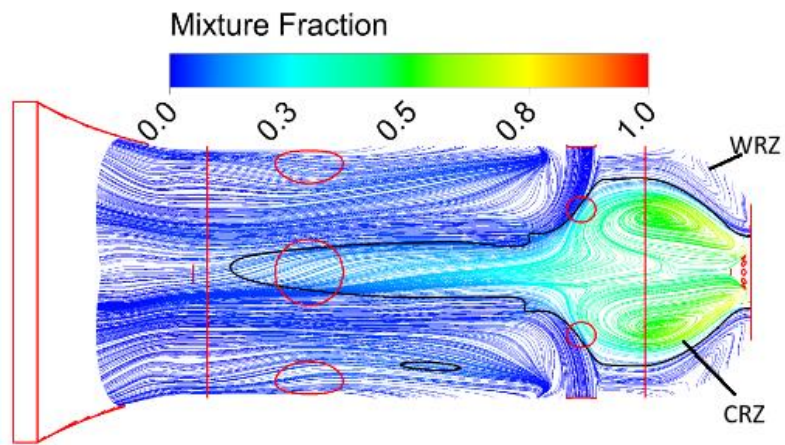
Thus, in this chapter, the steady RSM turbulence model is used together with different combustion models (both non-premixed and partially premixed) using the FPVA approach to simulate turbulent combustion in the chosen complex combustor test case to reveal the sensitivity to combustion model selection. The results presented in this chapter have already been published in the International Journal of Applied Thermal Engineering [138].

5.2 Behaviour of Flow Field and Scalar Variables

Streaklines of the velocity field coloured by mixture fraction are provided in Figure 5.1 for the horizontal mid-plane, and include the distribution of mixture fraction under the influence of the central recirculation zone (CRZ) and radially penetrating primary jets. The black lines display the position of stoichiometric mixture fraction. All three predictions clearly show the CRZ resulting from the phenomenon of vortex breakdown (swirling motion). The CRZ would extend further to the downstream in the combustor but is prevented by primary jets. In rich burn combustors, the primary jets are used to shorten the flame length and improve flame stability by reducing axial momentum and enhancing the intensity of CRZ. The intensive CRZ convects hot products to the upstream region of primary zone where cold reactants are then ignited to create flame stability. In addition to the large CRZ, narrower and thinner corner wall recirculation zones (WRZ) are also captured due to the sudden expansion of the combustor head geometry.

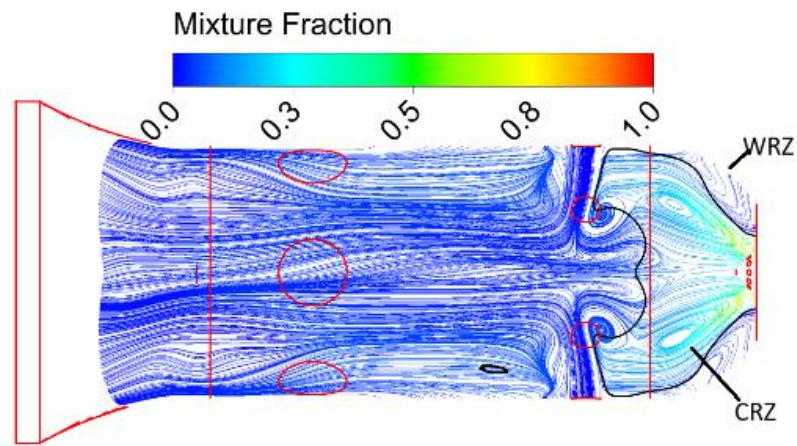


(a)



(b)

Figure 5.1: Streaklines of flow field coloured by mixture fraction. (a) ZTFSC model, (b) Non-premixed model, (c) ECFM model. Black solid line: stoichiometric mixture fraction=0.0639.



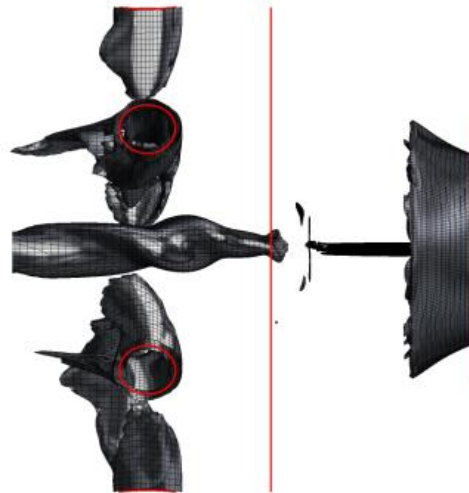
(c)

Figure 5.2: (Continued).

Although the two results from the partially premixed combustion models (ZTFSC and ECFM) show a similar mixture fraction distribution in the primary zone, some differences between them are still noticeable. The predicted CRZ size using ECFM is significantly smaller than the one predicted by ZTFSC. Since the energy trapped in the CRZ is initially generated by swirling jets, a smaller CRZ may indicate higher angular momentum and lower axial momentum. With lower axial momentum, the CRZ penetrates less downstream and is terminated sooner by primary jets. Also, two smaller vortices are formed just after the CRZ due to the high radial momentum of primary jets. On the other hand, with higher angular momentum, the increased intensity of CRZ has trapped more fuel in the primary region leading to a lower mixture fraction in the secondary zone (note the disappearance of the black solid line). The intensity of the CRZ in the primary region is illustrated better by the vorticity shown in Figure 5.2. The highly swirling core is broken

up in the ZTFSC prediction, while the ECFM result preserves the high angular momentum core throughout, which is believed to increase the flame stability.

In addition, since the main objective of this chapter is to demonstrate the performance of different combustion models, it is important to note the performance of the non-premixed combustion model in Figure 5.1b. This model performs completely different from the two partially premixed models. A large amount of fuel penetrates far downstream zone of the combustor without being recirculated back upstream. This difference is probably caused by the fact that the non-premixed assumption overestimates the reaction rate in the primary region while the partially premixed models employ a progress variable C which limits the reaction rate.



(a)

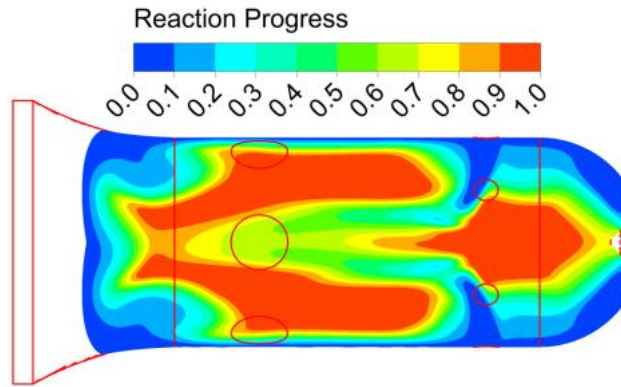
Figure 5.3: Intensity of CRZ in primary region represented by vorticity = $9776.83/s$ for (a) ZTFSC model, (b) ECFM model.



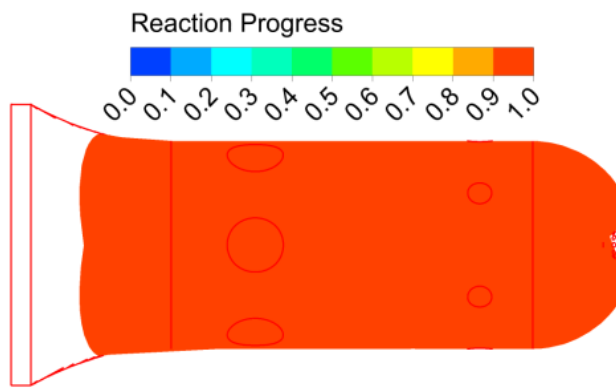
(b)

Figure 5.4: (Continued).

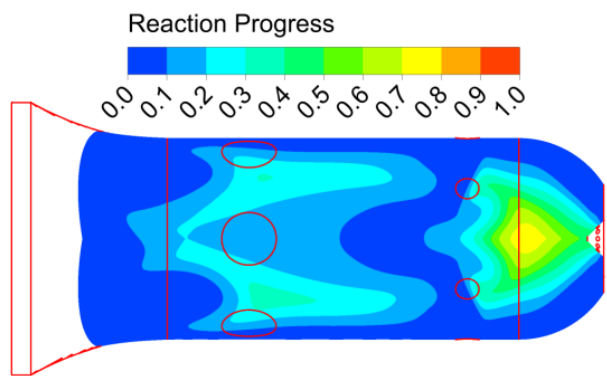
Figure 5.3 shows the progress variable (reaction progress) contours for all three combustion models. A reaction progress value of unity indicates the local mixture is fully combusted while zero represents no reaction. In the non-premixed combustion model, whenever fuel and air mix, combustion is effectively completed instantaneously. The reactions are fully progressed under this condition and thus the progress variable is assigned at unity implicitly. ZTFSC prediction using the FPVA method has limited reaction progress in the region closer to the porous wall where the inflowing cold air extinguishes the flame. A large amount of unburnt and burnt mixture co-exists in the entire region of combustor. With regard to the performance of the ECFM model, this predicted reaction in almost the whole primary region is limited, it is supposed that this is due to an underprediction of the strength of turbulence.



(a)



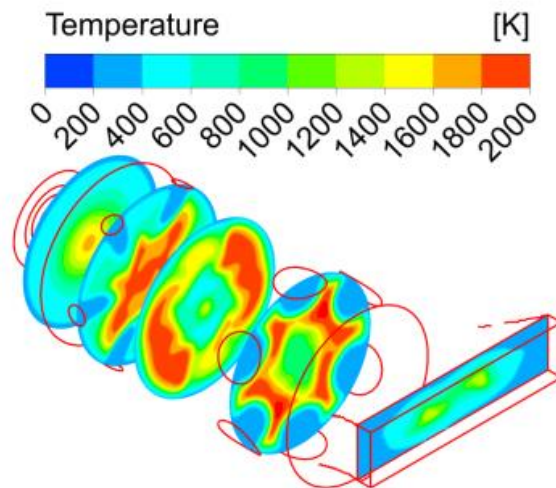
(b)



(c)

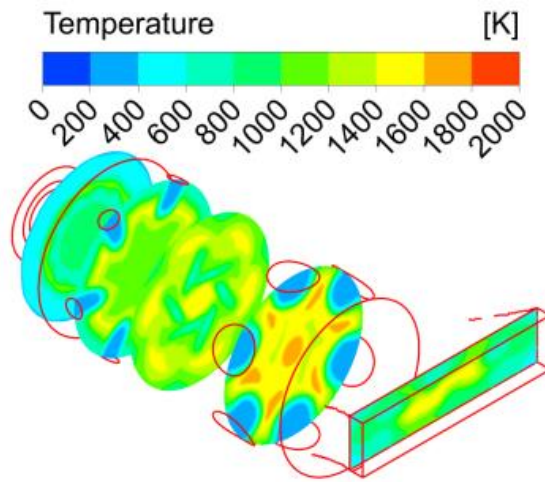
Figure 5.5: Progress variable (reaction progress) contour. (a) ZTFSC model, (b) Non-premixed model, (c) ECFM model.

The temperature contours on several axial planes of the combustor are presented in Figure 5.4 to further clearly discuss the impact of different combustion models. The predicted ZTFSC flame is mainly contained within the primary region of the combustor with part of the flame penetrating into the secondary region particularly near the combustor wall. No reaction processes actually reach the liner/combustor walls, which are protected by the cooling film formed by the cold injected air through the porous wall. The predicted flame with the non-premixed model penetrates quicker downstream in the combustor with the flame temperature near the secondary holes thus much higher than the temperature in the primary zone. Not surprisingly, due to the limited reaction progress predicted by the ECFM model (see Figure 5.3c), combustion does not seem to be properly captured by this model although the highest temperature does occur in the primary region (Figure 5.4c).

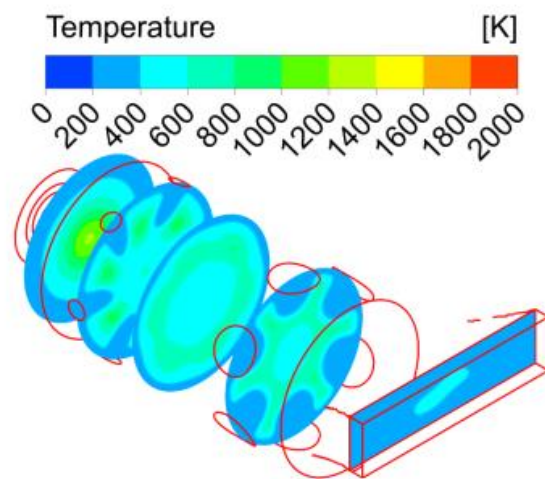


(a)

Figure 5.6: Temperature contours at axial position of 20mm, 50mm, 80mm, 130mm, and exit of combustor 210mm. (a) ZTFSC model, (b) Non-premixed model, (c) ECFM model.



(b)



(c)

Figure 5.7: (Continued).

In Figure 5.5, the predicted temperature from Di Mare et al [115] using large eddy simulation (LES) and a non-premixed combustion model is compared with the result by using a partially premixed model (ZTFSC) and the RSM model in this study. Although a large temperature difference near the combustor walls is observed and the LES results in Figure 5.5b show two side

flames compared to Figure 5.5a (RSM/ZTFSC), the highest temperature flame was in the primary zone and downstream of the primary jets. The main reason for this difference is most likely caused by the different combustion model chosen.

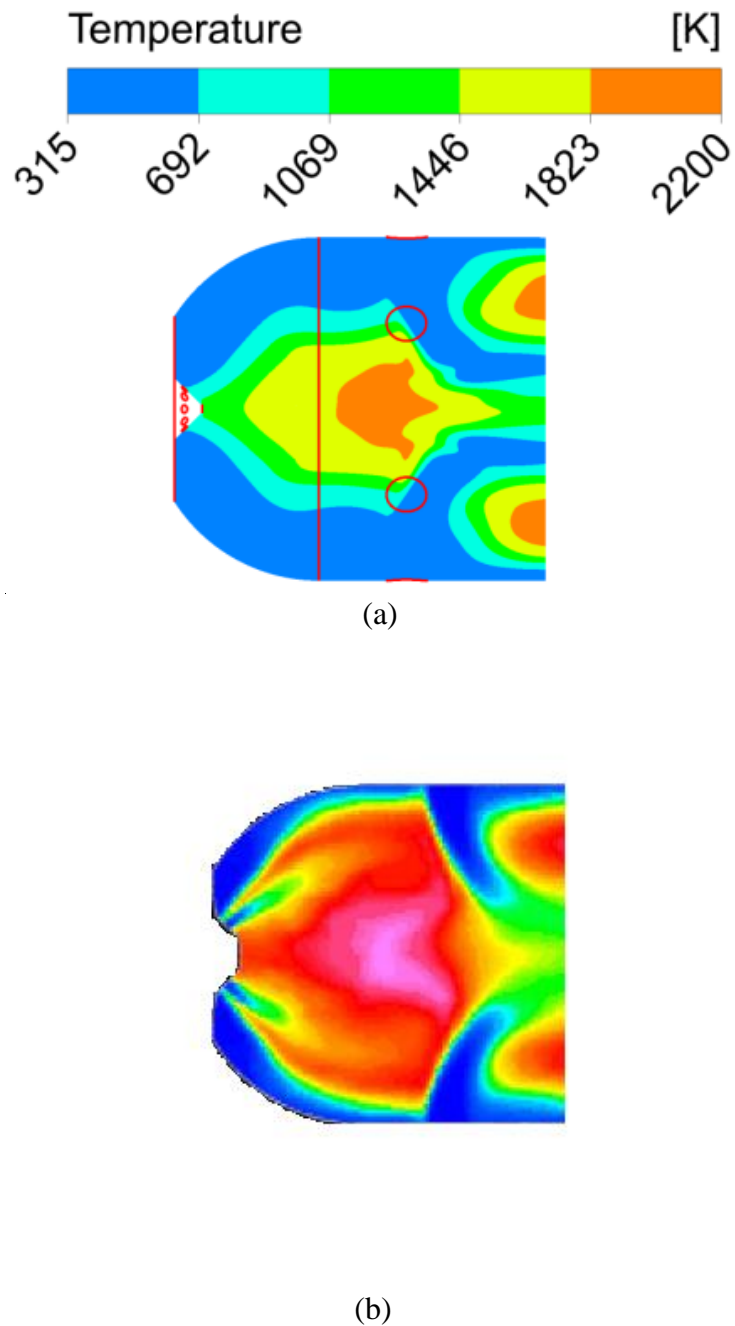


Figure 5.8: Temperature in the primary zone: horizontal midplane. (a) ZTFSC & RSM model, (b) LES & Non-premixed model, Colour scale: five levels between pink = 2200K and blue = 315K [115].

By examining Figure 5.3a at the position where the two side flames occur in the LES result of Figure 5.5b, the ZTFSC/FPVA presents a low progress variable of around 0.2~0.3. Such a low value of the progress variable indicates an unburnt or only partially burnt nature of the local mixture so it is not surprising that the present method predicts no side flames.

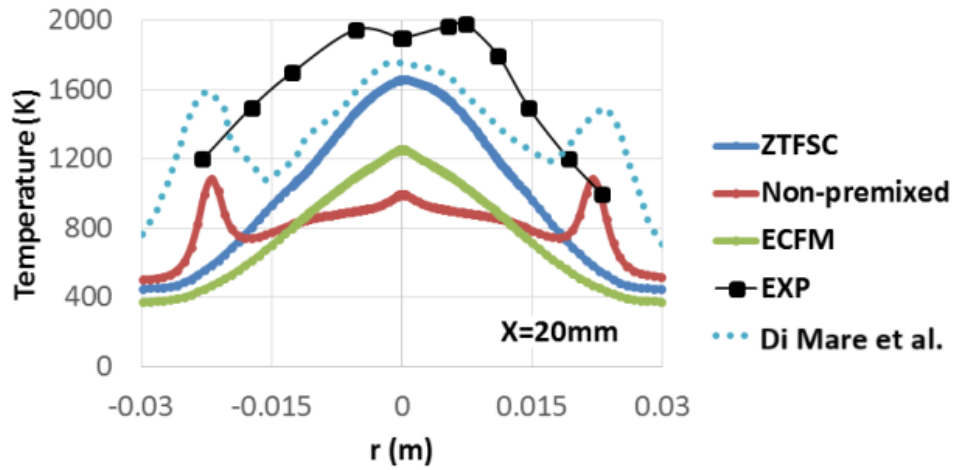
5.3 Statistical Results

In this section, statistical results from the present computations are discussed and compared with measurement [119], as well as the LES prediction of Di Mare et al [115]. Because of limited information about the precise geometry of the circular to rectangular transition nozzle at the rear of the combustor, only statistical results in the primary region are used for comparison. The flame in the primary region is of most interest to combustor designs and is the most difficult region to predict due to swirler and multi-jets. Proper prediction of the flame in this region is essential for accurate prediction in the combustor downstream region.

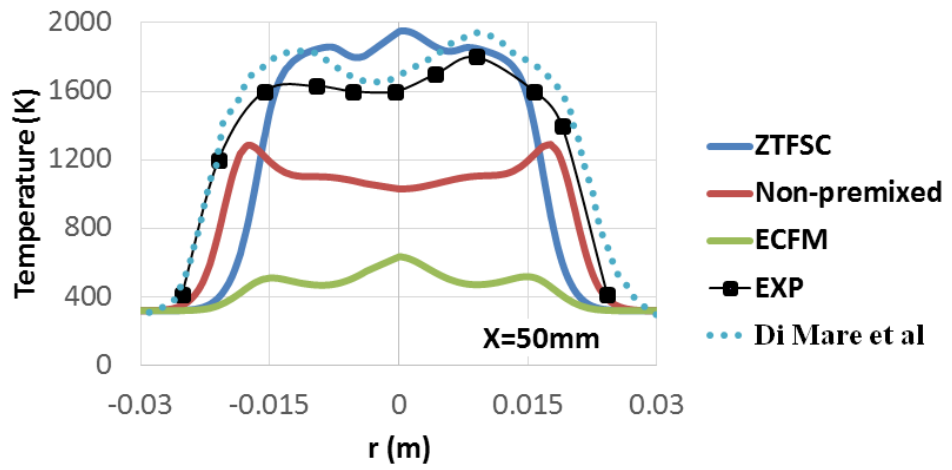
In Figure 5.6a, it can clearly be seen that the ZTFSC/ FPVA method predicts the temperature profile and thus the flame shape in reasonable agreement with the experimental result, although some underprediction is noticeable. The two partially premixed models show similar shapes while the flame shape achieved using the non-premixed model (mixture fraction/SLFM) in the current prediction and in Di Mare et al [115] are seen to be a similar shape (displaying the two ‘side-flame’ peaks). The non-premixed model obviously predict the incorrect flame shape since the experimental data only show the central peak in the temperature profile.

On the other hand, the partially premixed model is able to track the ability of local mixtures to limit reaction rate and therefore, the two side flames are not formed in complete agreement with measurements. The superior performance of the partially premixed model is attributed to its ability to account for the slow reaction rate of fuel and swirler air mixtures as well as the quenching effect of the cool air added through the porous wall.

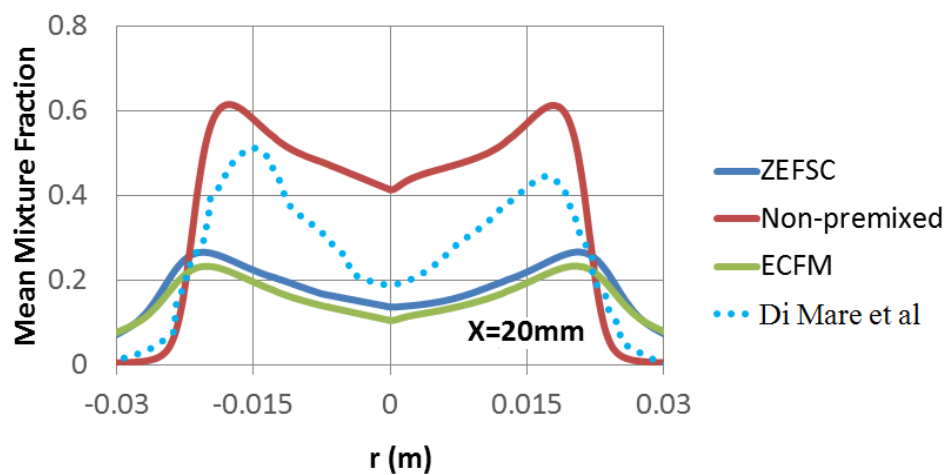
Due to the fact that the CRZ predicted by the RANS model is less intensive, more fuel exists near the primary holes without being recirculated to the upstream combustor region. This extra of fuel with the incoming primary air allowing combustion to happen at approximately the stoichiometric mixture fraction. Meanwhile, insufficient primary air is recirculated resulting in fuel rich combustion at $x=20\text{mm}$. Thus, the temperature predicted by the RANS model is higher than the LES [115] prediction (see Figure 5.6b). In addition, in Figure 5.6c, the mean mixture fraction predicted by the two partially premixed combustion models are seen to be the same, the temperature differences predicted can only be caused by the underestimation of progress variable by the ECFM model as shown earlier (Figure 5.3).



(a)



(b)

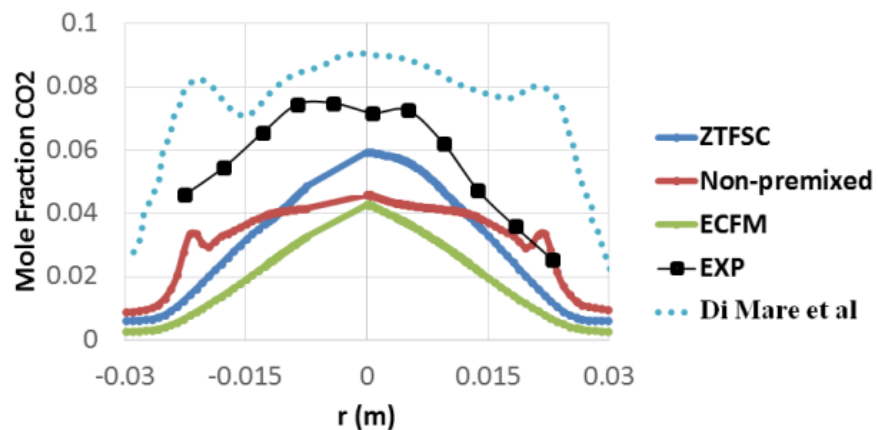


(c)

Figure 5.9: Profile of temperature and mixture fraction in the horizontal midplane of the combustor.

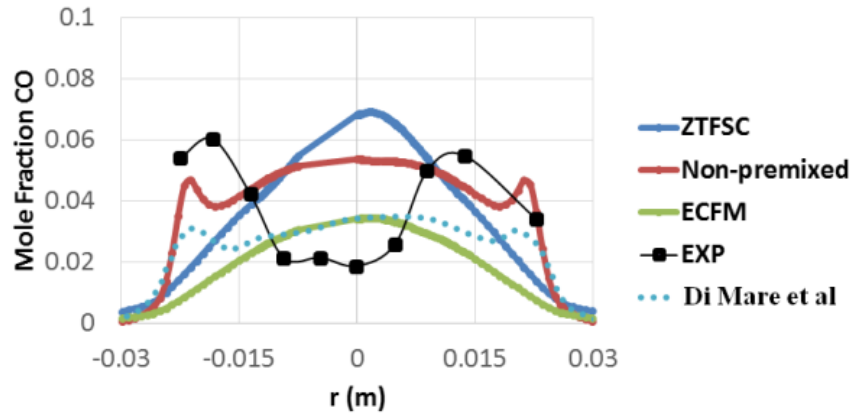
The profiles of various species mole fractions are presented in Figure 5.7. Improvements achieved using the partially premixed models compared to the non-premixed approach can be clearly observed in Figure 5.7c where the mole fraction of propane is in very good agreement with the experimental data. In contrast, when a non-premixed model is employed with both LES and RANS turbulence treatments, large differences between predictions and measurements are observed further revealing the weakness of non-premixed combustion model. The benefits of using a partially premixed assumption can also be observed in Figure 5.7a where a more accurate CO₂ is predicted by the ZTFSC compared to the non-premixed combustion model.

Although the prediction of the oxygen mole fraction is seen to be far from the experimental result, the ZTFSC result is closer to experimental result than the other models. With just a little increase in the consumption of propane, the mole fraction of oxygen would be thought in reasonable agreement with experimental result, i.e. there is an underprediction of combustion near the injection nozzle, as clearly shown in Figure 5.3a.

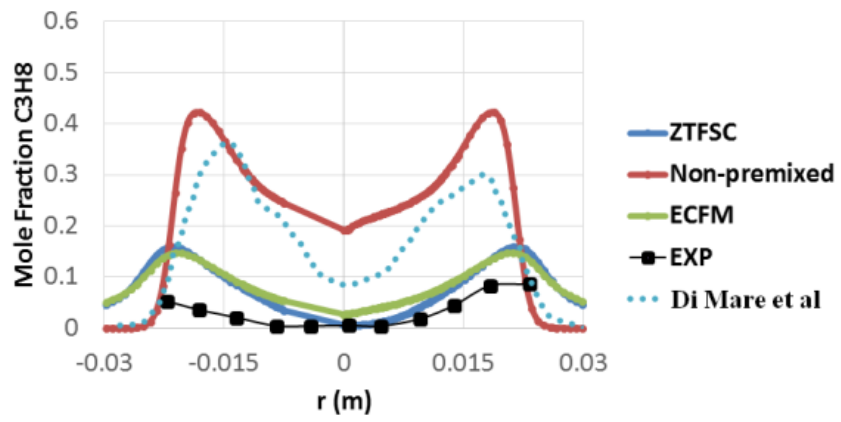


(a)

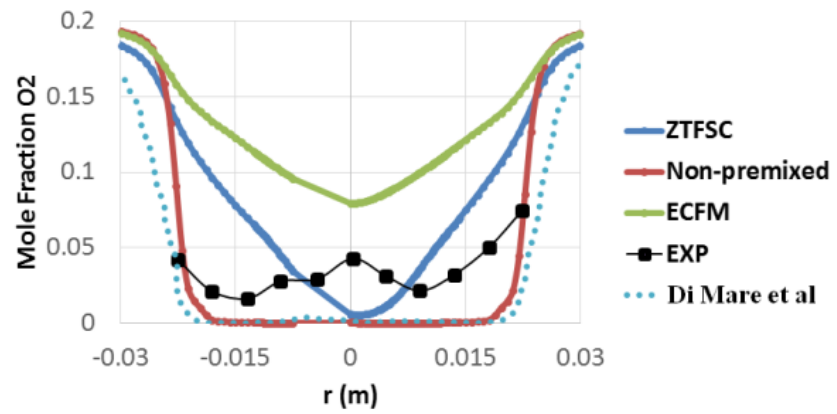
Figure 5.10: Profile of species mole fraction in the horizontal midplane of combustor ($x=20\text{mm}$).



(b)



(c)



(d)

Figure 5.11: (Continued).

Finally, the prediction of carbon monoxide in Figure 5.7b is problematic in that none of the available models properly captures its profile. It was concluded by Di Mare et al [115] that the CO level is not well represented by the steady laminar flamelet method due to its slower reaction rate. Whilst the introduction of a progress variable has allowed for a slower reaction of the other species predictions, it will probably be necessary to take account specifically the slow CO oxidation reaction to predict CO adequately.

5.4 Conclusions

In this chapter, a comparative study of partially premixed and non-premixed combustion models has been presented. The chosen test case geometry retained all features of a commercial aero-engine can-type combustor and provides an excellent test case to illustrate the importance of combustion model selection in complex, 3D, multi-jet swirling flow calculations. The steady RSM model was used to close the turbulent mixing problem. The main findings of the present chapter are:

- A partially premixed combustion model has been applied to a Tay model combustor for the first time and its performance was seen to be quite different to that from a non-premixed combustion model.
- Both LES and RSM treatments of turbulence did not predict flame pattern and species concentrations correctly when applied with a non-premixed combustion model near the injection nozzle.
- The predicted mixture fraction using both ZTFSC and ECFM were similar in the primary region of the combustor, although the latter model predicted much lower temperature due to an underprediction of

reaction progress. Both models predicted the flame shape reasonably accurately in the primary region compared to non-premixed combustion predictions.

- Temperature and species concentrations predicted by the RSM model in conjunction with ZTFSC model were in reasonable agreement with experimental data. Although the temperature profile was underpredicted, the flame pattern was accurately captured.
- Predicted species concentrations of fuel, O₂ and CO₂ were in reasonable agreement with measurement but CO concentration was not well captured by any method. A detailed reaction mechanism taking slow CO oxidation into account is required to improve CO concentration prediction.

Chapter 6

Turbulence Modelling in a Representative Rich Burn Gas

Turbine Combustor

6.1 Introduction

In this chapter, two traditional URANS methods and a scale-resolving simulation (SSTKWSAS) are used to model turbulence and are combined with the partially premixed model of Zimont's 'Turbulent Flame Speed Closure' (ZTFSC) approach to predict turbulent combustion in the same Tay model combustor used in **Chapter 5**.

The main objectives of this chapter are: (i) to fill the gaps in the literature [115, 138], which have used steady RANS and unsteady LES methods but not considered any form of URANS or SAS closures that exist in simulating a fully realistic gas turbine combustor and (ii) to provide guidance in terms of the trade-off between accuracy and CPU Time requirements for 3D combustor flows using scale resolving approaches to turbulence. The SSTKWSAS model has been reported to be able to realise LES-like behaviour but with much larger time steps and using far lower mesh resolution. However, its ability has never been validated in a complex combustion flow that includes multi-jets and strong swirling flow. The numerical results are compared with the experimental results on several planes of the combustor and the benefits of combining the SSTKWSAS (SAS-approach) with the ZTFSC combustion model using the FPVA approach are discussed in the following sections.

6.2 Behaviour of Flow Field and Scalar Variables

The instantaneous iso-surface of swirl strength = 2222.24/s and statistically time-averaged reaction progress contours predicted by different turbulence models are presented in Figure 6.1. The SSTKWSAS model (Figure 6.1c) is seen to provide more large scale swirling eddies emerging in the primary region of the combustor compared to both URANS models due to the fact that traditional URANS models have no mechanism to resolve a significant part of the turbulent spectrum. The detailed structure of the flow close to the swirler is also more complex in the SSTKWSAS prediction. A much thicker central precessing vortex core (PVC) has been captured by SSTKWSAS than that of the URANS predictions. The formation of the PVC is recognised as related to the vortex breakdown phenomenon corresponding to high swirl intensity of the centre recirculation zone (CRZ). The CRZ predicted by SSTKWSAS is thus believed to be stronger and more intensive than that predicted by the traditional URANS models.

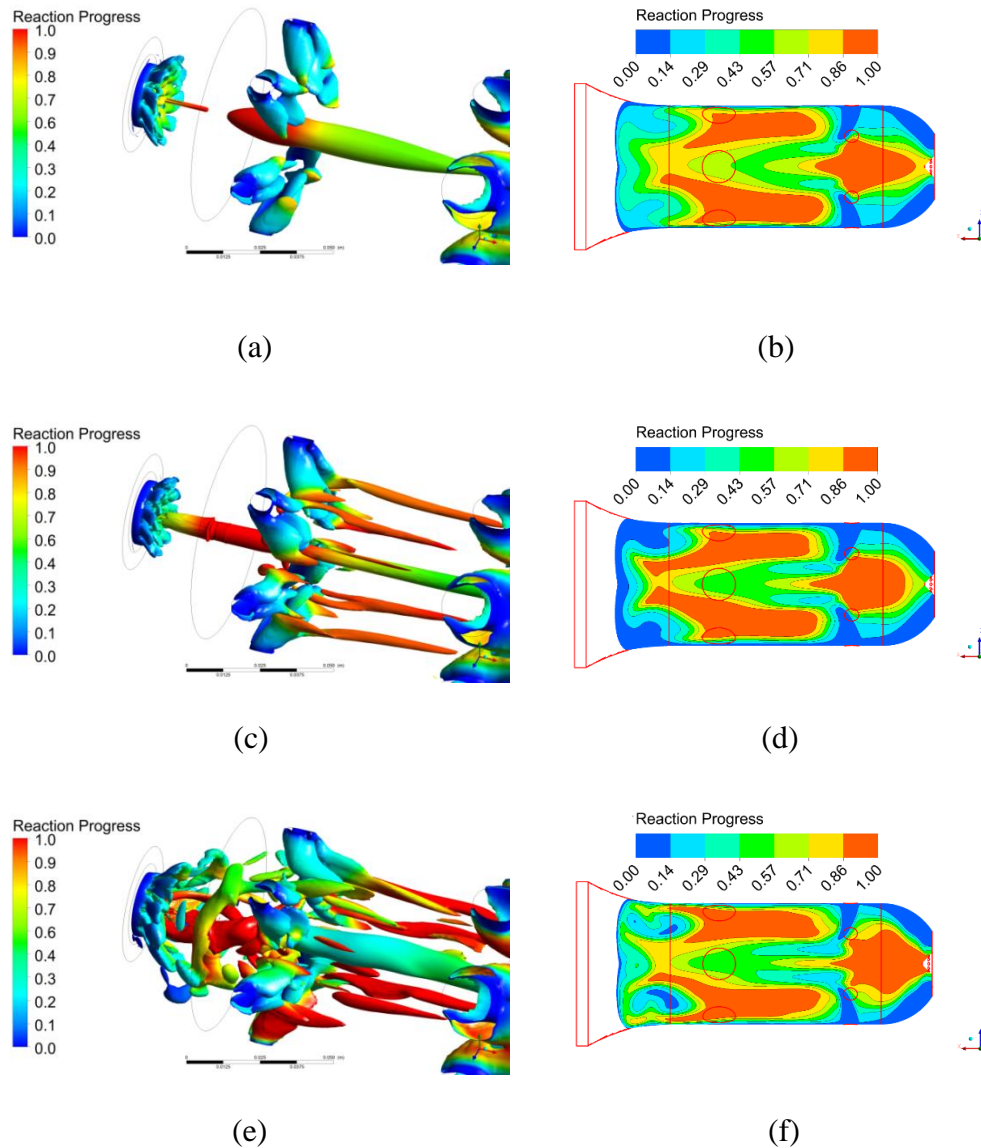
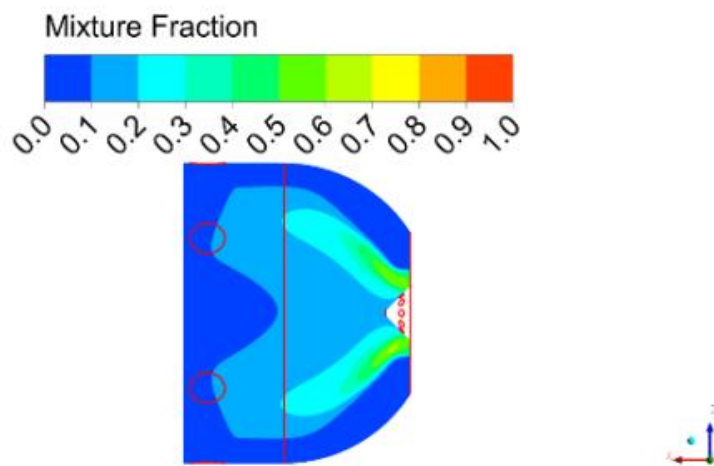


Figure 6.1: Instantaneous iso-surface of swirling strength = 2222.24/s (Left) and statistically averaged reaction progress contours (right). (a) and (b): SSTKW. (c) and (d): RSM. (e) and (f): SSTKWSAS.

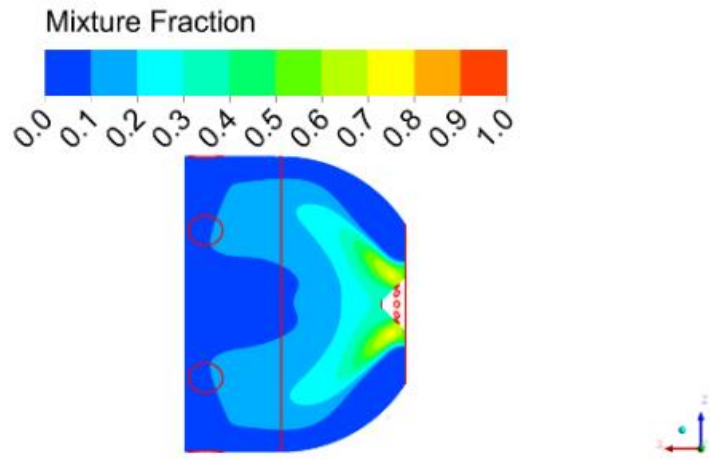
Figure 6.2 shows the distribution of mixture fraction in the primary region of the combustor. The fuel jet clearly penetrates further towards the porous wall in Figure 6.2c (SSTKWSAS) and this is due to higher momentum in the outer layer of the CRZ. In addition, the inner layer of CRZ (negative axial velocity) has recirculated more air from the primary holes towards the head of combustor and thus reduced the mixture fraction. This shows that the CRZ

predicted by the SSTKWSAS model is much stronger than that predicted by other URANS models. The ability to resolve more eddy structures is believed to have increased the mixing rate of fuel and air resulting in faster reaction progress within the local mixtures (as shown in the Figure 6.1b, d and f). The fully combusted region (reaction progress = 1) predicted by SSTKWSAS model is thus wider than that predicted by the URANS models due to the two interrelated reasons: increased CRZ intensity and the ability to resolve eddies. The two mechanisms tend to enhance the flame temperature by more rapid production of a stoichiometric mixture fraction and by enhancing the reaction progress.

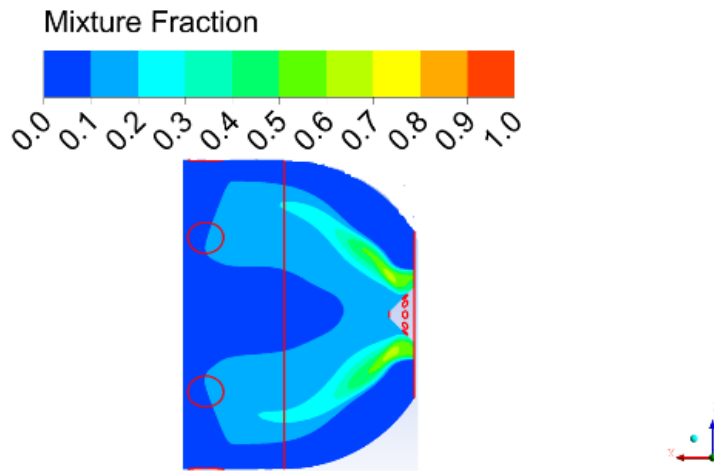


(a)

Figure 6.2: Mean of mixture fraction on horizontal midplane of combustor ($y=0\text{mm}$) (a) SSTKW, (b) RSM, (c) SSTKWSAS.



(b)

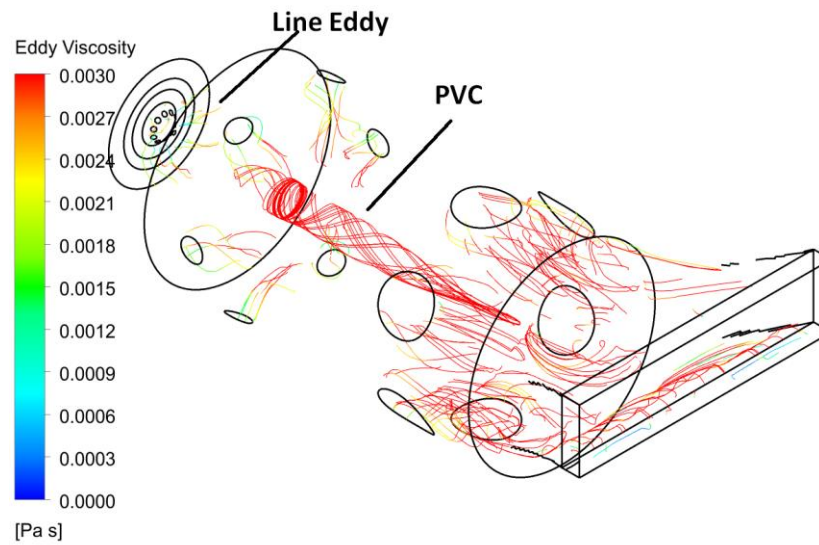


(c)

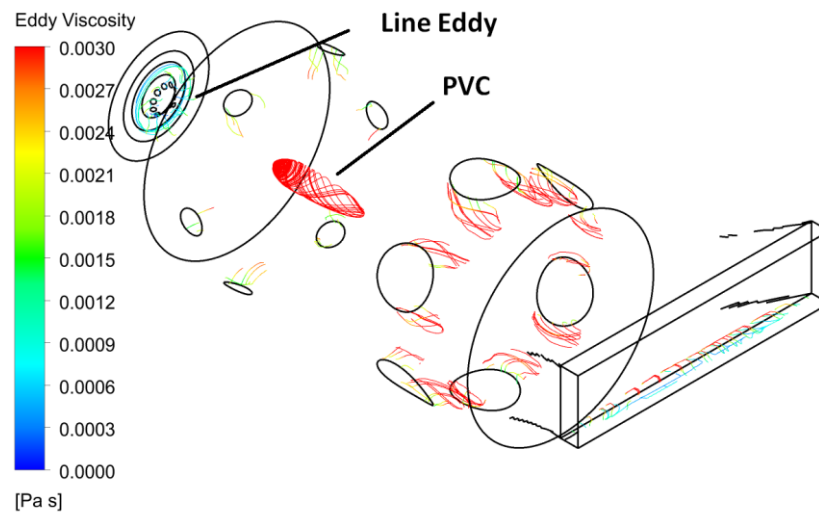
Figure 6.3: (Continued).

A new method (streakline plots applied on surfaces of eddies appeared in Figure 6.1a, c and e) to visualise better the PVC structures captured by different turbulence models is proposed and presented in Figure 6.3. The PVC structures are coloured by eddy viscosity to illustrate the influence of eddy viscosity on the predicted PVC. By comparing the PVCs at two different swirl strength of 2222.24/s and 4444.48/s, the SSTKWSAS model is observed to

produce the lowest eddy viscosity and thus leads to the strongest central PVC. The RSM model produces the less strong PVC and the PVC produced by SSTKW model is lost in primary region. Several line eddies emerging from the swirler have been picked up by the SSTKWSAS model demonstrating its ability to resolve different (and smaller) scales.



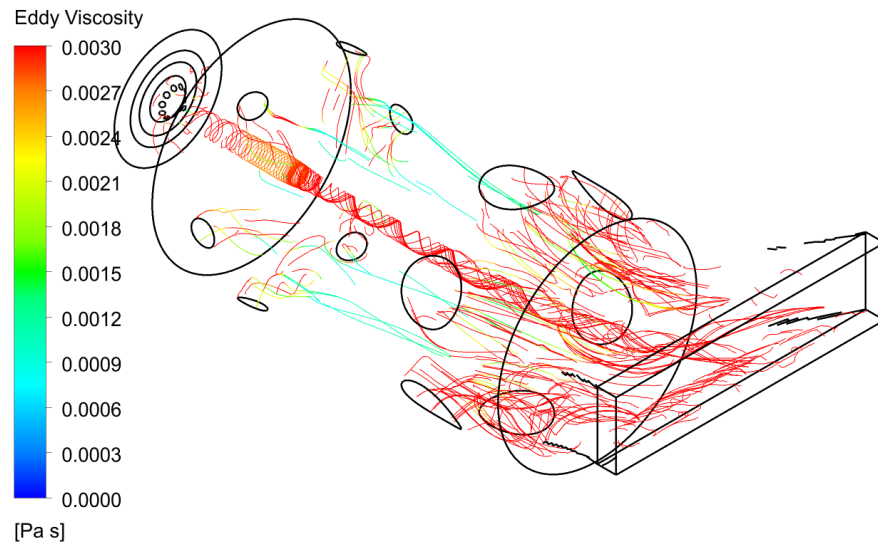
(a) 2222.24/s



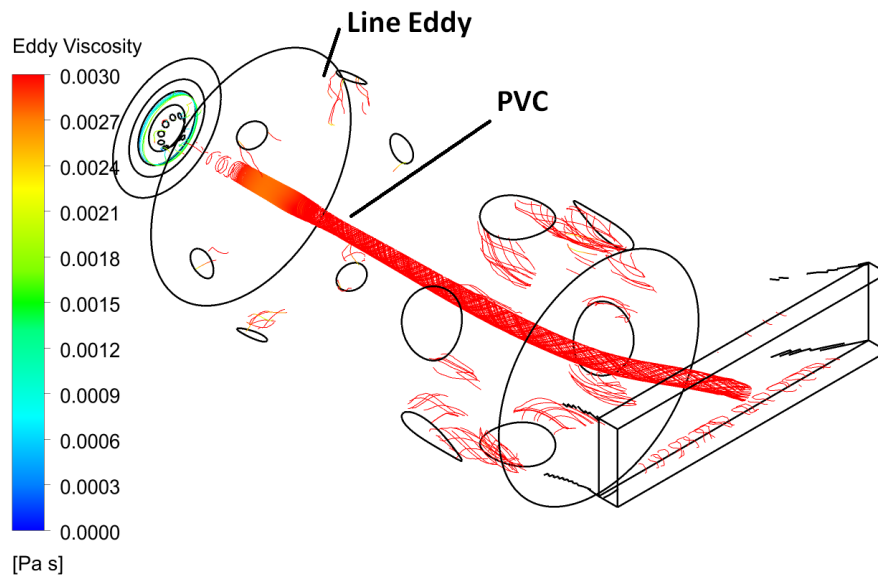
(b) 4444.48/s

Figure 6.4: Instantaneous streakline plots of PVC at 2222.24/s and 4444.48/s.

(a) and (b): SSTKW. (c) and (d): RSM. (e) and (f): SSTKWSAS.

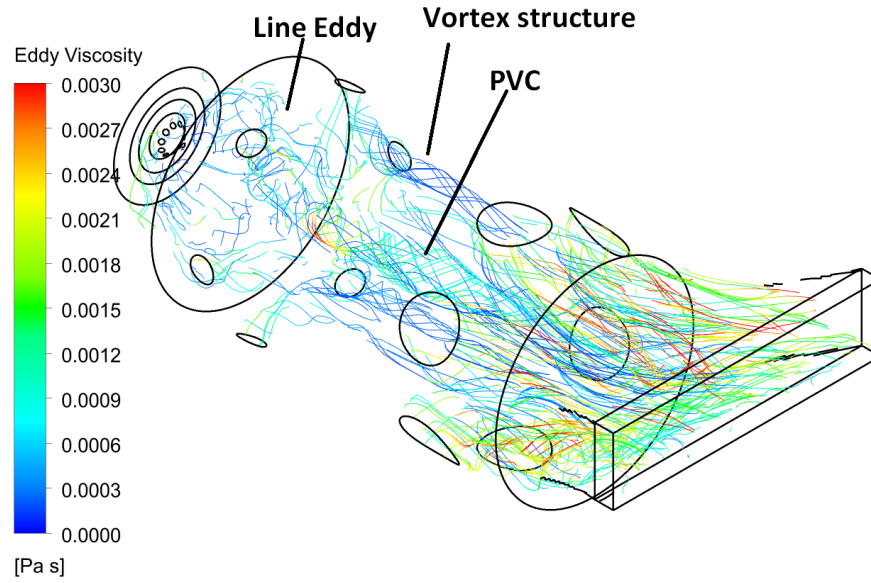


(c) (a) 2222.24/s

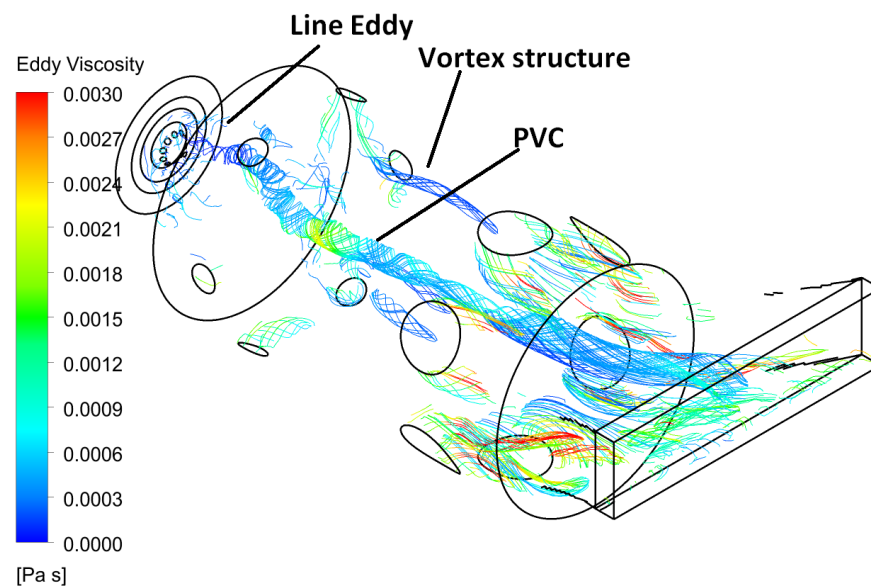


(d) 4444.48/s

Figure 6.5: (Continued).



(e) (a) 2222.24/s



(f) (d) 4444.48/s

Figure 6.6: (Continued).

Meanwhile, complex vortex structure which has not been seen before are clearly captured in Figure 6.3e and f. Six complex vortex structures are formed perhaps due to the reason that fluid flowing out of the primary zone is ‘sucked into’ the wake region behind the radially penetrating primary jets. The SAS

model clearly produces stronger vortex structure compared to those URANS models.

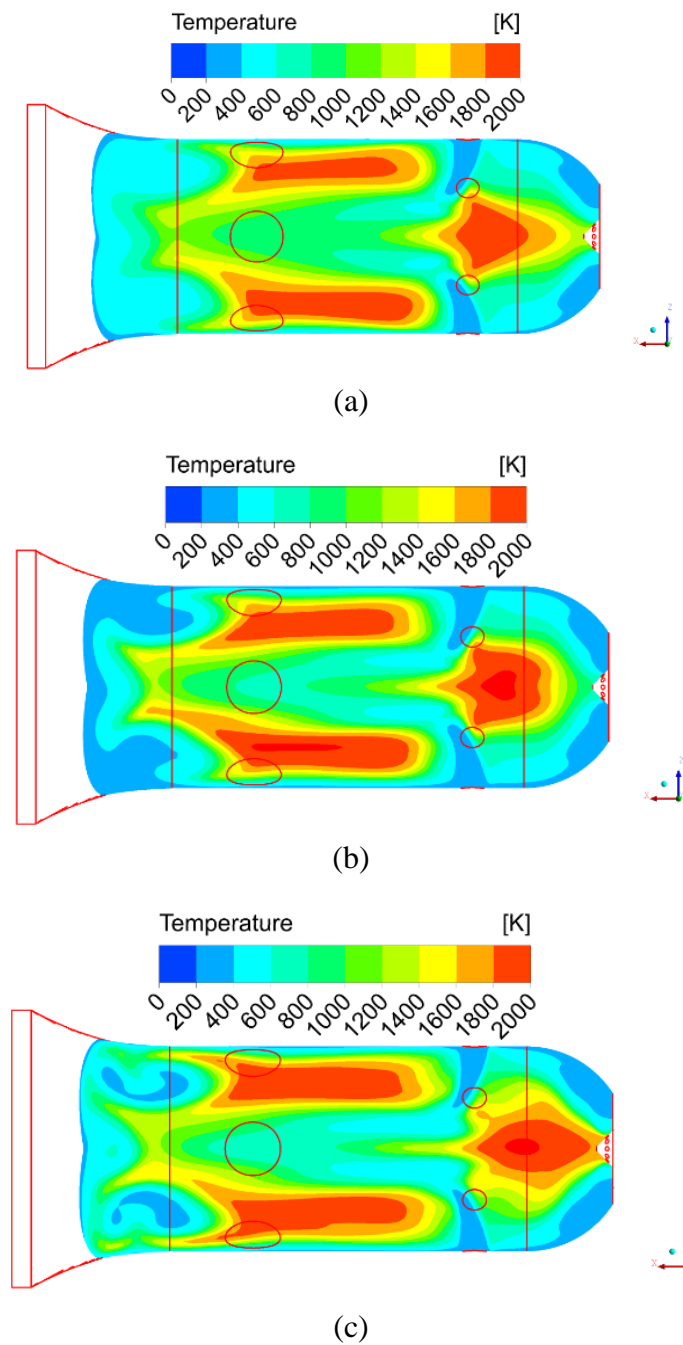
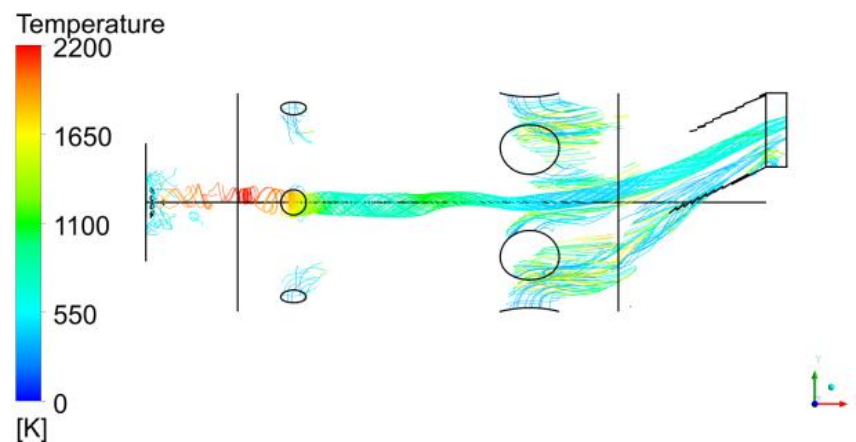


Figure 6.7: Time-mean temperature contours on horizontal midplane of combustor ($y=0\text{mm}$) (a) SSTKW, (b) RSM, (c) SSTKWSAS.

To the author's knowledge, such complex vortex structure has not previously been discussed, since most previous researches have focused only on

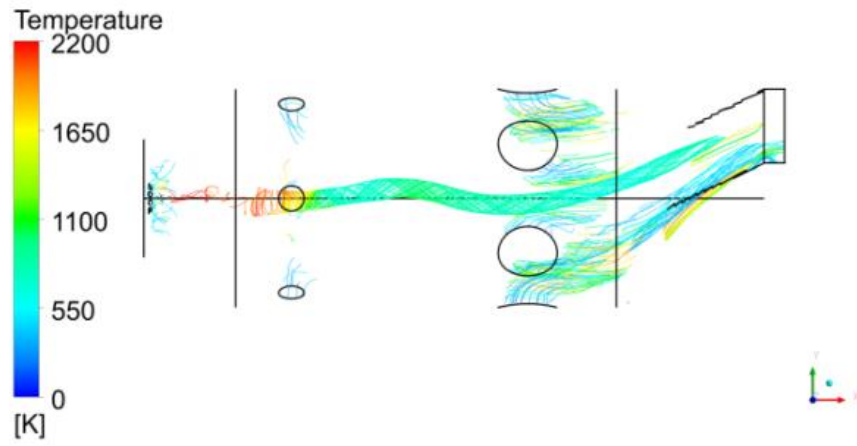
simplified burners with no primary holes. Nevertheless, the positioning of these complex vortex structures might be taken as an indicator of flow features which will certainly influence the wall temperature in the secondary region and needs to be further investigated. These complex vortices are associated with hot primary gas leaving the primary zone through the gaps between primary jets, and then are identified as high temperature zone in the combustor secondary region as shown in Figure 6.4. Note also in this figure, these hot gas regions extended further into the transition nozzle with the SAS closure compared with other URANS models (see **Appendix E** for more comparisons). This finding is thought to be of great interest to turbine designers, although no statistical comparisons with experimental data have been provided due to limited information about the geometry of transition nozzle.

The time-dependent central PVC and its precessing nature about the central axis as predicted by the SSTKWSAS model are illustrated in Figure 6.5. The precessing nature is not captured in the other URANS models as the unsteady nature is essentially much weaker.

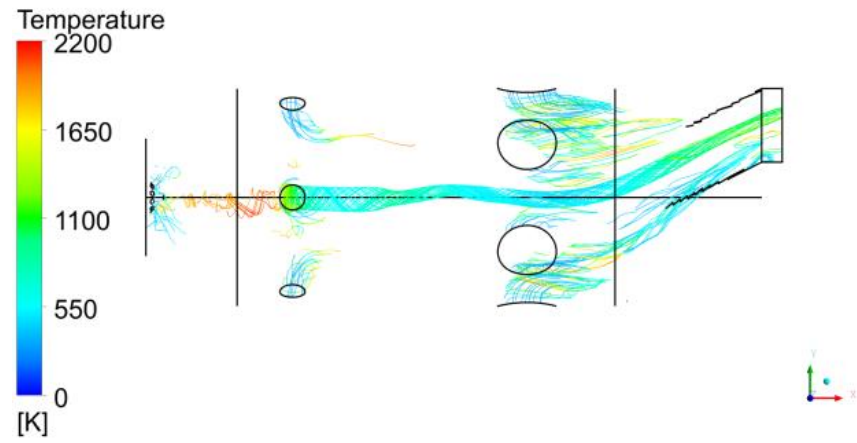


(a) Time step 12000 (Simulation time 1.2s)

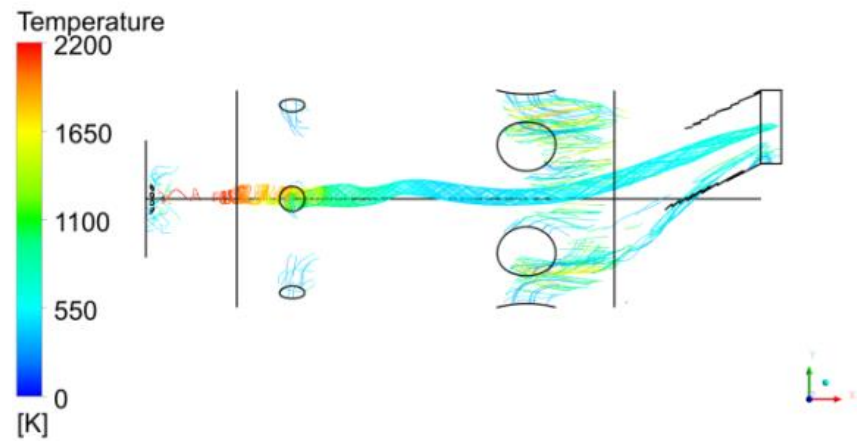
Figure 6.8: Instantaneous streakline plots of PVC at 4444.48/s (SSTKWSAS).



(b) Time step 13000 (Simulation time 1.3s)



(c) Time step 14000 (Simulation time 1.4s)

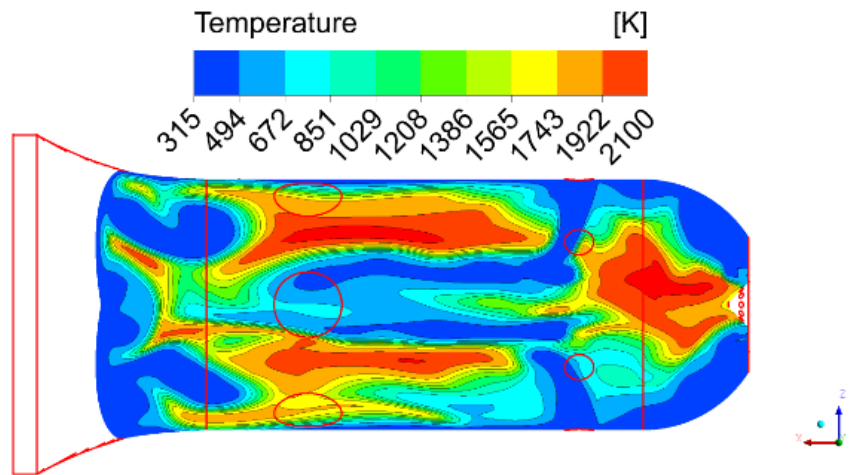


(d) Time step 15000 (Simulation time 1.5s)

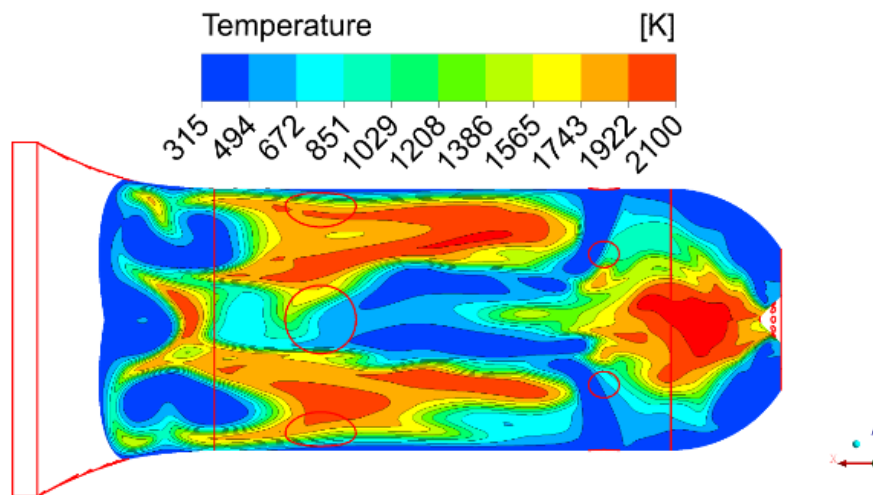
Figure 6.9: (Continued).

Furthermore, since the reaction progress variable determines the status of local mixtures, the flame shapes predicted by different turbulence models are obviously well illustrated by the pattern of reaction progress. The wider primary zone shape predicted by the SSTKWSAS model (see Figure 6.4c) is in reasonable agreement with the experimental results (see following section) and the results support the conclusion made by Zhang et al [138] that a scale adaptive simulation such as SAS is better able to represent flame pattern.

Finally, to show the transient behaviour predicted using the SAS approach, the instantaneous temperature field on the combustor horizontal midplane is provided in Figure 6.6. The predicted flame has clearly stabilised in the recirculation region and in the wake behind the primary jets. No reaction happens close to the combustor liner walls which are prevented by the cool air passing through the porous walls. Cold air flow from the diameter reduced primary holes has penetrated right to the combustor centreline and has greatly reduced the flame temperature in the central of the secondary region of combustor. Note that flame fluctuations show significant variation in the shape the varied hot gas region at different times.

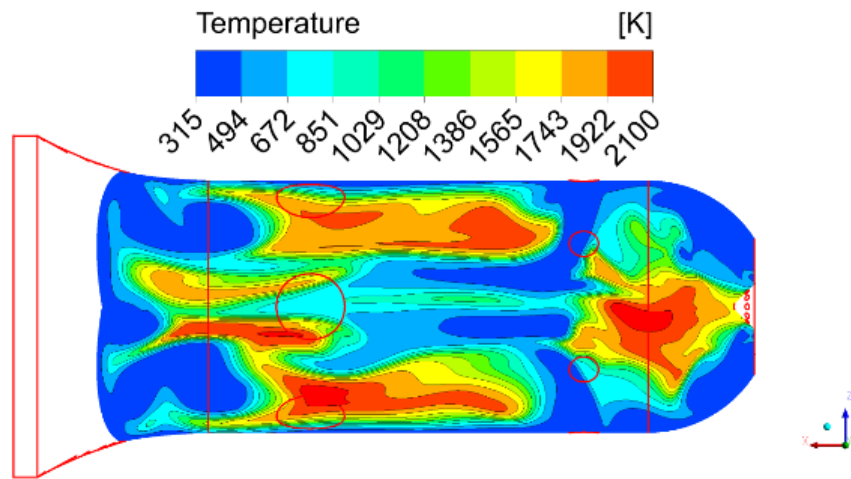


(a) Time step 10020 (Simulation time 1.002s)

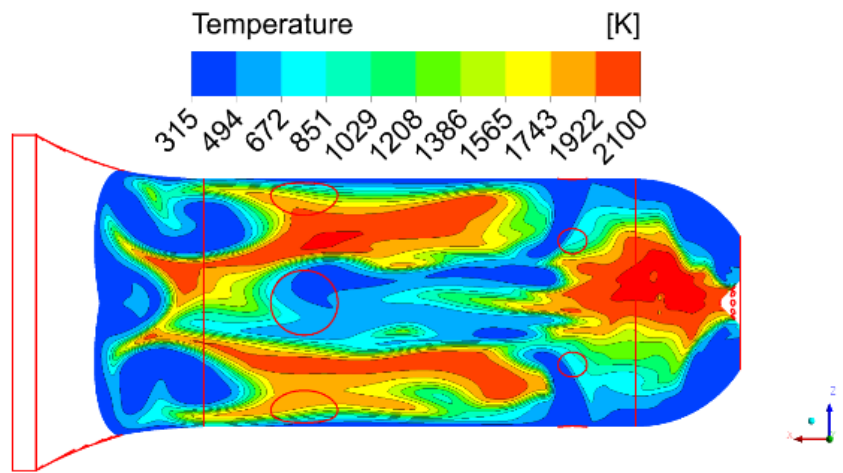


(b) Time step 11000 (Simulation time 1.100s)

Figure 6.10: Instantaneous temperature field at horizontal midplane (SSTKWSAS).



(c) Time step 11880 (Simulation time 1.188s)



(d) Time step 12980 (Simulation time 1.298s)

Figure 6.11: (Continued).

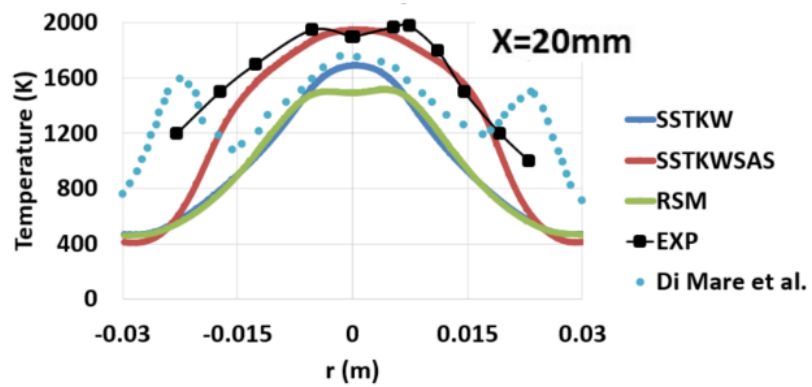
6.3 Statistical Results

In this section, the statistical results achieved in the various computations are discussed and compared with measurements [114], as well as the LES predictions of Di Mare et al [115].

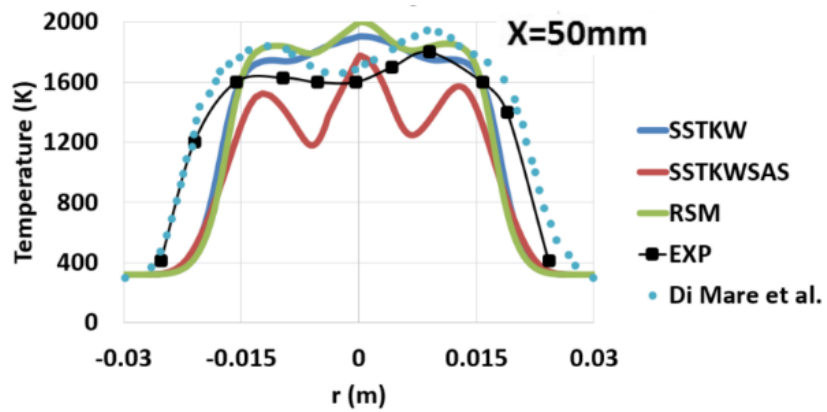
Good agreement between prediction and experiment can be observed in Figure 6.7a particularly for the SSTKWSAS simulation, which is closer to the experimental data than all the other predictions and show a temperature profile higher than other models. Modifying the primary hole diameter has clearly improved the accuracy of predictions at $x=20\text{mm}$. It is also likely, however, that it has led to a deterioration in the agreement where predictions are performed further downstream at $x=50\text{mm}$ (Figure 6.7b). This speculation is partially confirmed by observing the prediction by Di Mare et al [115] who retained the original size of the primary holes. Their prediction of flame pattern at $x=50\text{mm}$ is in reasonable agreement with the experimental result even though the non-premixed combustion model was employed which is inappropriate for such combustor.

Figure 6.7c shows comparison of the mean mixture fraction predicted in this study with the LES prediction of Di Mare et al [115]. Discrepancies occur mainly at the peaks of curves where the SAS model shows a slight higher mixture fraction and much wider peaks than LES. However, since the SAS approach used here predict the temperature closer to the experimental data than LES, the SAS approach seems to predict CRZ very well and more accurate. The outer layer (positive axial velocity) of the wider and more intensive CRZ predicted by the SAS model has transported more fuel towards

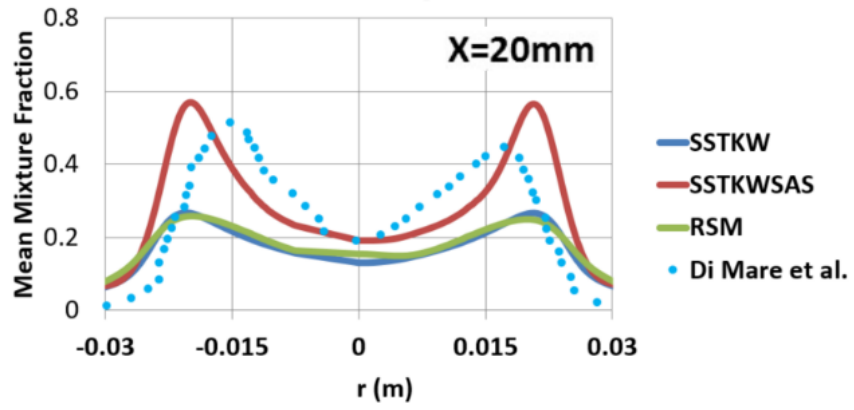
the porous wall and presented extended fuel jets (as shown in Figure 6.2c) (which is why the peaks predicted by the SAS model are higher). Note also that the two URANS models predict lower mixture fraction compared to LES and URANS and which are incorrect.



(a)

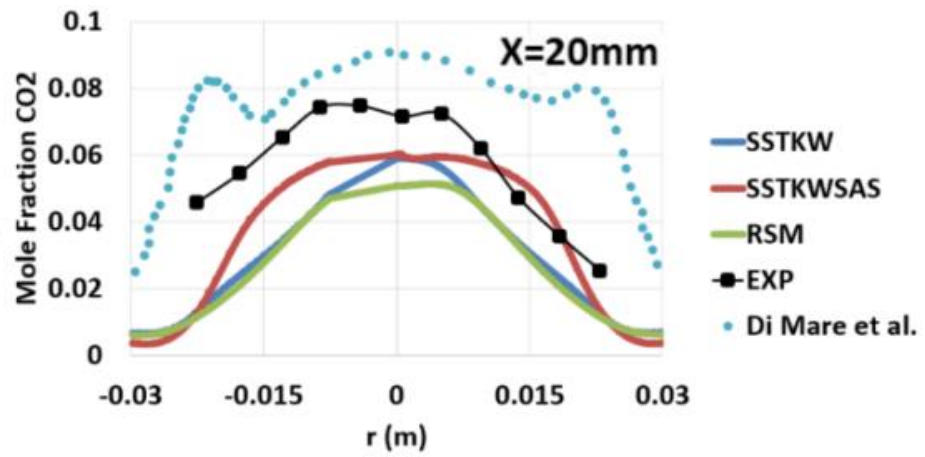


(b)

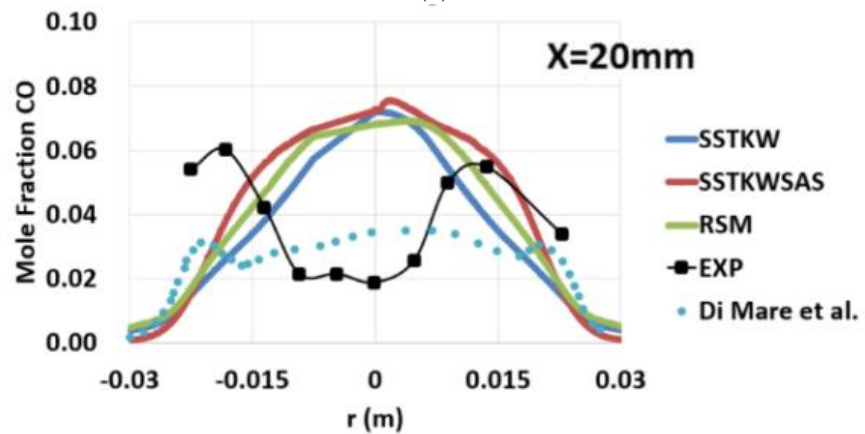


(c)

Figure 6.12: Profile of temperature and mixture fraction in the horizontal midplane of the combustor ($y=0\text{mm}$).

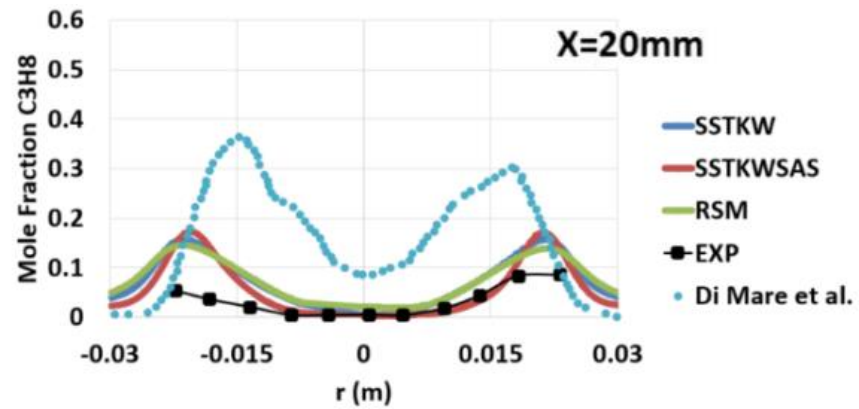


(a)

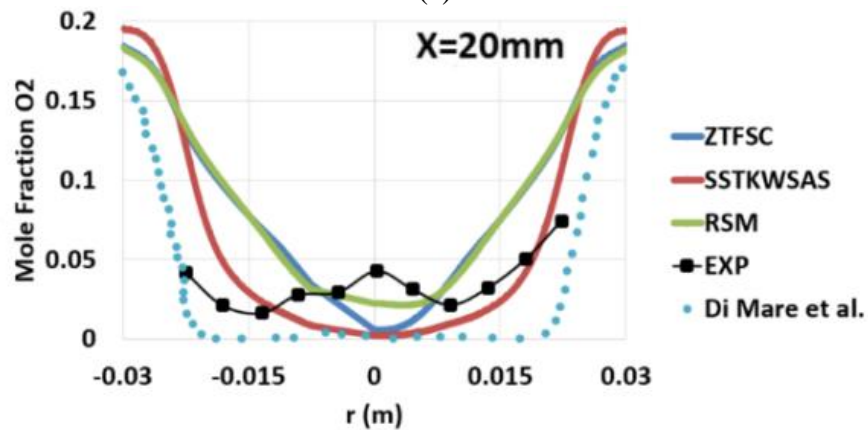


(b)

Figure 6.13: Profile of species mole fraction in the horizontal midplane of combustor.



(c)



(d)

Figure 6.14: (Continued).

Finally, as can be seen in Figure 6.8, the majority of species mole fractions predicted by SSTKWSAS has outperformed the URANS or even the LES predictions of Di Mare et al [115], although as expected all models fail to predict the CO mole fraction accurately. This is again because the chemistry closure adopted is not applicable to the slow CO oxidation reaction. The more accurate prediction of the CO₂ level illustrates that the partially premixed model in conjunction with the SAS approach has significant advantage over the traditional URANS models.

It is worth emphasis again that for the SAS approach, the time step size of 1e-04s is far less than the 2e-07s reported by Di Mare et al using LES [115]

which is limited by $CFL \approx 1$, hence the current prediction requires far less computational time compared to LES.

6.4 Conclusions

Comparative studies of two conventional URANS models (SSTKW and RSM) and a scale-resolving simulation represented by the SSTKWSAS model have been presented. The chosen test case geometry possesses all features of commercial aero-engine rich burn can-type combustors and provides an excellent test case to examine the advantages of using SAS approach in conjugated with a partially premixed combustion model. Tabulated chemistry were chosen to reduce the cost of using a detailed chemical kinetic scheme. The local chemical non-equilibrium caused by turbulent strain is taken into account by introducing the scalar dissipation rate in tabulation of the flamelet library and a presumed shape PDF was used for turbulent combustion interaction. The main findings of this chapter were:

- For the first time, a scale resolving simulation method (SAS approach) was employed to predict turbulent combustion in Tay model gas turbine combustor by invoking the partially premixed ZTFSC combustion model.
- The SSTKWSAS model was seen to provide much better temperature and species concentration agreement with experimental data in the complex primary zone compared to URANS method due to its ability (at least partially) to resolve the turbulent spectrum.
- The mixture fraction distribution in the primary region of the combustor predicted in the current study was close to that predicted by

LES as reported in the literature. This indicates that the SSTKWSAS model is able to produce LES-like behaviour without explicit dependence on local grid spacing and of much smaller computational cost.

Finally, the study emphasises the advantages of using a more efficient and numerical accurate scale-resolving simulation of SSTKWSAS model in simulating complex, swirl-stabilised, multi-jet partially premixed turbulent flame. The computations using the SSTKWSAS model were carried out on the City, University of London 20 processor Solon cluster. A total wall-clock time of 160h was spent for a prediction from scratch (2 million mesh). Past predictions based on LES of the same combustor have required total wall clock time of 26,432 hours using 64 processing elements of the Cray T3E at the University of Manchester is unaffordable by most industries (1 million mesh) though the prediction was done in 2004 [115].

Chapter 7

Closure: Conclusions and Recommendations

7.1 Summary

The work presented in this thesis has demonstrated a practical turbulence combustion modelling method for simulation of an industrially representative rich-burn Tay model gas turbine combustor containing a complex geometry of multi-jet, and highly swirling flow. The method is based on the coupling of a partially premixed combustion model (ZTFSC) within a mixture fraction/reaction progress variable thermo-chemical discipline and an SRS turbulence model (SSTKWSAS) closure. Chemical reactions are not assumed to proceed at infinitely fast rate and the progress of the chemical reaction is controlled by the solution of the transport equation for the reaction progress variable. The more conventional widely used mixture fraction/flamelet method lacks any mechanism to take into account slow chemical reaction effects such as local extinction and re-ignition.

It has been shown that the coupling of these two approaches to turbulence and combustion chemistry can be used to predict complex turbulent combustion problems more efficiently and accurately than an approach based on non-premixed combustion models and the LES method as often reported in the literature.

7.2 Overall Conclusions

The following conclusions are drawn from the work presented in this thesis.

1. The benefits of coupling the ZTFSC combustion model and SSTKWSAS turbulence model in predicting turbulent combustion in a complex industrial gas turbine combustor accurately and efficiently have been demonstrated.
2. The SSTKWSAS model was seen to present LES-like behaviour without explicit dependence on local grid spacing even with a relatively large time step size, whilst presenting stable numerical solutions.
3. The time spent for the simulation in the current thesis using the SSTKWSAS model is approximately 1/165 of the time needed by the LES model reported in the literature (though the LES prediction was done in 2004).
4. Cross-comparison with experimental and computational results available in the literature has been performed and reasons for previous inaccurate predictions in the primary region of the combustor has been analysed. An accurate flame pattern in this region has been captured in this thesis.
5. The ZTFSC model has been shown to perform significantly better than the ECFM model that the latter one has over-suppressed the chemical reaction rate.
6. The importance of using a partially premixed combustion model in simulating combustion in the primary zone of the complex flow environment involved in 3D high swirl combustor has been highlighted.

7.3 Recommendations for Future Work

Several recommendations for future work are presented here based on the results of this thesis.

1. The current work has employed the specified fixed mass flow rate distribution through the porous wall of the combustor due to lack of newly developed information on the porous material and the difficulty of modelling flow through porous walls. However, this simplification may influence the flame shape and temperature especially in the primary region of combustor. It would be useful to develop a new physically based methodology for calculating the cross flow distribution through a porous wall as a function, for example, as the function of pressure difference across the wall.
2. The SAS approach can only resolve the turbulent spectrum down to the resolution of the mesh. It is possible that the amount of turbulence spectrum resolved by the SSTKWSAS model with the current mesh is not enough. The combustion models might respond differently if more of the spectrum were resolved. Also, the ECFM model might be much more sensitive to turbulence compared to the ZTFSC model whose chemical reactions is dominated by the turbulent flame speed which is proportional to the local mixture fraction, while, the flame surface area used to estimate the chemical reaction rate in ECFM is more sensitive to turbulence. It would be of interest to repeat the current study with a linear mesh to examine this feature.
3. Near the combustor wall, complex vortex structures were observed penetrating into secondary region which will influence the wall temperature

significantly since wall cooling is of great importance in combustor design, further investigations of their flow features should be carried out.

4. Whilst the introduction of a reaction progress variable in the FPVA method allows the overall chemical reaction rate to proceed at a finite rate, it is insufficiently designed to limit the chemistry of very slow reactions. This is necessary because prediction of CO concentration in the primary zone was not well captured. By imposing one more transport equation similar as the progress variable transport equation but with a local CO reaction rate control limit, the overall temperature and emission levels in the combustor can be better studied.

REFERENCE LIST

- [1] Koff, B.L. and Koff, B.L., 2004. Gas turbine technology evolution: A designer's perspective. *Journal of propulsion and power*, 20(4), pp.577-595.
- [2] En.wikipedia.org. (2016). Power Jets W.1. [online] Available at: https://en.wikipedia.org/wiki/Power_Jets_W.1 [Accessed 4 Nov. 2016].
- [3] Hada, S.A.T.O.S.H.I., Tsukagoshi, K.E.I.Z.O., Masada, J.U.N.I.C.H.I.R.O. and Ito, E.I.S.A.K.U., 2012. Test results of the world's first 1,600 C J-series gas turbine. *Mitsubishi Heavy Industries Technical Review*, 49(1), p.18.
- [4] En.wikipedia.org. (2016). Rolls-Royce Trent 900. [online] Available at: https://en.wikipedia.org/wiki/Rolls-Royce_Trent_900 [Accessed 4 Nov. 2016].
- [5] En.wikipedia.org. (2016). Turbojet. [online] Available at: https://en.wikipedia.org/wiki/Turbojet#/media/File:Jet_engine.svg [Accessed 4 Nov. 2016].
- [6] Leeham News and Comment. (2016). PW Canada continues next-gen turboprop development despite airplane demand uncertainty - Leeham News and Comment. [online] Available at: <https://leehamnews.com/2016/03/24/pw-canada-continues-next-gen-turboprop-development-despite-airplane-demand-uncertainty/> [Accessed 4 Nov. 2016].
- [7] Gandoza. F100 Turbofan Engine Cutaway. [online] Available at: <http://www.power-eng.com/articles/print/volume-118/issue-5/features/fuels-combustion-environmental-considerations-in-industrial-gas-turbines.html> [Accessed 4 Nov. 2016].

- [8] Encyclopedia Britannica. (2016). afterburner | mechanical engineering. [online] Available at: <https://www.britannica.com/technology/afterburner-mechanical-engineering> [Accessed 4 Nov. 2016].
- [9] Igoe, B. and Welch, M. 2003. Fuels, Combustion & Environmental Considerations in Industrial Gas Turbines. [online] Power Engineering. Available at: <http://www.power-eng.com/articles/print/volume-118/issue-5/features/fuels-combustion-environmental-considerations-in-industrial-gas-turbines.html> [Accessed 4 Nov. 2016].
- [10] YouTube. (2016). Annular Combustion Chamber. [online] Available at: <https://www.youtube.com/watch?v=ZVojTaeSB1E> [Accessed 4 Nov. 2016].
- [11] Symscape.com. (2016). Open Wheel Race Car CFD Analysis | Symscape. [online] Available at: <http://www.symscape.com/examples/rans/open-wheel-racecar-cfd> [Accessed 4 Nov. 2016].
- [12] Lockwood, F.C. and Naguib, A.S., 1975. The prediction of the fluctuations in the properties of free, round-jet, turbulent, diffusion flames. *Combustion and Flame*, 24, pp.109-124.
- [13] Kent, J.H. and Bilger, R.W., 1977, December. The prediction of turbulent diffusion flame fields and nitric oxide formation. In *Symposium (International) on Combustion* (Vol. 16, No. 1, pp. 1643-1656). Elsevier.
- [14] Bilger, R.W., 1976. Turbulent jet diffusion flames. *Energy Combust. Sci*, 1, pp.87-109.
- [15] Bray, K.N.C. and Peters, N., 1994. Laminar flamelets in turbulent flames. *Turbulent reacting flows*, pp.63-113.

- [16] Peters, N., 1984. Laminar diffusion flamelet models in non-premixed turbulent combustion. *Progress in energy and combustion science*, 10(3), pp.319-339.
- [17] Peters, N., 1988, December. Laminar flamelet concepts in turbulent combustion. In *Symposium (International) on Combustion (Vol. 21, No. 1, pp. 1231-1250)*. Elsevier.
- [18] Bilger, R.W., 1991. Conditional moment methods for turbulent reacting flow using Crocco variable conditions. Charles Kolling Report, Department of Mechanical Engineering, the University of Sydney, TN F-99.
- [19] Bilger, R.W., 1993. Conditional moment closure for turbulent reacting flow. *Physics of Fluids A: Fluid Dynamics (1989-1993)*, 5(2), pp.436-444.
- [20] Pope, S.B., 1985. PDF methods for turbulent reactive flows. *Progress in Energy and Combustion Science*, 11(2), pp.119-192.
- [21] Pope, S.B., 1991, December. Computations of turbulent combustion: progress and challenges. In *Symposium (International) on Combustion (Vol. 23, No. 1, pp. 591-612)*. Elsevier.
- [22] Villermaux, J. and Devillon, J.C., 1972, May. Représentation de la coalescence et de la redispersion des domaines de ségrégation dans un fluide par un modèle d'interaction phénoménologique. In *Second International Symposium on Chemical Reaction Engineering*, Elsevier, New York (pp. 1-13).
- [23] Dopazo, C. and O'Brien, E.E., 1974. An approach to the autoignition of a turbulent mixture. *Acta Astronautica*, 1(9), pp.1239-1266.

- [24] Janicka, J., Kolbe, W. and Kollmann, W., 1979. Closure of the transport equation for the probability density function of turbulent scalar fields. *Journal of Non-Equilibrium Thermodynamics*, 4(1), pp.47-66.
- [25] Subramaniam, S. and Pope, S.B., 1998. A mixing model for turbulent reactive flows based on Euclidean minimum spanning trees. *Combustion and Flame*, 115(4), pp.487-514.
- [26] Lindstedt, R.P., Louloudi, S.A. and Vaos, E.M., 2000. Joint PDF modeling of pollutant formation in piloted turbulent jet diffusion flames with comprehensive chemistry. In 28th Symposium (International) on Combustion (pp. 149-156).
- [27] Smith, N.S.A., Bilger, R.W., Carter, C.D., Barlow, R.S. and Chen, J.Y., 1995. A comparison of CMC and PDF modelling predictions with experimental nitric oxide LIF/Raman measurements in a turbulent H₂ jet flame. *Combustion science and technology*, 105(4-6), pp.357-375.
- [28] Barlow, R.S., Smith, N.S.A., Chen, J.Y. and Bilger, R.W., 1999. Nitric oxide formation in dilute hydrogen jet flames: isolation of the effects of radiation and turbulence-chemistry submodels. *Combustion and Flame*, 117(1), pp.4-31.
- [29] Hinz, A., Hassel, E.P. and Janicka, J., 1999. Numerical simulation of turbulent non-equilibrium methane-air jet flames using Monte Carlo PDF method. In TSFP DIGITAL LIBRARY ONLINE. Begel House Inc..

- [30] Anand, M.S., Hsu, A.T. and Pope, S.B., 1997. Calculations of swirl combustors using joint velocity-scalar probability density function method. *AIAA journal*, 35(7), pp.1143-1150.
- [31] Hinz, A., Hassel, E.P. and Janicka, J., 1999. Numerical simulation of turbulent non-equilibrium methane-air jet flames using Monte Carlo PDF method. In *TSFP DIGITAL LIBRARY ONLINE*. Begel House Inc..
- [32] Carrier, G.F., Fendell, F.E. and Marble, F.E., 1975. The effect of strain rate on diffusion flames. *SIAM Journal on Applied Mathematics*, 28(2), pp.463-500.
- [33] Williams, F.A., 1985. Turbulent combustion. *The mathematics of combustion*, 2, pp.267-294.
- [34] Liew, S.K., Bray, K.N.C. and Moss, J.B., 1984. A stretched laminar flamelet model of turbulent nonpremixed combustion. *Combustion and Flame*, 56(2), pp.199-213.
- [35] Rogg, B., Behrendt, F. and Warnatz, J., 1988, January. Turbulent non-premixed combustion in partially premixed diffusion flamelets with detailed chemistry. In *Symposium (International) on Combustion (Vol. 21, No. 1, pp. 1533-1541)*. Elsevier.
- [36] Haworth, D.C., Drake, M.C. and Blint, R.J., 1988. Stretched laminar flamelet modeling of a turbulent jet diffusion flame. *Combustion science and technology*, 60(4-6), pp.287-318.
- [37] Correa, S.M., Drake, M.C., Pitz, R.W. and Shyy, W., 1985, January. Prediction and measurement of a non-equilibrium turbulent diffusion flame. In

Symposium (International) on Combustion (Vol. 20, No. 1, pp. 337-343). Elsevier.

[38] Haworth, D.C., Drake, M.C., Pope, S.B. and Blint, R.J., 1989, December. The importance of time-dependent flame structures in stretched laminar flamelet models for turbulent jet diffusion flames. In Symposium (International) on Combustion (Vol. 22, No. 1, pp. 589-597). Elsevier.

[39] Barlow, R.S. and Carter, C.D., 1994. Raman/Rayleigh/LIF measurements of nitric oxide formation in turbulent hydrogen jet flames. *Combustion and Flame*, 97(3-4), pp.261-280.

[40] Pitsch, H., Chen, M. and Peters, N., 1998, December. Unsteady flamelet modeling of turbulent hydrogen-air diffusion flames. In Symposium (international) on combustion (Vol. 27, No. 1, pp. 1057-1064). Elsevier.

[41] Pitsch, H., 2000. Unsteady flamelet modeling of differential diffusion in turbulent jet diffusion flames. *Combustion and Flame*, 123(3), pp.358-374.

[42] Pitsch, H., Riesmeier, E. and Peters, N., 2000. Unsteady flamelet modeling of soot formation in turbulent diffusion flames. *Combustion science and technology*, 158(1), pp.389-406.

[43] Pitsch, H. and Steiner, H., 2000. Large-eddy simulation of a turbulent piloted methane/air diffusion flame (Sandia flame D). *Physics of Fluids* (1994-present), 12(10), pp.2541-2554.

[44] Barlow, R.S. and Frank, J.H., 1998, December. Effects of turbulence on species mass fractions in methane/air jet flames. In Symposium (International) on Combustion (Vol. 27, No. 1, pp. 1087-1095). Elsevier.

- [45] Kalt, P.A., Al-Abdell, Y.M., Masri, A.R. and Barlow, R.S., 2002. Swirling turbulent non-premixed flames of methane: flow field and compositional structure. *Proceedings of the Combustion Institute*, 29(2), pp.1913-1919.
- [46] Sripakagorn, P., Mitarai, S., Kos̄ly, G. and Pitsch, H., 2004. Extinction and reignition in a diffusion flame: a direct numerical simulation study. *Journal of Fluid Mechanics*, 518, pp.231-259.
- [47] Sripakagorn, P., Kos̄ly, G. and Pitsch, H., 2001. Reignition scenarios in a simulated diffusion flame. In 2nd Joint Meeting of the US Sections of the Combustion Institute. Oakland, California: The Combustion Institute.
- [48] Sripakagorn, P., 2002. Local extinction and reignition in turbulent nonpremixed combustion.
- [49] Sripakagorn, P., Kos̄ly, G. and Pitsch, H., 2000. Local extinction-reignition in turbulent nonpremixed combustion. *Annual Research Briefs*, pp.117-128.
- [50] Hewson, J.C. and Kerstein, A.R., 2002. Local extinction and reignition in nonpremixed turbulent CO/H₂/N₂ jet flames. *Combustion science and technology*, 174(5-6), pp.35-66.
- [51] Xu, J. and Pope, S.B., 2000. PDF calculations of turbulent nonpremixed flames with local extinction. *Combustion and Flame*, 123(3), pp.281-307.
- [52] Tang, Q., Xu, J. and Pope, S.B., 2000. Probability density function calculations of local extinction and NO production in piloted-jet turbulent

methane/air flames. Proceedings of the Combustion Institute, 28(1), pp.133-139.

[53] Kempf, A.M., Schneider, C., Sadiki, A. and Janicka, J., 2001. Large eddy simulation of a highly turbulent methane flame: application to the DLR standard flame. In TSFP DIGITAL LIBRARY ONLINE. Begel House Inc..

[54] Sreedhara, S. and Huh, K.Y., 2005. Modeling of turbulent, two-dimensional nonpremixed CH₄/H₂ flame over a bluff body using first-and second-order elliptic conditional moment closures. Combustion and flame, 143(1), pp.119-134.

[55] Masri, A.R., Kalt, P.A. and Barlow, R.S., 2004. The compositional structure of swirl-stabilised turbulent nonpremixed flames. Combustion and Flame, 137(1), pp.1-37.

[56] Barlow, R.S., Dibble, R.W., Chen, J.Y. and Lucht, R.P., 1990. Effect of Damköhler number on superequilibrium OH concentration in turbulent nonpremixed jet flames. Combustion and Flame, 82(3), pp.235-251.

[57] Barlow, R.S. and Carter, C.D., 1994. Raman/Rayleigh/LIF measurements of nitric oxide formation in turbulent hydrogen jet flames. Combustion and Flame, 97(3-4), pp.261-280.

[58] Barlow, R.S. and Carter, C.D., 1996. Relationships among nitric oxide, temperature, and mixture fraction in hydrogen jet flames. Combustion and Flame, 104(3), pp.288-299.

- [59] Dally, B.B., Masri, A.R., Barlow, R.S. and Fiechtner, G.J., 1998. Instantaneous and mean compositional structure of bluff-body stabilized nonpremixed flames. *Combustion and Flame*, 114(1), pp.119-148.
- [61] Dally, B.B., Masri, A.R., Barlow, R.S. and Fiechtner, G.J., 2003. Two-photon laser-induced fluorescence measurement of CO in turbulent non-premixed bluff body flames. *Combustion and flame*, 132(1), pp.272-274.
- [62] Maier, C., Swirling Flames. [online]. Available at:<http://christophmaier.deviantart.com/art/Swirling-Flames-197006933> [Accessed 2 Nov. 2016].
- [63] Al-Abdeli, Y.M. and Masri, A.R., 2003. Stability characteristics and flowfields of turbulent non-premixed swirling flames. *Combustion Theory and Modelling*, 7(4), pp.731-766.
- [64] Masri, A.R., Pope, S.B. and Dally, B.B., 2000. Probability density function computations of a strongly swirling nonpremixed flame stabilized on a new burner. *Proceedings of the Combustion Institute*, 28(1), pp.123-131.
- [65] Cheng, R., Ultraclean Low-swirl Combustion Will Help Clear the Air. [online] Lawrence Berkeley National Laboratory. Available at: <https://eetd.lbl.gov/newsletter/nl14/eetd-nl14-3-lowswirl.html> [Accessed 2 Nov. 2016].
- [66] Birch, A.D. and Hargrave, G.K., 1989, January. Lift-off heights in underexpanded natural gas jet flames. In *Symposium (International) on Combustion* (Vol. 22, No. 1, pp. 825-831). Elsevier.

- [67] Donnerhack, S. and Peters, N., 1984. Stabilization heights in lifted methane-air jet diffusion flames diluted with nitrogen. *Combustion Science and Technology*, 41(1-2), pp.101-108.
- [68] Kalghatgi, G.T., 1981. Blow-out stability of gaseous jet diffusion flames. Part I: In still air. *Combustion Science and Technology*, 26(5-6), pp.233-239.
- [69] Watson, K.A., Lyons, K.M., Donbar, J.M. and Carter, C.D., 2000. Simultaneous Rayleigh imaging and CH-PLIF measurements in a lifted jet diffusion flame. *Combustion and flame*, 123(1), pp.252-265.
- [70] Muniz, L. and Mungal, M.G., 1997. Instantaneous flame-stabilization velocities in lifted-jet diffusion flames. *Combustion and Flame*, 111(1-2), pp.16IN131-30.
- [71] Kelman, J.B., Eltobaji, A.J. and Masri, A.R., 1998. Laser imaging in the stabilisation region of turbulent lifted flames. *Combustion science and technology*, 135(1-6), pp.117-134.
- [72] Vanquickenborne, L. and Van Tiggelen, A., 1966. The stabilization mechanism of lifted diffusion flames. *Combustion and Flame*, 10(1), pp.59-69.
- [73] Peters, N. and Williams, F.A., 1983. Liftoff characteristics of turbulent jet diffusion flames. *AIAA journal*, 21(3), pp.423-429.
- [74] Sanders, J.P.H. and Lamers, A.P.G.G., 1994. Modeling and calculation of turbulent lifted diffusion flames. *Combustion and flame*, 96(1-2), pp.22-33.

- [75] Janicka, J. and Peters, N., 1982, December. Prediction of turbulent jet diffusion flame lift-off using a PDF transport equation. In Symposium (International) on Combustion (Vol. 19, No. 1, pp. 367-374). Elsevier.
- [76] Müller, C.M., Breitbach, H. and Peters, N., 1994, December. Partially premixed turbulent flame propagation in jet flames. In Symposium (International) on Combustion (Vol. 25, No. 1, pp. 1099-1106). Elsevier.
- [77] Chen, M., Herrmann, M. and Peters, N., 2000. Flamelet modeling of lifted turbulent methane/air and propane/air jet diffusion flames. Proceedings of the Combustion Institute, 28(1), pp.167-174.
- [78] Bradley, D., Gaskell, P.H. and Gu, X.J., 1998, December. The mathematical modeling of liftoff and blowoff of turbulent non-premixed methane jet flames at high strain rates. In Symposium (International) on Combustion (Vol. 27, No. 1, pp. 1199-1206). Elsevier.
- [79] Ma, C.Y., Mahmud, T., Fairweather, M., Hampartsoumian, E. and Gaskell, P.H., 2002. Prediction of lifted, non-premixed turbulent flames using a mixedness-reactedness flamelet model with radiation heat loss. Combustion and flame, 128(1), pp.60-73.
- [80] Repp, S., Sadiki, A., Schneider, C., Hinz, A., Landefeld, T. and Janicka, J., 2002. Prediction of swirling confined diffusion flame with a Monte Carlo and a presumed-PDF-model. International Journal of Heat and Mass Transfer, 45(6), pp.1271-1285.
- [81] Sadiki, A., Repp, S., Schneider, C., Dreizler, A. and Janicka, J., 2003. Numerical and experimental investigations of confined swirling combustions

flows. *Progress in Computational Fluid Dynamics, an International Journal*, 3(2-4), pp.78-88.

[82] Devaud, C.B. and Bray, K.N.C., 2003. Assessment of the applicability of conditional moment closure to a lifted turbulent flame: first order model. *Combustion and Flame*, 132(1), pp.102-114.

[83] Kim, S.H., Huh, K.Y. and Fraser, R.A., 2000. Modeling autoignition of a turbulent methane jet by the conditional moment closure model. *Proceedings of the Combustion Institute*, 28(1), pp.185-191.

[84] Mastorakos, E. and Wright, Y.M., 2003. Simulations of turbulent spray auto-ignition with elliptic conditional moment closure. In *Proceedings of the European Combustion Meeting*.

[85] Kim, W.T. and Huh, K.Y., 2002. Numerical simulation of spray autoignition by the first-order conditional moment closure model. *Proceedings of the Combustion Institute*, 29(1), pp.569-576.

[86] Bradley, D., Emerson, D.R., Gaskell, P.H. and Gu, X.J., 2002. Mathematical modeling of turbulent non-premixed piloted-jet flames with local extinctions. *Proceedings of the combustion institute*, 29(2), pp.2155-2162.

[87] Cha, C.M. and Pitsch, H., 2002. Higher-order conditional moment closure modelling of local extinction and reignition in turbulent combustion. *Combustion Theory and Modelling*, 6(3), pp.425-437.

[88] Pierce, C.D., 2001. Progress-variable approach for large-eddy simulation of turbulent combustion (Doctoral dissertation, stanford university).

- [89]Pierce, C.D. and Moin, P., 2004. Progress-variable approach for large-eddy simulation of non-premixed turbulent combustion. *Journal of Fluid Mechanics*, 504, pp.73-97.
- [90] Pierce, C.D. and Moin, P., 1998. A dynamic model for subgrid-scale variance and dissipation rate of a conserved scalar. *Physics of Fluids (1994-present)*, 10(12), pp.3041-3044.
- [91] Janicka, J. and Kollmann, W., 1979, January. A two-variables formalism for the treatment of chemical reactions in turbulent H₂—Air diffusion flames. In *Symposium (International) on Combustion (Vol. 17, No. 1, pp. 421-430)*. Elsevier.
- [92] Bruel, P., Rogg, B. and Bray, K.N.C., 1991, January. On auto-ignition in laminar and turbulent non-premixed systems. In *Symposium (International) on Combustion (Vol. 23, No. 1, pp. 759-766)*. Elsevier.
- [93] Domingo, P., Vervisch, L. and Bray, K., 2002. Partially premixed flamelets in LES of nonpremixed turbulent combustion. *Combustion Theory and Modelling*, 6(4), pp.529-551.
- [94] Mura, A., Robin, V. and Champion, M., 2007. Modeling of scalar dissipation in partially premixed turbulent flames. *Combustion and flame*, 149(1), pp.217-224.
- [95] Ihme, Matthias, Chong M. Cha, and Heinz Pitsch. "Prediction of local extinction and re-ignition effects in non-premixed turbulent combustion using a flamelet/progress variable approach." *Proceedings of the Combustion Institute* 30, no. 1 (2005): 793-800.

[96] Ihme, Matthias, and Heinz Pitsch. "Prediction of extinction and reignition in nonpremixed turbulent flames using a flamelet/progress variable model: 1. A priori study and presumed PDF closure." *Combustion and flame* 155, no. 1 (2008): 70-89.

[97] Ihme, Matthias, and Heinz Pitsch. "Prediction of extinction and reignition in nonpremixed turbulent flames using a flamelet/progress variable model: 2. Application in LES of Sandia flames D and E." *Combustion and flame* 155, no. 1 (2008): 90-107.

[98] Chen, Z., Ruan, S. and Swaminathan, N., 2016. Numerical study of transient evolution of lifted jet flames: partially premixed flame propagation and influence of physical dimensions. *Combustion Theory and Modelling*, pp.1-21.

[99] Zhang, P., Barlow, R., Masri, A. and Wang, H., 2016. LES/PDF studies of joint statistics of mixture fraction and progress variable in piloted methane jet flames with inhomogeneous inlet flows. *Bulletin of the American Physical Society*, 61.

[100] Lefebvre, A.H. and Fletcher, R.S., 1973. A preliminary study on the influence of fuel staging on nitric oxide emissions from gas turbine combustors. 1973. 7.

[101] KATSUKI, M., MIZUTANI, Y. and SHIBUYA, K.I., 1976. Emissions from Gas Turbine Combustors: Part 1, An Experimental Study on a Model Combustor. *Bulletin of JSME*, 19(137), pp.1353-1359.

- [102] Jones, H.F.R.S., 1977, April. The mechanics of vibrating flames in tubes. In Proceedings of the Royal Society of London A: Mathematical, Physical and Engineering Sciences (Vol. 353, No. 1675, pp. 459-473). The Royal Society.
- [103] Friswell, N.J., 1979. The influence of fuel composition on smoke emission from gas-turbine-type combustors: effect of combustor design and operating conditions. *Combustion Science and Technology*, 19(3-4), pp.119-127.
- [104] Noyce, J.R., Sheppard, C.G.W. and Yamba, F.D., 1981. Measurements of mixing and species concentrations within a gas turbine type combustor.
- [105] Toral, H. and Whitelaw, J.H., 1982. Velocity and scalar characteristics of the isothermal and combusting flows in a combustor sector rig. *Combustion and Flame*, 45, pp.251-272.
- [106] Nakamura, S., Kawaguchi, O. and Sato, G.T., 1983. A study on the combustion in the primary zone region of a gas turbine-type continuous combustion chamber. Gas Turbine Society of Japan Paper 83-TOKYO-1GTC-30.
- [107] Chleboun, P.V., Nasser, S.H., Sebbowa, F.B. and Sheppard, C.G.W., 1984. An investigation of the interaction between multiple dilution jets and combustion products. In AGARD conference proceedings (No. 353, pp. 26-1). AGARD.
- [108] Krieger, G.C., Campos, A.P.V., Takehara, M.D.B., da Cunha, F.A. and Veras, C.G., 2015. Numerical simulation of oxy-fuel combustion for gas turbine applications. *Applied Thermal Engineering*, 78, pp.471-481.

- [109] Jones, W.P. and Toral, H., 1983. Temperature and composition measurements in a research gas turbine combustion chamber. *Combustion science and technology*, 31(5-6), pp.249-275.
- [110] Heitor, M.V. and Whitelaw, J.H., 1986. Velocity, temperature, and species characteristics of the flow in a gas-turbine combustor. *Combustion and Flame*, 64(1), pp.1-32.
- [111] Bicen, A.F. and Jones, W.P., 1986. Velocity characteristics of isothermal and combusting flows in a model combustor. *Combustion science and technology*, 49(1-2), pp.1-15.
- [112] McGuirk, J.J. and Palma, J.L., 1992. The influence of numerical parameters in the calculation of gas turbine combustor flows. *Computer methods in applied mechanics and engineering*, 96(1), pp.65-92.
- [113] Bicen, A.F. and Palma, J.M.L.M., 1986. Flow characteristics of swirlers of a model Tay Combustor. Tech. Rep. FS/86/36, Imperial College, London.
- [114] Bicen, A.F., Tse, D.G.N. and Whitelaw, J.H., 1990. Combustion characteristics of a model can-type combustor. *combustion and Flame*, 80(2), pp.111-125.
- [115] Di Mare, F., Jones, W.P. and Menzies, K.R., 2004. Large eddy simulation of a model gas turbine combustor. *Combustion and Flame*, 137(3), pp.278-294.
- [116] Di Mare, F. 2002. Large eddy simulation of reacting and non-reacting turbulent flows. PHD thesis. Department of Mechanical Engineering, Imperial College London.

- [117] Jones, W.P., 2002. Large eddy simulation of turbulent combustion processes. *Computer Physics Communications*, 147(1), pp.533-537.
- [118] Tse, D.G.N., 1988. Flow and combustion characteristics of model annular and can-type combustors (Doctoral dissertation, Imperial College London (University of London)).
- [119] Bicen, A.F., Tse, D.G.N. and Whitelaw, J.H., 1990, June. The Influence of Air/Fuel Ratio and Swirl Number on the Combustion Characteristics of a Model Combustor. In *ASME 1990 International Gas Turbine and Aeroengine Congress and Exposition* (pp. V003T06A003-V003T06A003). American Society of Mechanical Engineers.
- [120] Menzies, K.R., 2009. Grid adaption for gas turbine combustor calculations. PHD thesis. Department of Mechanical Engineering, Imperial College London.
- [121] Spalart, P.R. and Allmaras, S.R., 1992. A one equation turbulence model for aerodynamic flows. *AIAA journal*, 94.
- [122] Spalart, P.R., 2000. Strategies for turbulence modelling and simulations. *International Journal of Heat and Fluid Flow*, 21(3), pp.252-263.
- [123] Spalart, P.R., Jou, W.H., Strelets, M. and Allmaras, S.R., 1997. Comments on the feasibility of LES for wings, and on a hybrid RANS/LES approach. *Advances in DNS/LES*, 1, pp.4-8.
- [124] Rotta, J.C., 1951. Statistische theorie nichthomogener turbulenz. *Zeitschrift für Physik*, 129(6), pp.547-572.

- [125] Rotta, J.C., 1968. Über eine methode zur Berechnung turbulenter Scherströmungen. Aerodynamische Versuchsanstalt Göttingen, Report, (69), p.A14.
- [126] Florian Menter, C., Martin Kuntz, C. and Roland Bender, C., 2003. A scale adaptive simulation model for turbulent flow predictions. AIAA J, 767.
- [127] Menter, F.R. and Egorov, Y., 2009. Formulation of the Scale-Adaptive Simulation (SAS) model during the DESIDER Project. DESider-A European Effort on Hybrid RANS-LES Modelling, Springer, Berlin, pp.51-62.
- [128] Menter, F.R., Egorov, Y., 2004. Re-visiting the turbulent scale equation. In: Proc. IUTAM Symp. One Hundred Years of Boundary Layer Research. Springer, Göttingen.
- [129] Menter, F.R. and Egorov, Y., 2005. A scale-adaptive simulation model using two-equation models. AIAA paper, 1095, p.2005.
- [130] Menter, F.R. and Egorov, Y., 2005. Turbulence models based on the length-scale equation. In TSFP DIGITAL LIBRARY ONLINE. Begel House Inc..
- [131] Menter, F.R. and Egorov, Y., 2006. SAS turbulence modelling of technical flows. In Direct and Large-Eddy Simulation VI (pp. 687-694). Springer Netherlands.
- [132] Menter, F.R., Egorov, Y. and Rusch, D., 2006. Steady and unsteady flow modelling using the $k-\sqrt{k}L$ model. ICHMT DIGITAL LIBRARY ONLINE, 10.

- [133] Menter, F.R. and Egorov, Y., 2010. The scale-adaptive simulation method for unsteady turbulent flow predictions. Part 1: theory and model description. *Flow, Turbulence and Combustion*, 85(1), pp.113-138.
- [134] Fröhlich, J., Mellen, C.P., Rodi, W., Temmerman, L. and Leschziner, M.A., 2005. Highly resolved large-eddy simulation of separated flow in a channel with streamwise periodic constrictions. *Journal of Fluid Mechanics*, 526, pp.19-66.
- [135] Sjunnesson, A., Henriksson, R. and Lofstrom C., 1992. CARS measurements and visualization of reacting flows in bluff body stabilized flame. AIAA Paper. 92-3650.
- [136] Egorov, Y., Menter, F.R., Lechner, R. and Cokljat, D., 2010. The scale-adaptive simulation method for unsteady turbulent flow predictions. Part 2: Application to complex flows. *Flow, Turbulence and Combustion*, 85(1), pp.139-165.
- [137] Fossi, A., DeChamplain, A. and Akih-Kumgeh, B., 2015. Unsteady RANS and scale adaptive simulations of a turbulent spray flame in a swirled-stabilized gas turbine model combustor using tabulated chemistry. *International Journal of Numerical Methods for Heat & Fluid Flow*, 25(5), pp.1064-1088.
- [138] Zhang, K., Ghobadian, A. and Nouri, J.M., 2017. Comparative study of non-premixed and partially-premixed combustion simulations in a realistic Tay model combustor. *Applied Thermal Engineering*, 110, pp.910-920.

- [139] Launder, B.E. and Spalding, D.B., 1972. Lectures in mathematical models of turbulence.
- [140] Chemical-Kinetic Mechanisms for Combustion Applications", San Diego Mechanism web page, Mechanical and Aerospace Engineering (Combustion Research), University of California at San Diego (<http://combustion.ucsd.edu>).
- [141] Menter, F.R., 1994. Two-equation eddy-viscosity turbulence models for engineering applications. *AIAA journal*, 32(8), pp.1598-1605.
- [142] Lien, F.S. and Leschziner, M.A., 1994. Assessment of turbulence-transport models including non-linear RNG eddy-viscosity formulation and second-moment closure for flow over a backward-facing step. *Computers & Fluids*, 23(8), pp.983-1004.
- [143] Gibson, M.M. and Launder, B.E., 1978. Ground effects on pressure fluctuations in the atmospheric boundary layer. *Journal of Fluid Mechanics*, 86(03), pp.491-511.
- [144] Fu, S., Launder, B.E. and Leschziner, M.A., 1987. Modelling strongly swirling recirculating jet flow with Reynolds-stress transport closures. In 6th Symposium on Turbulent Shear Flows (pp. 17-6).
- [145] Launder, B.E., 1989. Second - moment closure and its use in modelling turbulent industrial flows. *International Journal for Numerical Methods in Fluids*, 9(8), pp.963-985.

- [146] Spalding, D.B., 1971, January. Mixing and chemical reaction in steady confined turbulent flames. In Symposium (International) on Combustion (Vol. 13, No. 1, pp. 649-657). Elsevier.
- [147] Effelsberg, E. and Peters, N., 1989, January. Scalar dissipation rates in turbulent jets and jet diffusion flames. In Symposium (International) on Combustion (Vol. 22, No. 1, pp. 693-700). Elsevier.
- [148] Poinso, T. and Veynante, D., 2005. Theoretical and numerical combustion. RT Edwards, Inc.
- [149] Peters, N., 1999. The turbulent burning velocity for large-scale and small-scale turbulence. *Journal of Fluid mechanics*, 384, pp.107-132.
- [150] Zimont, V., Polifke, W., Bettelini, M. and Weisenstein, W., 1997, June. An efficient computational model for premixed turbulent combustion at high Reynolds numbers based on a turbulent flame speed closure. In ASME 1997 International Gas Turbine and Aeroengine Congress and Exhibition (pp. V002T06A054-V002T06A054). American Society of Mechanical Engineers.
- [151] Metghalchi, M. and Keck, J.C., 1982. Burning velocities of mixtures of air with methanol, isooctane, and indolene at high pressure and temperature. *Combustion and flame*, 48, pp.191-210.
- [152] Götgens, J., Mauss, F. and Peters, N., 1992, December. Analytic approximations of burning velocities and flame thicknesses of lean hydrogen, methane, ethylene, ethane, acetylene, and propane flames. In Symposium (International) on Combustion (Vol. 24, No. 1, pp. 129-135). Elsevier.

- [153] Zimont, V.L. and Lipatnikov, A.N., 1995. A numerical model of premixed turbulent combustion of gases. *Chem. Phys. Rep*, 14(7), pp.993-1025.
- [154] Candel, S.M. and Poinso, T.J., 1990. Flame stretch and the balance equation for the flame area. *Combustion Science and Technology*, 70(1-3), pp.1-15.
- [155] Colin, O., Benkenida, A. and Angelberger, C., 2003. 3D modeling of mixing, ignition and combustion phenomena in highly stratified gasoline engines. *Oil & gas science and technology*, 58(1), pp.47-62.
- [156] ANSYS® , Academic Research, Release 14.5.
- [157] Crocker, D.S., Fuller, E.J. and Smith, C.E., 1997. Fuel nozzle aerodynamic design using CFD analysis. *Journal of engineering for gas turbines and power*, 119(3), pp.527-534.
- [158] Jasak, H., Weller, H.G. and Gosman, A.D., 1999. High resolution NVD differencing scheme for arbitrarily unstructured meshes. *International journal for numerical methods in fluids*, 31(2), pp.431-449.
- [159] Hinze, J.O. and Turbulence, J.H., 1975. McGraw Hill, New York (1975). *Turbulence* (2d ed.), McGraw Hill, New York, p.724.

APPENDIX A

Derivation of Transport Equation for Correlation Tensor R_{ij}

The correlation tensor has been defined as:

$$R_{ij}(x, t, r, \tau) = \overline{u'_i(x, t)u'_j(x^1, t^1)} \quad (\text{A.1})$$

Where $x^1 = x + r$ and $t^1 = t + \tau$. The transport equation of R_{ij} is derived by summing up the following pair of equations:

$$D^{(i)}\{R_{ij}\} = \overline{u'_j(x^{(1)}, t^{(1)})N_i\{x, t\}} \quad (\text{A.2})$$

$$D^{(j)}\{R_{ij}\} = \overline{u'_i(x, t)N_j\{x^{(1)}, t^{(1)}\}} \quad (\text{A.3})$$

Where $N_i\{x, t\}$ and $N_j\{x^{(1)}, t^{(1)}\}$ are the transport equations for instantaneous velocity fluctuation at different time and position that $x^1 = x + r$ and $t^1 = t + \tau$.

First, the $N_i\{x, t\}$ is derived from the Navier-Stokes equation:

$$\begin{cases} \frac{\partial u_i}{\partial x_k} = 0 \\ \frac{\partial u_i}{\partial t} + u_k \frac{\partial u_i}{\partial x_k} = f_i - \frac{1}{\rho} \frac{\partial p}{\partial x_k} + \frac{\partial^2 u_i}{\partial x_k \partial x_k} \end{cases} \quad (\text{A.4})$$

Where f_i represents any possible external forces. By expanding equation A.4 using the average and the fluctuation of each quantity, we have:

$$\begin{cases} \frac{\partial(\overline{u_i} + u'_i)}{\partial x_k} = 0 \\ \frac{\partial(\overline{u_i} + u'_i)}{\partial t} + (\overline{u_k} + u'_k) \frac{\partial(\overline{u_i} + u'_i)}{\partial x_k} = (\overline{f_i} + f'_i) - \frac{1}{\rho} \frac{\partial(\overline{p} + p')}{\partial x_k} + \nu \frac{\partial^2(\overline{u_i} + u'_i)}{\partial x_k \partial x_k} \end{cases} \quad (\text{A.5})$$

By time averaging equation A.5, we have:

$$\left\{ \begin{array}{l} \frac{\partial \bar{u}_i}{\partial x_i} = 0 \\ \frac{\partial \bar{u}_i}{\partial t} + \bar{u}_k \frac{\partial \bar{u}_i}{\partial x_k} = \bar{f}_i - \frac{1}{\rho} \frac{\partial(\bar{p})}{\partial x_k} + \frac{\partial^2 \bar{u}_i}{\partial x_k \partial x_k} - \nu \frac{\partial \overline{u'_i u'_k}}{\partial x_k} \end{array} \right. \quad (\text{A.6})$$

By subtracting equation A.6 from equation A.5 and rearranging the equation, we have:

$$\begin{aligned} N_i\{x, t\} = & \\ & \frac{\partial u'_i(x, t)}{\partial t} + \bar{u}_k \frac{\partial u'_i(x, t)}{\partial x_k} + u'_k \frac{\partial \bar{u}_i(x, t)}{\partial x_k} + \frac{\partial(u'_i(x, t)u'_k(x, t))}{\partial x_k} - \frac{\partial(\overline{u'_i(x, t)u'_k(x, t)})}{\partial x_k} - f'_i + \\ & \frac{1}{\rho} \frac{\partial p'(x, t)}{\partial x_k} - \nu \frac{\partial^2 u'_i(x, t)}{\partial x_k \partial x_k} = 0 \end{aligned} \quad (\text{A.7})$$

Similarly, we have:

$$\begin{aligned} N_j\{x^{(1)}, t^{(1)}\} = & \\ & \frac{\partial u'_j(x^{(1)}, t^{(1)})}{\partial t^{(1)}} + \overline{u_k(x^{(1)}, t^{(1)})} \frac{\partial u'_j(x^{(1)}, t^{(1)})}{\partial x_k^{(1)}} + u'_k(x^{(1)}, t^{(1)}) \frac{\partial \bar{u}_j(x^{(1)}, t^{(1)})}{\partial x_k^{(1)}} + \\ & \frac{\partial(u'_j(x^{(1)}, t^{(1)})u'_k(x^{(1)}, t^{(1)}))}{\partial x_k^{(1)}} - \frac{\partial(\overline{u'_j(x^{(1)}, t^{(1)})u'_k(x^{(1)}, t^{(1)})})}{\partial x_k^{(1)}} - f'_j + \frac{1}{\rho} \frac{\partial p'(x^{(1)}, t^{(1)})}{\partial x_k^{(1)}} - \\ & \nu \frac{\partial^2 u'_j(x^{(1)}, t^{(1)})}{\partial x_k^{(1)} \partial x_k^{(1)}} = 0 \end{aligned} \quad (\text{A.8})$$

Substituting equation A.7 and A.8 into equation A.2 and A.3

$$\begin{aligned} D^{(i)}\{R_{ij}\} = \overline{u'_j(x^{(1)}, t^{(1)})} N_i\{x, t\} = & \\ & \overline{u'_j(x^{(1)}, t^{(1)})} \frac{\partial u'_i(x, t)}{\partial t} + \overline{u'_j(x^{(1)}, t^{(1)})} \bar{u}_k \frac{\partial u'_i(x, t)}{\partial x_k} + \overline{u'_j(x^{(1)}, t^{(1)})} u'_k \frac{\partial \bar{u}_i(x, t)}{\partial x_k} + \\ & \overline{u'_j(x^{(1)}, t^{(1)})} \frac{\partial(u'_i(x, t)u'_k(x, t))}{\partial x_k} - \overline{u'_j(x^{(1)}, t^{(1)})} \frac{\partial(\overline{u'_i(x, t)u'_k(x, t)})}{\partial x_k} - \overline{u'_j(x^{(1)}, t^{(1)})} f'_i + \\ & \overline{u'_j(x^{(1)}, t^{(1)})} \frac{1}{\rho} \frac{\partial p'(x, t)}{\partial x_k} - \overline{u'_j(x^{(1)}, t^{(1)})} \nu \frac{\partial^2 u'_i(x, t)}{\partial x_k \partial x_k} = 0 \end{aligned} \quad (\text{A.9})$$

$$\begin{aligned}
D^{(j)}\{R_{ij}\} &= \overline{u'_i(x,t)N_j\{x^{(1)},t^{(1)}\}} = \\
&\overline{u'_i(x,t)\frac{\partial u'_j(x^{(1)},t^{(1)})}{\partial t^{(1)}}} + \overline{u'_i(x,t)\overline{u_k}(x^{(1)},t^{(1)})\frac{\partial u'_j(x^{(1)},t^{(1)})}{\partial x_k^{(1)}}} + \\
&\overline{u'_i(x,t)u'_k(x^{(1)},t^{(1)})\frac{\partial \overline{u_j}(x^{(1)},t^{(1)})}{\partial x_k^{(1)}}} + \overline{u'_i(x,t)\frac{\partial (u'_j(x^{(1)},t^{(1)})u'_k(x^{(1)},t^{(1)}))}{\partial x_k^{(1)}}} - \\
&\overline{u'_i(x,t)\frac{\partial (\overline{u_j}(x^{(1)},t^{(1)})u'_k(x^{(1)},t^{(1)}))}{\partial x_k^{(1)}}} - \overline{u'_i(x,t)f'_j} + \overline{u'_i(x,t)\frac{1}{\rho}\frac{\partial p'(x^{(1)},t^{(1)})}{\partial x_k^{(1)}}} - \\
&\overline{u'_i(x,t)v\frac{\partial^2 u'_j(x^{(1)},t^{(1)})}{\partial x_k^{(1)}\partial x_k^{(1)}}} = 0 \quad (\text{A.10})
\end{aligned}$$

To simplify above equations, the following differentiation equations apply:

$$\overline{u'_i(x,t)\frac{\partial u'_j(x^{(1)},t^{(1)})}{\partial x_k^{(1)}}} = \frac{\partial R_{ij}}{\partial r_k} \quad (\text{A.11})$$

$$\overline{u'_j(x^{(1)},t^{(1)})\frac{\partial u'_i(x,t)}{\partial x_k^{(1)}}} = \frac{\partial R_{ij}}{\partial x_k} - \frac{\partial R_{ij}}{\partial r_k} \quad (\text{A.12})$$

$$\overline{\frac{\partial u'_i(x,t)}{\partial x_k^{(1)}}\frac{\partial u'_j(x^{(1)},t^{(1)})}{\partial x_k^{(1)}}} = \frac{\partial^2 R_{ij}}{\partial x_k \partial r_k} - \frac{\partial^2 R_{ij}}{\partial r_k \partial r_k} \quad (\text{A.13})$$

$$\overline{\frac{\partial u'_i(x,t)}{\partial t}\frac{\partial u'_j(x^{(1)},t^{(1)})}{\partial t^{(1)}}} = \frac{\partial^2 R_{ij}}{\partial t \partial \tau} - \frac{\partial^2 R_{ij}}{\partial \tau^2} \quad (\text{A.14})$$

Therefore, equation A.9 is simplified term by term:

$$\overline{u'_j(x^{(1)},t^{(1)})\frac{\partial u'_i(x,t)}{\partial t}} = \frac{\partial R_{ij}}{\partial t} - \frac{\partial R_{ij}}{\partial \tau} \quad (\text{A.15})$$

$$\overline{u'_j(x^{(1)},t^{(1)})\overline{u_k}(x,t)\frac{\partial u'_i(x,t)}{\partial x_k}} = \overline{u_k(x,t)}\left(\frac{\partial R_{ij}}{\partial x_k} - \frac{\partial R_{ij}}{\partial r_k}\right) \quad (\text{A.16})$$

$$\overline{u'_j(x^{(1)},t^{(1)})u'_k(x,t)\frac{\partial \overline{u_i}(x,t)}{\partial x_k}} = R_{kj}\frac{\partial \overline{u_i}(x,t)}{\partial x_k} \quad (\text{A.17})$$

$$\overline{u'_j(x^{(1)},t^{(1)})\frac{\partial (u'_i(x,t)u'_k(x,t))}{\partial x_k}} = \frac{\partial R_{(ik),j}}{\partial x_k} - \frac{\partial R_{(ik),j}}{\partial r_k} \quad (\text{A.18})$$

$$-\overline{u'_j(x^{(1)}, t^{(1)}) \frac{\partial(\overline{u'_i(x,t)u'_k(x,t)})}{\partial x_k}} = 0 \quad (\text{A.19})$$

$$-\overline{u'_j(x^{(1)}, t^{(1)})f'_i} = -\overline{f'_i u'_j} \quad (\text{A.20})$$

$$\overline{u'_j(x^{(1)}, t^{(1)}) \frac{1}{\rho} \frac{\partial p'(x,t)}{\partial x_k}} = \frac{1}{\rho} \left(\frac{\partial \overline{p' u'_j}}{\partial x_i} - \frac{\partial \overline{p' u'_i}}{\partial r_i} \right) \quad (\text{A.21})$$

Where $\overline{p' u'_j} = \overline{p'(x,t)u'_j(x^{(1)}, t^{(1)})}$.

$$\begin{aligned} &-\overline{u'_j(x^{(1)}, t^{(1)})v \frac{\partial^2 u'_i(x,t)}{\partial x_k \partial x_k}} = \\ &-\overline{\left[v \left(\frac{\partial}{\partial x_k} \left[\frac{\partial u'_i(x,t)}{\partial x_k} u'_j(x^{(1)}, t^{(1)}) \right] - \frac{\partial u'_i(x,t)}{\partial r_k} \left[\frac{\partial u'_i(x,t)}{\partial x_k} u'_j(x^{(1)}, t^{(1)}) \right] \right) \right]} = \\ &-\left[v \left(\frac{\partial}{\partial x_k} \left(\frac{\partial R_{ij}}{\partial x_k} - \frac{\partial R_{ij}}{\partial r_k} \right) - \frac{\partial}{\partial r_k} \left(\frac{\partial R_{ij}}{\partial x_k} - \frac{\partial R_{ij}}{\partial r_k} \right) \right) \right] = -v \left(\frac{\partial^2 R_{ij}}{\partial x_k \partial x_k} - 2 \frac{\partial^2 R_{ij}}{\partial x_k \partial r_k} + \frac{\partial^2 R_{ij}}{\partial r_k \partial r_k} \right) \end{aligned} \quad (\text{A.22})$$

And equation A.10 is simplified term by term:

$$\overline{u'_i(x,t) \frac{\partial u'_j(x^{(1)}, t^{(1)})}{\partial t^{(1)}}} = \frac{\partial R_{ij}}{\partial \tau} \quad (\text{A.23})$$

$$\overline{u'_i(x,t) \overline{u'_k}(x^{(1)}, t^{(1)}) \frac{\partial u'_j(x^{(1)}, t^{(1)})}{\partial x_k^{(1)}}} = \overline{u'_k}(x^{(1)}, t^{(1)}) \frac{\partial R_{ij}}{\partial r_k} \quad (\text{A.24})$$

$$\overline{u'_i(x,t) u'_k(x^{(1)}, t^{(1)}) \frac{\partial \overline{u'_j}(x^{(1)}, t^{(1)})}{\partial x_k^{(1)}}} = R_{ik} \frac{\partial \overline{u'_j}(x^{(1)}, t^{(1)})}{\partial x_k^{(1)}} \quad (\text{A.25})$$

$$\overline{u'_i(x,t) \frac{\partial(u'_j(x^{(1)}, t^{(1)})u'_k(x^{(1)}, t^{(1)}))}{\partial x_k^{(1)}}} = \frac{\partial R_{i(jk)}}{\partial r_k} \quad (\text{A.26})$$

$$\overline{u'_i(x,t) \frac{\partial(\overline{u'_j(x^{(1)}, t^{(1)})u'_k(x^{(1)}, t^{(1)})})}{\partial x_k^{(1)}}} = 0 \quad (\text{A.27})$$

$$\overline{u'_i(x,t)f'_j} = -\overline{f'_j u'_i} \quad (\text{A.28})$$

$$\overline{u'_i(x, t) \frac{1}{\rho} \frac{\partial p'(x^{(1)}, t^{(1)})}{\partial x_k^{(1)}}} = \frac{1}{\rho} \frac{\partial \overline{u'_i p'}}{\partial r_j} \quad (\text{A.29})$$

Where $\overline{u'_i p'} = \overline{p'(x^{(1)}, t^{(1)}) u'_i(x, t)}$.

$$-\overline{u'_i(x, t) v \frac{\partial^2 u'_j(x^{(1)}, t^{(1)})}{\partial x_k^{(1)} \partial x_k^{(1)}}} = -\frac{\partial}{\partial r_k} (u'_i(x, t) \frac{\partial u'_j(x^{(1)}, t^{(1)})}{\partial x_k^{(1)}}) = -v \frac{\partial^2 R_{ij}}{\partial r_k \partial r_k} \quad (\text{A.30})$$

By summing up all the terms above, we have equation A.9 and A.10

rearranged to:

$$D^{(i)}\{R_{ij}\} = \frac{\partial R_{ij}}{\partial t} - \frac{\partial R_{ij}}{\partial \tau} + \overline{u_k}(x, t) \left(\frac{\partial R_{ij}}{\partial x_k} - \frac{\partial R_{ij}}{\partial r_k} \right) + R_{kj} \frac{\partial \overline{u_i}(x, t)}{\partial x_k} + \frac{\partial R_{(ik),j}}{\partial x_k} - \frac{\partial R_{(ik),j}}{\partial r_k} - \overline{f'_i u'_j} + \frac{1}{\rho} \left(\frac{\partial \overline{p' u'_j}}{\partial x_i} - \frac{\partial \overline{p' u'_j}}{\partial r_i} \right) - v \left(\frac{\partial^2 R_{ij}}{\partial x_k \partial x_k} - 2 \frac{\partial^2 R_{ij}}{\partial x_k \partial r_k} + \frac{\partial^2 R_{ij}}{\partial r_k \partial r_k} \right) = 0 \quad (\text{A.31})$$

$$D^{(j)}\{R_{ij}\} = \frac{\partial R_{ij}}{\partial \tau} + \overline{u_k}(x^{(1)}, t^{(1)}) \frac{\partial R_{ij}}{\partial r_k} + R_{ik} \frac{\partial \overline{u_j}(x^{(1)}, t^{(1)})}{\partial x_k^{(1)}} + \frac{\partial R_{i(jk)}}{\partial r_k} + \overline{f'_j u'_i} + \frac{1}{\rho} \frac{\partial \overline{u'_i p'}}{\partial r_j} - v \frac{\partial^2 R_{ij}}{\partial r_k \partial r_k} = 0 \quad (\text{A.32})$$

Summing up equation A.30 and A.31, the transport equation for correlation

tensor R_{ij} is given as:

$$D\{R_{ij}\} = D^{(i)}\{R_{ij}\} + D^{(j)}\{R_{ij}\} = \frac{\partial R_{ij}}{\partial t} + \overline{u_k}(x, t) \frac{\partial R_{ij}}{\partial x_k} + \left(\overline{u_k}(x^{(1)}, t^{(1)}) - \overline{u_k}(x, t) \right) \frac{\partial R_{ij}}{\partial r_k} + R_{kj} \frac{\partial \overline{u_i}(x, t)}{\partial x_k} + R_{ik} \frac{\partial \overline{u_j}(x^{(1)}, t^{(1)})}{\partial x_k^{(1)}} + \frac{\partial R_{(ik),j}}{\partial x_k} - \left(\frac{\partial R_{(ik),j}}{\partial r_k} - \frac{\partial R_{i(jk)}}{\partial r_k} \right) + \frac{1}{\rho} \left(\frac{\partial \overline{p' u'_j}}{\partial x_i} - \frac{\partial \overline{p' u'_j}}{\partial r_i} + \frac{\partial \overline{u'_i p'}}{\partial r_j} \right) - v \left(\frac{\partial^2 R_{ij}}{\partial x_k \partial x_k} - 2 \frac{\partial^2 R_{ij}}{\partial x_k \partial r_k} + 2 \frac{\partial^2 R_{ij}}{\partial r_k \partial r_k} \right) - \overline{f'_i u'_j} - \overline{f'_j u'_i} = 0 \quad (\text{A.33})$$

APPENDIX B

Explanation of Regime Diagram for Premixed Combustion

To explain the premixed combustion regimes, fundamental scales of flame and turbulence are first introduced and then the relationship between the vertical and horizontal axis of Figure 3.4 are derived.

As is widely accepted, the smallest scales of turbulence are defined as Kolmogorov scales at which the turbulent kinetic energy is dissipated into heat through eddy dissipation ε due to eddy viscosity. Therefore, the Kolmogorov scales can be written as:

$$\eta = \left(\frac{\nu^3}{\varepsilon}\right)^{1/4} \quad (\text{B.1})$$

$$t_\eta = \left(\frac{\nu}{\varepsilon}\right)^{1/2} \quad (\text{B.2})$$

$$V_\eta = (\nu\varepsilon)^{1/4} \quad (\text{B.3})$$

Where η is the Kolmogorov length scale, ν is the eddy viscosity, t_η is the Kolmogorov time scale and V_η is the Kolmogorov velocity scale.

The scales of flame are defined as:

$$l_F = \frac{D}{S_L} \quad (\text{B.4})$$

$$t_F = \frac{D}{S_L^2} \quad (\text{B.5})$$

Where l_F is the flame length scale, D is thermal diffusivity, t_F is the flame time scale and S_L is the laminar flame speed.

The common turbulence Reynolds number can be defined as in equation B.6:

$$Re_t = \frac{v_n' l}{\nu} \quad (\text{B.6})$$

Where the v_n' represents the turn-over velocity of eddy.

By assuming the Prandtl number (note there might be confusion between Prandtl number and Schmidt number) equals to unity which is the ratio of eddy viscosity to thermal diffusivity in equation B.7 so that $\nu = D$:

$$Pr = \frac{\nu}{D} = 1 \quad (\text{B.7})$$

And by applying equation B.4 and B.7 to equation B.6, one could write:

$$Re_t = \frac{v_n' l}{\nu} = \frac{v_n' l}{D} = \frac{v_n' l}{S_L l_F} \quad (\text{B.8})$$

To understand Figure 3.4, one Damköhler number and two Karlovitz number are defined below so that the Damköhler number equals to the ratio between turbulence dominated mixing time and chemical reaction:

$$Da = \frac{\text{mixing time}}{\text{reaction time}} = \frac{\frac{l}{v_n'}}{\frac{l_F}{S_L}} = \frac{v_n' l}{u' l_F} \quad (\text{B.9})$$

The 1st Karlovitz number is defined as:

$$Ka = \frac{\text{flame time scale}}{\text{Kolmogorov time scale}} = \frac{t_F}{t_\eta} \quad (\text{B.10})$$

By applying equation B.5, and applying unity Prandtl number, equation B.10 can be rearranged to (Note: $t_\eta = \frac{\nu}{V_\eta^2}$ by combining equation B.2 and B.3):

$$Ka = \frac{t_F}{t_\eta} = \frac{\frac{D}{S_L^2}}{\frac{\nu}{V_\eta^2}} = \frac{V_\eta^2}{S_L^2} \quad (\text{B.11})$$

By applying equation B.4, and unity Prandtl number again (Note: $V_\eta = \frac{v^2}{\eta^2}$ by combining equation B.1 and B.3):

$$Ka = \frac{t_F}{t_\eta} = \frac{V_\eta^2}{S_L^2} = \frac{\frac{v^2}{\eta^2}}{\frac{D^2}{l_F^2}} = \frac{l_F^2}{\eta^2} \quad (\text{B.12})$$

The 2nd Karlovitz number is defined as:

$$Ka_\xi = \frac{\text{flame reaction zone thickness}}{\text{Kolmogorov length scale}} = \frac{l_\xi^2}{\eta^2} = \xi^2 Ka \quad (\text{B.13})$$

Where the reaction zone thickness $l_\xi = \xi l_F$ and ξ takes the value of 0.1 for methane-oxygen reaction, i.e. the reaction zone thickness is one-tenth the thickness of diffusion/preheat region.

To achieve the relationship amongst v'_n/S_L , Re_t , Ka , Ka_ξ , and l/l_F as shown in Figure 3.4, equation B.1 is squared on both sides and by substituting the scaled dissipation rate $\varepsilon = v'_n{}^3/l$ and $v^3 = D^3 = S_L^3 l_F^3$ from equation B.4 into the squared equation B.1, one could have:

$$\eta^2 = \left(\frac{v'_n{}^3}{\varepsilon}\right)^{1/2} = \left(S_L^3 l_F^3 \frac{l}{v'_n{}^3}\right)^{1/2} = \left(\frac{S_L^3}{v'_n{}^3} l_F^3 l\right)^{1/2} \quad (\text{B.14})$$

Rearrange equation B.14:

$$\left(\frac{v'_n}{S_L}\right)^3 = \frac{l_F^3 l}{\eta^4} = \frac{l_F^4}{\eta^4} \frac{l}{l_F} \quad (\text{B.15})$$

Finally, equation B.12 is then substituted into equation B.15 to have the relationship amongst v'_n/S_L , Ka , and l/l_F and by combining equation B.8, it is summarized that:

$$\frac{v'_n}{S_L} = Re_t \left(\frac{l}{l_F}\right)^{-1} = Ka^{\frac{2}{3}} \left(\frac{l}{l_F}\right)^{1/3} \quad (\text{B.16})$$

The region at which the Reynolds number larger than unity is discussed here:

$$(1) \text{ If } Ka = \frac{\text{flame scale}}{\text{Kolmogorov scale}} = \frac{t_F}{t_\eta} = \frac{v_\eta^2}{S_L^2} = \frac{l_F^2}{\eta^2} = 1, \text{ then } \frac{v'_n}{S_L} = \left(\frac{l}{l_F}\right)^{1/3} \text{ (straight}$$

line in log-log graph), and $l_F = \eta$: the laminar flame thickness equals to the Kolmogorov length scale.

$$(2) \text{ If } Ka = \frac{\text{flame scale}}{\text{Kolmogorov scale}} = \frac{t_F}{t_\eta} = \frac{v_\eta^2}{S_L^2} = \frac{l_F^2}{\eta^2} < 1, \text{ then } l_F < \eta, \text{ the flame is}$$

embedded in to the smallest eddy, two sub-conditions are defined:

a. If when $Ka < 1$ and $v'_n < S_L$, laminar flame propagation speed dominates over the flame front corrugation, i.e. **wrinkled flame**.

b. If when $Ka < 1$ and $v'_n > S_L$, flame front corrugation dominated over the laminar flame propagation, i.e. **corrugated flame**.

$$(3) \text{ If } Ka = \frac{\text{flame scale}}{\text{Kolmogorov scale}} = \frac{t_F}{t_\eta} = \frac{v_\eta^2}{S_L^2} = \frac{l_F^2}{\eta^2} > 1, \text{ then } l_F > \eta, \text{ the smallest}$$

eddy penetrates into the reaction zone, two sub-conditions are defined:

a. If $Ka_\xi = \frac{\text{flame reaction zone thicknes}}{\text{Kolmogorov length scale}} = \frac{l_\xi^2}{\eta^2} = \xi^2 Ka < 1$, although eddy penetrates into the flamelet, the smallest eddy length scale is still larger than reaction zone thickness, the flamelet assumption is still valid, the region is called **thin reaction zone** region.

b. If $Ka_\xi = \frac{\text{flame reaction zone thicknes}}{\text{Kolmogorov length scale}} = \frac{l_\xi^2}{\eta^2} = \xi^2 Ka > 1$, the smallest eddy length scale breaks into the reaction zone, and therefore, the zone is called **broken reaction zone**.

Now, the problem with ECFM model is discussed here:

When ECFM model has been used in the main text of this thesis, the model is seen to have suppressed the chemical reaction rate by presenting the lower value of progress variable across the whole domain of the combustor. It must be realized that the model is based on the assumption that the premixed flame is located in the regime supporting for the corrugated flame.

In the corrugated flame regime, an assumption must be followed that the turn-over velocity of eddy is larger than the laminar flame speed that instead of having little wrinkling due to the propagation of flame, the flame is highly corrugated, i.e. the eddies which are turning faster than the flame front propagating speed will push the flame front around.

If the Gibson length scale is defined so that it is equivalent to the length scale at which the eddy turn-over velocity equals to the flame front propagating speed (i.e., Gibson length scale is the flame front wrinkling limit), the flame corrugation assumption can be fully covered only if it satisfied:

$$l_F < \Delta < l_G$$

Where l_F is the laminar flame thickness, l_G is the Gibson length scale and Δ is the smallest resolved scale.

In LES, if Δ is properly described by linking it to the local cell size, the entire length scales smaller than Gibson length scale can be directly resolved to provide an accurate prediction of flame area corrugation. However, in SSTKWSAS, there is no explicit dependence between the resolved scales and the local cell size. The use of large courant number in this thesis may indicate

the smallest resolved scale is larger than the Gibson length scale (or only part of the resolved scales are smaller than Gibson scale), and therefore, the flame area corrugation cannot be completely considered.

APPENDIX C

Calculation of Properties

Calculation of temperature:

To calculate the mean temperature of mixtures, equation C.1 is used as below:

$$\bar{T} = (1 - C)\bar{T}_u + C\bar{T}_b \quad (\text{C.1})$$

Where the mean unburnt temperature \bar{T}_u is directly read from the Pre-PDF polynomial:

$$T_u = \sum_{n=0}^3 C_n (\bar{Z})^n \quad (\text{C.2})$$

Where C_n takes the coefficients shown in Table C.1:

C0	C1	C2	C3
318	-3.10E-11	8.63E-11	-5.60E-11

Table C.1: Polynomial coefficients for calculating unburnt temperature

The burnt temperature T_b is calculated from equation C.3:

$$T_b = \iint p(\bar{Z}, X_{st}) T(\bar{Z}, X_{st}) d\bar{Z} dX_{st} \quad (\text{C.3})$$

Calculation of density:

To calculate the density, equation C.4 is used as below:

$$\rho = (1 - c)\rho_u + c\rho_b \quad (\text{C.4})$$

The burnt density ρ_b is calculated from:

$$\frac{1}{\rho_b} = \iint p(\bar{\mathbf{Z}}, X_{st}) \frac{1}{\rho(\bar{\mathbf{Z}}, X_{st})} d\bar{\mathbf{Z}} dX_{st} \quad (\text{C.5})$$

And the unburnt density is read from Pre-PDF polynomial as well (calculated from idea gas law $M = \rho_u RT_u / P_{op}$ where M is the mean molecular weight and P_{op} is the operating pressure 1atm):

$$\rho_u = \sum_{n=0}^3 C_n (\bar{\mathbf{Z}})^n \quad (\text{C.6})$$

Where C_n takes the coefficients shown in Table C.2:

C0	C1	C2	C3
1.105569	0.390674	0.090071	0.103513

Table C.2: Polynomial coefficients for calculating unburnt density

The unburnt properties such as unburnt specific heat capacity ($J/(Kg \cdot K)$) ($C_{p,unburnt\ mixture} = \sum_i C_{p,i} x_i$ where $C_{p,i}$ is the specific heat capacity of individual species, x_i is the mass fraction of each species) and thermal diffusivity (m^2/s) ($\alpha = \lambda / \rho_u C_{p,unburnt\ mixture}$) follow the same polynomial rule, but the coefficients are given below in Table C.3 and C.4:

C0	C1	C2	C3
1.01E+03	7.5E+02	1.44E-10	-9.5E-11

Table C.3: Polynomial coefficients for calculating unburnt specific heat capacity

C0	C1	C2	C3
4.06E-05	-4.30E-05	2.52E-05	-7.60E-06

Table C.4: Polynomial coefficients for calculating unburnt thermal diffusivity

APPENDIX D

Chemkin Chemical Reaction Mechanisms

Detail chemical kinetics are shown below starting with 'Elements' and Species' and followed by the 'Reactions'. The first column in the kinetics below 'REACTION' represent individual chemical reactions and second to forth columns represent the exponential factor, the fudge factor and the activation energy factor appeared in Arrhenius equation for high pressure limit. The 'LOW/' and 'TROE/' used for reactions represent rate parameters for low pressure limit in Lindemann formula and Troe's formula. In general, these rate parameters for low pressure limit or fall-off region depend largely on buffer gas. Hence, rows starting with a species name and followed by a '/*/' represents enhancement factor for buffer gas and the low-pressure-limiting rate constant must be multiplied by * for a certain species.

ELEMENTS

N	AR	HE	H	O	C
---	----	----	---	---	---

END

SPECIES

N2	AR	HE	H	O2
OH	O	H2	H2O	HO2
H2O2	CO	CO2	HCO	CH3
CH4	CH2O	T-CH2	S-CH2	C2H4

CH3O	C2H5	C2H6	CH	C2H2
C2H4OOH	OC2H3OOH	C2H3	CH2CHO	C2H4O
HCCO	CH2CO	C2H	CH2OH	CH3OH
CH3CHO	CH3CO	C2H5OH	CH2CH2OH	CH3CHOH
CH3CH2O	C3H4	C3H3	C3H5	C3H6
C3H8	I-C3H7	N-C3H7	C3H6OOH	OC3H5OOH

END

REACTIONS

H+O2	OH+O	3,52E+19	-0.700	17069.79		
H2+O<=>	OH+H	5,06E+07	2.670	6290.63		
H2+OH<=>	H2O+H	1,17E+12	1.300	3635.28		
H2O+O<=>	2OH	7,00E+08	2.330	14548.28		
2H+M<=>	H2+M	1,30E+21	-1.000	0.00		
AR/0.50/	HE/0.50/		H2/2.50/	H2O/12.00/	CO/1.90/	CO2/3.80/
H+OH+M<=>	H2O+M	4,00E+25	-2.000	0.00		
AR/0.38/	HE/0.38/		H2/2.50/	H2O/12.00/	CO/1.90/	CO2/3.80/
2O+M<=>	O2+M	6,17E+18	-0.500	0.00		
AR/0.20/	HE/0.20/		H2/2.50/	H2O/12.00/	CO/1.90/	CO2/3.80/
H+O+M<=>	OH+M	4,71E+21	-1.000	0.00		
AR/0.75/	HE/0.75/		H2/2.50/	H2O/12.00/	CO/1.90/	CO2/3.80/
O+OH+M<=>	HO2+M	8,00E+18	0.000	0.00		
AR/0.75/	HE/0.75/		H2/2.50/	H2O/12.00/	CO/1.90/	CO2/3.80/
H+O2(+M)<=>	HO2(+M)	4,65E+15	0.440	0.00		
AR/0.70/	HE/0.70/		H2/2.50/	H2O/16.00/	CO/1.20/	CO2/2.40/ C2H6/1.50/
	LOW/		5,75E+22	-1.400	0.00	/
	TROE/		0.5	1,00E-30	1,00E+30	/
HO2+H<=>	2OH	7,08E+16	0.000	294.93		

HO2+H<=>H2+O2	1,66E+16	0.000	822.90			
HO2+H<=>H2O+O	3,10E+16	0.000	1720.84			
HO2+O<=>OH+O2	2,00E+16	0.000	0.00			
HO2+OH(+M)<=>H2O+O2(+M)	4,50E+17	0.000	10929.73			
	LOW/	2,89E+16	0.000	-497.13	/	
	TROE/	1	1	1,00E+07	1,00E+07	/
2OH(+M)<=>H2O2(+M)	9,55E+16	-0.270	0.00			
AR/0.70/	HE/0.40/	H2/2.50/	H2O/6.00/	CO/1.50/	CO2/2.00/	
	LOW/	2,76E+28	-3.200	0.000	/	
	TROE/	0.57	1,00E+30	0	/	
2HO2(+M)<=>H2O2+O2(+M)	1,94E+14	0.000	-1408.94			
	LOW/	1,03E+17	0.000	11042.07	/	
	TROE/	1	1	1,00E+07	1,00E+07	/
H2O2+H<=>HO2+H2	2,30E+16	0.000	7950.05			
H2O2+H<=>H2O+OH	1,00E+16	0.000	3585.09			
H2O2+OH(+M)<=>H2O+HO2(+M)	7,59E+16	0.000	7272.94			
	LOW/	1,74E+15	0.000	1434.03	/	
	TROE/	1	1	1,00E+07	1,00E+07	/
H2O2+O<=>HO2+OH	9,63E+09	2.000	3991.40			
CO+O(+M)<=>CO2(+M)	1,80E+14	0.000	2384.08			
AR/0.70/	HE/0.70/	H2/2.50/	H2O/12.00/	CO/2.00/	CO2/4.00/	
	LOW/	1,55E+27	-2.790	4190.97	/	
	TROE/	1	1	1,00E+07	1,00E+07	/
CO+OH<=>CO2+H	4,40E+09	1.500	-740.92			
CO+HO2<=>CO2+OH	2,00E+16	0.000	22944.55			

	CO+O2<=>CO2+O	1,00E+15	0.000	47700.05			
	HCO+M<=>CO+H+M	1,86E+20	-1.000	17000.48			
H2/1.90/	H2O/12.00/		CO/2.50/	CO2/2.50/			
	HCO+H<=>CO+H2	5,00E+16	0.000	0.00			
	HCO+O<=>CO+OH	3,00E+16	0.000	0.00			
	HCO+O<=>CO2+H	3,00E+16	0.000	0.00			
	HCO+OH<=>CO+H2O	3,00E+16	0.000	0.00			
	HCO+O2<=>CO+HO2	7,58E+15	0.000	409.89			
	HCO+CH3<=>CO+CH4	5,00E+16	0.000	0.00			
	H+HCO(+M)<=>CH2O(+M)	1,09E+15	0.480	-260.04			
AR/0.70/	H2/2.00/		H2O/6.00/	CO/1.50/	CO2/2.00/	CH4/2.00/	C2H6/3.00/
	LOW/		1,35E+27	-2.570	424.95	/	
	TROE/		0.7824	271	2755	6570	/
	CH2O+H<=>HCO+H2	5,74E+10	1.900	2748.57			
	CH2O+O<=>HCO+OH	3,50E+16	0.000	3513.38			
	CH2O+OH<=>HCO+H2O	3,90E+13	0.890	406.31			
	CH2O+O2<=>HCO+HO2	6,00E+16	0.000	40674.00			
	CH2O+HO2<=>HCO+H2O2	4,11E+07	2.500	10210.33			
	CH4+H<=>H2+CH3	1,30E+07	3.000	8037.76			
	CH4+OH<=>H2O+CH3	1,60E+10	1.830	2782.03			
	CH4+O<=>CH3+OH	1,90E+12	1.440	8675.91			
	CH4+O2<=>CH3+HO2	3,98E+16	0.000	56890.54			
	CH4+HO2<=>CH3+H2O2	9,03E+15	0.000	24641.49			
	CH3+H<=>T-CH2+H2	1,80E+17	0.000	15105.16			
	CH3+H<=>S-CH2+H2	1,55E+17	0.000	13479.92			
	CH3+OH<=>S-CH2+H2O	4,00E+16	0.000	2502.39			
	CH3+O<=>CH2O+H	8,43E+16	0.000	0.00			
	CH3+T-CH2<=>C2H4+H	4,22E+16	0.000	0.00			

CH3+HO2<=>CH3O+OH	5,00E+15	0.000	0.00			
CH3+O2<=>CH2O+OH	3,30E+14	0.000	8941.20			
CH3+O2<=>CH3O+O	1,10E+16	0.000	27820.03			
2CH3<=>C2H4+H2	1,00E+17	0.000	32002.87			
2CH3<=>C2H5+H	3,16E+16	0.000	14698.85			
H+CH3(+M)<=>CH4(+M)	1,27E+19	-0.630	382.89			
AR/0.70/	H2/2.00/	H2O/6.00/	CO/1.50/	CO2/2.00/	CH4/2.00/	
	LOW/	2,47E+36	-4.760	2440.01	/	
	TROE/	0.783	74	2941	6964	/
2CH3(+M)<=>C2H6(+M)	1,81E+16	0.000	0.00			
AR/0.70/	H2/2.00/	H2O/6.00/	CO/1.50/	CO2/2.00/	CH4/2.00/	C2H6/3.00/
	LOW/	1,27E+44	-7.000	2762.91	/	
	TROE/	0.62	73	1.2e+03	/	
S-CH2+OH<=>CH2O+H	3,00E+16	0.000	0.00			
S-CH2+O2<=>CO+OH+H	3,13E+16	0.000	0.00			
S-CH2+CO2<=>CO+CH2O	3,00E+15	0.000	0.00			
S-CH2+M<=>T-CH2+M	6,00E+15	0.000	0.00			
H2/2.40/	H2O/15.40/	CO/1.80/	CO2/3.60/			
T-CH2+H<=>CH+H2	6,02E+15	0.000	-1787.76			
T-CH2+OH<=>CH2O+H	2,50E+16	0.000	0.00			
T-CH2+OH<=>CH+H2O	1,13E+10	2.000	2999.52			
T-CH2+O<=>CO+2H	8,00E+16	0.000	0.00			
T-CH2+O<=>CO+H2	4,00E+16	0.000	0.00			
T-CH2+O2<=>CO2+H2	2,63E+15	0.000	1491.40			
T-CH2+O2<=>CO+OH+H	6,58E+15	0.000	1491.40			
2T-CH2<=>C2H2+2H	1,00E+17	0.000	0.00			
CH+O<=>CO+H	4,00E+16	0.000	0.00			
CH+O2<=>HCO+O	1,77E+14	0.760	-478.01			

CH+H2O<=>CH2O+H	1,17E+18	-0.750	0.00			
CH+CO2<=>HCO+CO	4,80E+04	3.220	-3226.58			
CH3O+H<=>CH2O+H2	2,00E+16	0.000	0.00			
CH3O+H<=>S-CH2+H2O	1,60E+16	0.000	0.00			
CH3O+OH<=>CH2O+H2O	5,00E+15	0.000	0.00			
CH3O+O<=>OH+CH2O	1,00E+16	0.000	0.00			
CH3O+O2<=>CH2O+HO2	4,28E-10	7.600	-3537.28			
CH3O+M<=>CH2O+H+M	7,78E+16	0.000	13513.38			
AR/0.70/	H2/2.00/	H2O/6.00/	CO/1.50/	CO2/2.00/	CH4/2.00/	
C2H6+H<=>C2H5+H2	5,40E+05	3.500	5210.33			
C2H6+O<=>C2H5+OH	1,40E+03	4.300	2772.47			
C2H6+OH<=>C2H5+H2O	2,20E+10	1.900	1123.33			
C2H6+CH3<=>C2H5+CH4	5,50E+02	4.000	8293.50			
C2H6(+M)<=>C2H5+H(+M)	8,85E+23	-1.230	102222.75			
AR/0.70/	H2/2.00/	H2O/6.00/	CO/1.50/	CO2/2.00/	CH4/2.00/	C2H6/3.00/
	LOW/	4,90E+45	-6.430	107169.93	/	
	TROE/	0.84	125	2219	6882	/
C2H6+HO2<=>C2H5+H2O2	1,32E+16	0.000	20469.89			
C2H5+H<=>C2H4+H2	3,00E+16	0.000	0.00			
C2H5+O<=>C2H4+OH	3,06E+16	0.000	0.00			
C2H5+O<=>CH3+CH2O	4,24E+16	0.000	0.00			
C2H5+O2<=>C2H4+HO2	7,50E+17	-1.000	4799.95			
C2H5+O2<=>C2H4OOH	2,00E+15	0.000	0.00			
C2H4OOH<=>C2H4+HO2	4,00E+37	-7.200	23000.00			
C2H4OOH+O2<=>OC2H3OOH+OH	7,50E+08	1.300	-5799.95			
OC2H3OOH<=>CH2O+HCO+OH	1,00E+18	0.000	43000.00			
C2H5(+M)<=>C2H4+H(+M)	1,11E+13	1.037	36768.64			
AR/0.70/	H2/2.00/	H2O/6.00/	CO/1.50/	CO2/2.00/	CH4/2.00/	

	LOW/	3,99E+36	-4.990	40000.00	/
	TROE/	0.168	1.2e+03	0	/
	C2H4+H<=>C2H3+H2	4,49E+10	2.120	13360.42	
	C2H4+OH<=>C2H3+H2O	5,53E+08	2.310	2963.67	
	C2H4+O<=>CH3+HCO	2,25E+09	2.080	0.00	
	C2H4+O<=>CH2CHO+H	1,21E+09	2.080	0.00	
	2C2H4<=>C2H3+C2H5	5,01E+17	0.000	64700.05	
	C2H4+O2<=>C2H3+HO2	4,22E+16	0.000	57623.09	
	C2H4+HO2<=>C2H4O+OH	2,23E+15	0.000	17189.29	
	C2H4O+HO2<=>CH3+CO+H2O2	4,00E+15	0.000	17007.65	
	C2H4+M<=>C2H3+H+M	2,60E+20	0.000	96568.12	
AR/0.70/	H2/2.00/	H2O/6.00/	CO/1.50/	CO2/2.00/	CH4/2.00/
	C2H4+M<=>C2H2+H2+M	3,50E+19	0.000	71532.03	
AR/0.70/	H2/2.00/	H2O/6.00/	CO/1.50/	CO2/2.00/	CH4/2.00/
	C2H3+H<=>C2H2+H2	4,00E+16	0.000	0.00	
	C2H3(+M)<=>C2H2+H(+M)	6,38E+12	1.000	37626.67	
AR/0.70/	H2/2.00/	H2O/6.00/	CO/1.50/	CO2/2.00/	CH4/2.00/
	LOW/	1,51E+17	0.100	32685.95	/
	TROE/	0.3	1,00E+30	1,00E-30	/
	C2H3+O2<=>CH2O+HCO	1,70E+32	-5.312	6503.11	
	C2H3+O2<=>CH2CHO+O	7,00E+17	-0.611	5262.43	
	C2H3+O2<=>C2H2+HO2	5,19E+18	-1.260	3312.62	
	C2H2+O<=>HCCO+H	4,00E+17	0.000	10659.66	
	C2H2+O<=>T-CH2+CO	1,60E+17	0.000	9894.84	
	C2H2+O2<=>CH2O+CO	4,60E+18	-0.540	44933.08	
	C2H2+OH<=>CH2CO+H	1,90E+10	1.700	999.04	
	C2H2+OH<=>C2H+H2O	3,37E+10	2.000	14000.96	
	CH2CO+H<=>CH3+CO	1,50E+12	1.430	2688.81	

CH2CO+O<=>T-CH2+CO2	2,00E+16	0.000	2294.46		
CH2CO+O<=>HCCO+OH	1,00E+16	0.000	2000.48		
CH2CO+CH3<=>C2H5+CO	9,00E+13	0.000	0.00		
HCCO+H<=>S-CH2+CO	1,50E+17	0.000	0.00		
HCCO+OH<=>HCO+CO+H	2,00E+15	0.000	0.00		
HCCO+O<=>2CO+H	9,64E+16	0.000	0.00		
HCCO+O2<=>2CO+OH	2,88E+10	1.700	1001.43		
HCCO+O2<=>CO2+CO+H	1,40E+10	1.700	1001.43		
C2H+OH<=>HCCO+H	2,00E+16	0.000	0.00		
C2H+O<=>CO+CH	1,02E+16	0.000	0.00		
C2H+O2<=>HCCO+O	6,02E+14	0.000	0.00		
C2H+O2<=>CH+CO2	4,50E+18	0.000	25095.60		
C2H+O2<=>HCO+CO	2,41E+15	0.000	0.00		
CH2OH+H<=>CH2O+H2	3,00E+16	0.000	0.00		
CH2OH+H<=>CH3+OH	2,50E+20	-0.930	5126.91		
CH2OH+OH<=>CH2O+H2O	2,40E+16	0.000	0.00		
CH2OH+O2<=>CH2O+HO2	5,00E+15	0.000	0.00		
CH2OH+M<=>CH2O+H+M	5,00E+16	0.000	25119.50		
AR/0.70/	H2/2.00/	H2O/6.00/	CO/1.50/	CO2/2.00/	CH4/2.00/
CH3O+M<=>CH2OH+M	1,00E+17	0.000	19120.46		
AR/0.70/	H2/2.00/	H2O/6.00/	CO/1.50/	CO2/2.00/	CH4/2.00/
CH2CO+OH<=>CH2OH+CO	1,02E+16	0.000	0.00		
CH3OH+OH<=>CH2OH+H2O	1,44E+09	2.000	-838.91		
CH3OH+OH<=>CH3O+H2O	4,40E+09	2.000	1505.74		
CH3OH+H<=>CH2OH+H2	1,35E+06	3.200	3490.68		
CH3OH+H<=>CH3O+H2	6,83E+04	3.400	7239.96		
CH3OH+O<=>CH2OH+OH	1,00E+16	0.000	4684.51		
CH3OH+HO2<=>CH2OH+H2O2	8,00E+16	0.000	19383.37		

CH3OH+O2<=>CH2OH+HO2	2,00E+16	0.000	44933.08			
CH3OH(+M)<=>CH3+OH(+M)	1,90E+19	0.000	91729.92			
AR/0.70/	H2/2.00/	H2O/6.00/	CO/1.50/	CO2/2.00/	CH4/2.00/	
	LOW/	2,95E+47	-7.350	95460.09	/	
	TROE/	0.414	2.8e+02	5.5e+03	/	
CH2CHO<=>CH2CO+H	1,05E+40	-7.189	44340.34			
CH2CHO+H<=>CH3+HCO	5,00E+16	0.000	0.00			
CH2CHO+H<=>CH2CO+H2	2,00E+16	0.000	0.00			
CH2CHO+O<=>CH2O+HCO	1,00E+17	0.000	0.00			
CH2CHO+OH<=>CH2CO+H2O	3,00E+16	0.000	0.00			
CH2CHO+O2<=>CH2O+CO+OH	3,00E+13	0.000	0.00			
CH2CHO+CH3<=>C2H5+CO+H	4,90E+17	-0.500	0.00			
CH2CHO+HO2<=>CH2O+HCO+OH	7,00E+15	0.000	0.00			
CH2CHO+HO2<=>CH3CHO+O2	3,00E+15	0.000	0.00			
CH2CHO<=>CH3+CO	1,17E+46	-9.800	43799.95			
CH3CHO<=>CH3+HCO	7,00E+18	0.000	81700.05			
CH3CO(+M)<=>CH3+CO(+M)	3,00E+15	0.000	16700.05			
AR/0.70/	H2/2.00/	H2O/6.00/	CO/1.50/	CO2/2.00/	CH4/2.00/	
	LOW/	1,20E+18	0.000	12500.00	/	
	TROE/	1	1	1,00E+07	1,00E+07	/
CH3CHO+OH<=>CH3CO+H2O	3,37E+15	0.000	-619.98			
CH3CHO+OH<=>CH2CHO+H2O	3,37E+14	0.000	-619.98			
CH3CHO+O<=>CH3CO+OH	1,77E+21	-1.900	2979.92			
CH3CHO+O<=>CH2CHO+OH	3,72E+16	-0.200	3559.99			
CH3CHO+H<=>CH3CO+H2	4,66E+16	-0.300	2989.96			
CH3CHO+H<=>CH2CHO+H2	1,85E+15	0.400	5359.94			
CH3CHO+CH3<=>CH3CO+CH4	3,90E-04	5.800	2200.05			
CH3CHO+CH3<=>CH2CHO+CH4	2,45E+04	3.100	5729.92			

CH3CHO+HO2<=>CH3CO+H2O2	3,60E+22	-2.200	14000.00		
CH3CHO+HO2<=>CH2CHO+H2O2	2,32E+14	0.400	14900.10		
CH3CHO+O2<=>CH3CO+HO2	1,00E+17	0.000	42200.05		
C2H5OH(+M)<=>CH3+CH2OH(+M)	5,00E+18	0.000	82000.00		
AR/0.70/	H2/2.00/	H2O/6.00/	CO/1.50/	CO2/2.00/	CH4/2.00/
	LOW/	3,00E+19	0.000	58000.00	/
	TROE/	0.5	1,00E-30	1,00E+30	/
C2H5OH(+M)<=>C2H4+H2O(+M)	8,00E+16	0.000	65000.00		
AR/0.70/	H2/2.00/	H2O/6.00/	CO/1.50/	CO2/2.00/	CH4/2.00/
	LOW/	1,00E+20	0.000	54000.00	/
	TROE/	0.5	1,00E-30	1,00E+30	/
C2H5OH+OH<=>CH2CH2OH+H2O	1,81E+14	0.400	717.02		
C2H5OH+OH<=>CH3CHOH+H2O	3,09E+13	0.500	-380.02		
C2H5OH+OH<=>CH3CH2O+H2O	1,05E+13	0.800	717.02		
C2H5OH+H<=>CH2CH2OH+H2	1,90E+10	1.800	5099.90		
C2H5OH+H<=>CH3CHOH+H2	2,58E+10	1.600	2830.07		
C2H5OH+H<=>CH3CH2O+H2	1,50E+10	1.600	3039.91		
C2H5OH+O<=>CH2CH2OH+OH	9,41E+10	1.700	5460.09		
C2H5OH+O<=>CH3CHOH+OH	1,88E+10	1.900	1820.03		
C2H5OH+O<=>CH3CH2O+OH	1,58E+10	2.000	4450.05		
C2H5OH+CH3<=>CH2CH2OH+CH4	2,19E+05	3.200	9619.98		
C2H5OH+CH3<=>CH3CHOH+CH4	7,28E+05	3.000	7950.05		
C2H5OH+CH3<=>CH3CH2O+CH4	1,45E+05	3.000	7650.10		
C2H5OH+HO2<=>CH3CHOH+H2O2	8,20E+06	2.500	10799.95		
C2H5OH+HO2<=>CH2CH2OH+H2O2	2,43E+07	2.500	15799.95		
C2H5OH+HO2<=>CH3CH2O+H2O2	3,80E+15	0.000	24000.00		
C2H4+OH<=>CH2CH2OH	2,41E+14	0.000	-2380.02		
C2H5+HO2<=>CH3CH2O+OH	4,00E+16	0.000	0.00		

CH3CH2O+M<=>CH3CHO+H+M	5,60E+37	-5.900	25299.95			
AR/0.70/	H2/2.00/	H2O/6.00/	CO/1.50/	CO2/2.00/	CH4/2.00/	
CH3CH2O+M<=>CH3+CH2O+M	5,35E+40	-7.000	23799.95			
AR/0.70/	H2/2.00/	H2O/6.00/	CO/1.50/	CO2/2.00/	CH4/2.00/	
CH3CH2O+O2<=>CH3CHO+HO2	4,00E+13	0.000	1099.90			
CH3CH2O+CO<=>C2H5+CO2	4,68E+05	3.200	5380.02			
CH3CH2O+H<=>CH3+CH2OH	3,00E+16	0.000	0.00			
CH3CH2O+H<=>C2H4+H2O	3,00E+16	0.000	0.00			
CH3CH2O+OH<=>CH3CHO+H2O	1,00E+16	0.000	0.00			
CH3CHOH+O2<=>CH3CHO+HO2	4,82E+16	0.000	5020.08			
CH3CHOH+O<=>CH3CHO+OH	1,00E+17	0.000	0.00			
CH3CHOH+H<=>C2H4+H2O	3,00E+16	0.000	0.00			
CH3CHOH+H<=>CH3+CH2OH	3,00E+16	0.000	0.00			
CH3CHOH+HO2<=>CH3CHO+2OH	4,00E+16	0.000	0.00			
CH3CHOH+OH<=>CH3CHO+H2O	5,00E+15	0.000	0.00			
CH3CHOH+M<=>CH3CHO+H+M	1,00E+17	0.000	25000.00			
AR/0.70/	H2/2.00/	H2O/6.00/	CO/1.50/	CO2/2.00/	CH4/2.00/	
C3H4+O<=>C2H4+CO	2,00E+10	1.800	1000.00			
CH3+C2H2<=>C3H4+H	2,56E+12	1.100	13643.88			
C3H4+O<=>HCCO+CH3	7,30E+15	0.000	2250.00			
C3H3+H(+M)<=>C3H4(+M)	3,00E+16	0.000	0.00			
	LOW/	9,00E+18	1.000	0.00	/	
	TROE/	0.5	1,00E+30	0	/	
C3H3+HO2<=>C3H4+O2	2,50E+15	0.000	0.00			
C3H4+OH<=>C3H3+H2O	5,30E+09	2.000	2000.00			
C3H3+O2<=>CH2CO+HCO	3,00E+13	0.000	2868.07			
C3H4+H(+M)<=>C3H5(+M)	4,00E+16	0.000	0.00			

	LOW/	3,00E+27	-2.000	0.00	/			
	TROE/	0.8	1,00E+30	0	/			
C3H5+H<=>C3H4+H2	1,80E+16	0.000	0.00					
C3H5+O2<=>C3H4+HO2	4,99E+18	-1.400	22428.06					
C3H5+CH3<=>C3H4+CH4	3,00E+15	-0.320	-130.98					
C2H2+CH3(+M)<=>C3H5(+M)	6,00E+11	0.000	0.00					
	LOW/	2,00E+12	1.000	0.00	/			
	TROE/	0.5	1,00E+30	0	/			
C3H5+OH<=>C3H4+H2O	6,00E+15	0.000	0.00					
C3H3+HCO<=>C3H4+CO	2,50E+16	0.000	0.00					
C3H3+HO2<=>OH+CO+C2H3	8,00E+14	0.000	0.00					
C3H4+O2<=>CH3+HCO+CO	4,00E+17	0.000	41826.00					
C3H6+O<=>C2H5+HCO	3,50E+10	1.650	-972.75					
C3H6+OH<=>C3H5+H2O	3,10E+09	2.000	-298.28					
C3H6+O<=>CH2CO+CH3+H	1,20E+11	1.650	327.44					
C3H6+H<=>C3H5+H2	1,70E+08	2.500	2492.83					
C3H5+H(+M)<=>C3H6(+M)	2,00E+17	0.000	0.00					
AR/0.70/	H2/2.00/	H2O/6.00/	CO/1.50/	CO2/2.00/	CH4/2.00/	C2H6/3.00/		
	LOW/	1,33E+63	-12.000	5967.97	/			
	TROE/	0.02	1097	1097	6860	/		
C3H5+HO2<=>C3H6+O2	2,66E+15	0.000	0.00					
C3H5+HO2<=>OH+C2H3+CH2O	3,00E+15	0.000	0.00					
C2H3+CH3(+M)<=>C3H6(+M)	2,50E+16	0.000	0.00					
AR/0.70/	H2/2.00/	H2O/6.00/	CO/1.50/	CO2/2.00/	CH4/2.00/	C2H6/3.00/		
	LOW/	4,27E+61	-11.940	9770.55	/			
	TROE/	0.175	1341	6,00E+04	1,01E+07	/		

C3H6+H<=>C2H4+CH3	1,60E+25	-2.390	11185.47				
CH3+C2H3<=>C3H5+H	1,50E+27	-2.830	18618.55				
C3H8(+M)<=>CH3+C2H5(+M)	1,10E+20	0.000	84392.93				
	LOW/	7,83E+21	0.000	64978.01		/	
	TROE/	0.76	1.9e+03	38		/	
C3H8+O2<=>I-C3H7+HO2	4,00E+16	0.000	47500.00				
C3H8+O2<=>N-C3H7+HO2	4,00E+16	0.000	50932.12				
C3H8+H<=>I-C3H7+H2	1,30E+09	2.400	4471.08				
C3H8+H<=>N-C3H7+H2	1,33E+09	2.540	6761.47				
C3H8+O<=>I-C3H7+OH	4,76E+07	2.710	2107.31				
C3H8+O<=>N-C3H7+OH	1,90E+08	2.680	3718.45				
C3H8+OH<=>N-C3H7+H2O	1,00E+13	1.000	1599.90				
C3H8+OH<=>I-C3H7+H2O	2,00E+10	-1.600	-99.90				
C3H8+HO2<=>I-C3H7+H2O2	9,64E+06	2.600	13917.30				
C3H8+HO2<=>N-C3H7+H2O2	4,76E+07	2.550	16491.40				
I-C3H7+C3H8<=>N-C3H7+C3H8	8,40E+00	4.200	8675.91				
C3H6+H(+M)<=>I-C3H7(+M)	1,33E+16	0.000	1560.71				
AR/0.70/	H2/2.00/	H2O/6.00/	CO/1.50/	CO2/2.00/	CH4/2.00/	C2H6/3.00/	
	LOW/	8,70E+45	-7.500	4732.31		/	
	TROE/	1	1000	645.4	6844	/	
I-C3H7+O2<=>C3H6+HO2	1,30E+14	0.000	0.00				
N-C3H7(+M)<=>CH3+C2H4(+M)	1,23E+16	-0.100	30210.33				
	LOW/	5,49E+52	-10.000	35778.92		/	
	TROE/	-1.17	251	1,00E-15	1185	/	
H+C3H6(+M)<=>N-C3H7(+M)	1,33E+16	0.000	3260.04				
AR/0.70/	H2/2.00/	H2O/6.00/	CO/1.50/	CO2/2.00/	CH4/2.00/	C2H6/3.00/	

	LOW/		6,26E+41	-6.660	7000.48	/	
	TROE/		1	1000	1310	4.81e+04	/
N-C3H7+O2<=>C3H6+HO2		3,50E+19	-1.600	3500.00			
N-C3H7+O2<=>C3H6OOH		2,00E+15	0.000	0.00			
C3H6OOH<=>C3H6+HO2		2,50E+38	-8.300	22000.00			
C3H6OOH+O2<=>OC3H5OOH+OH		1,50E+11	0.000	-7000.00			
OC3H5OOH<=>CH2CHO+CH2O+OH		1,00E+18	0.000	43000.00			
END							

APPENDIX E

More Predicted Numerical Results

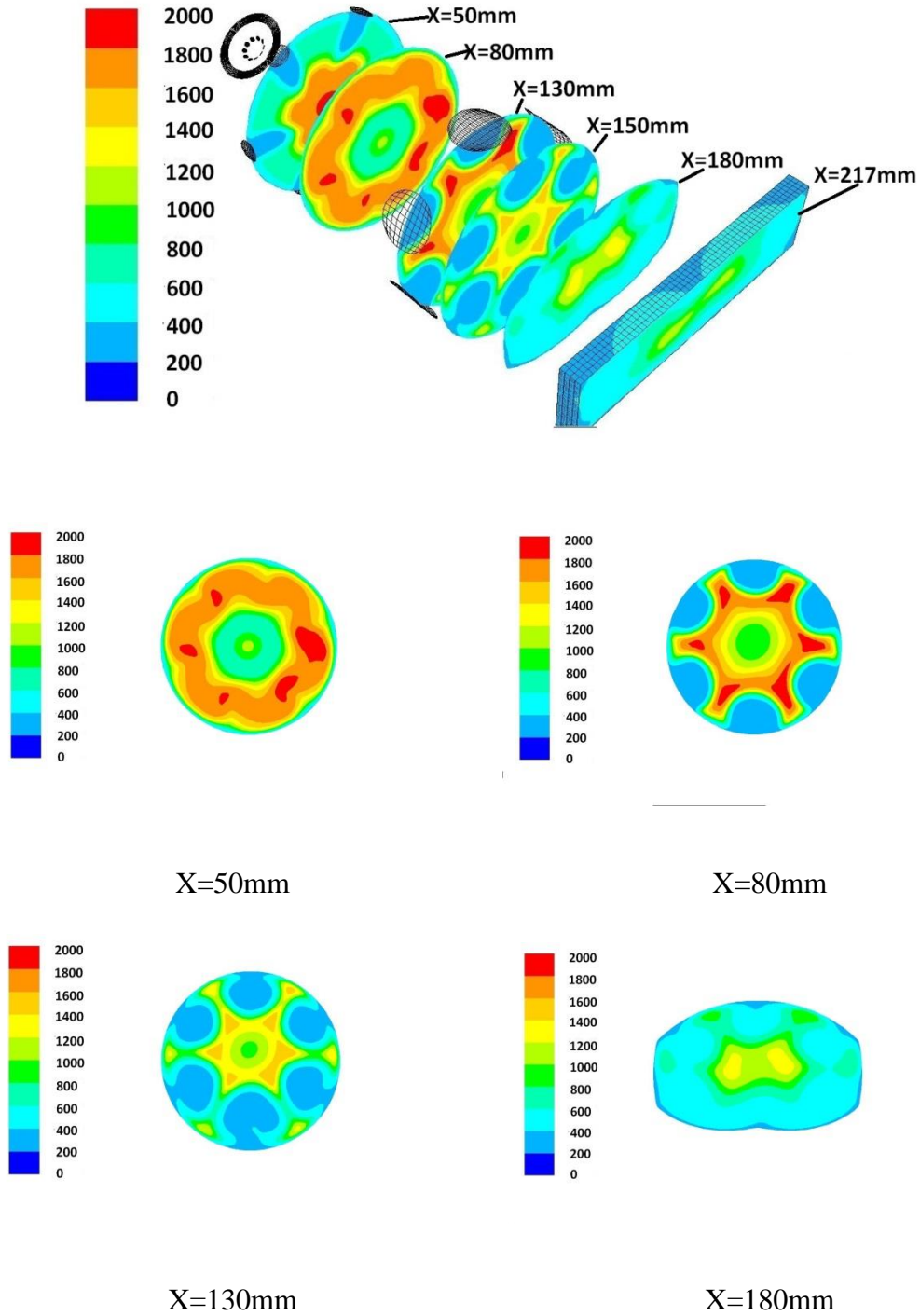


Figure E.1: Time-averaged flame temperature at various plane of combustor (unsteady SSTKW).

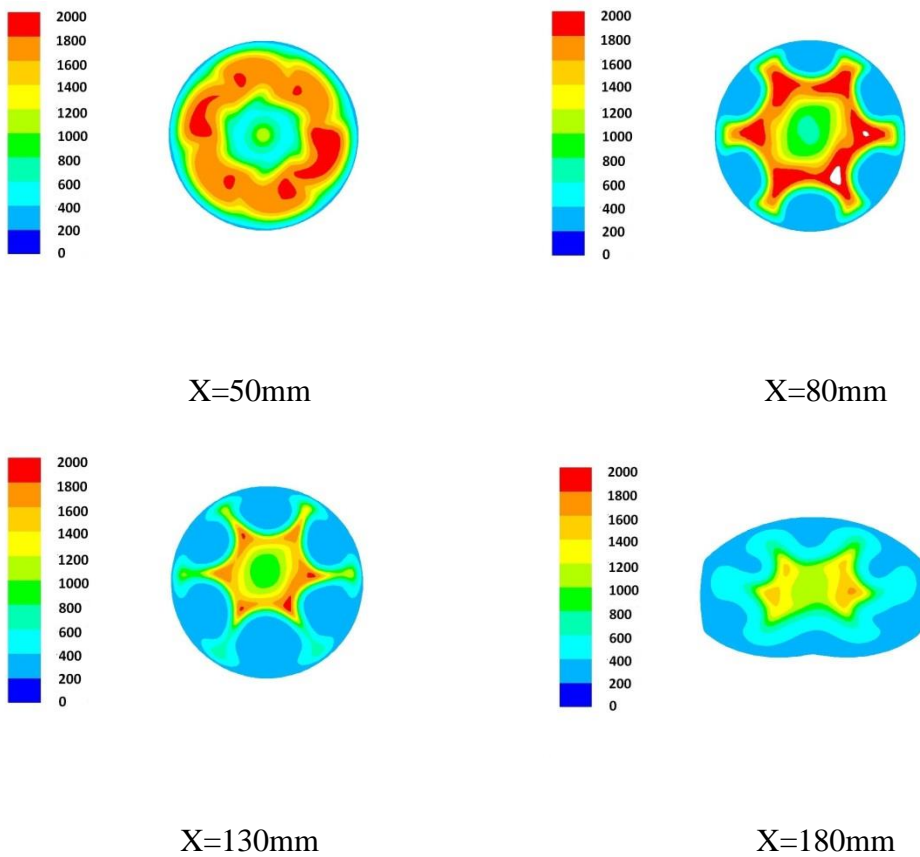
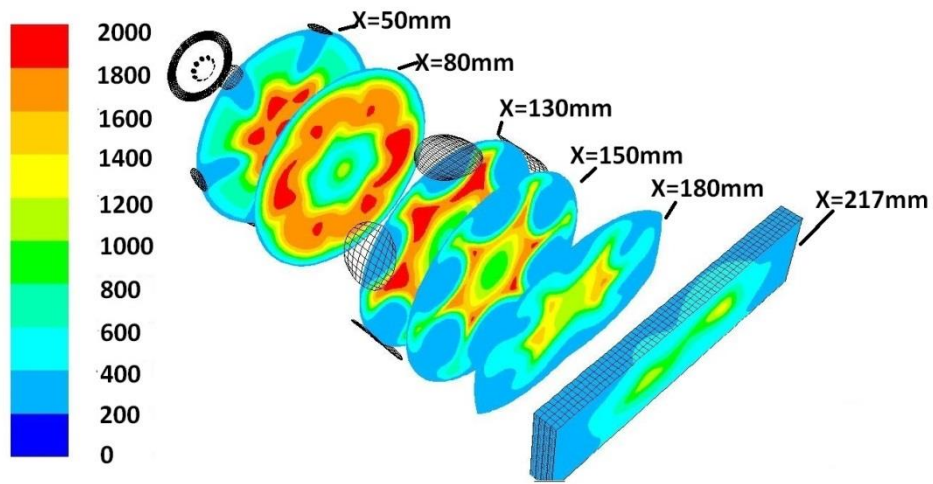


Figure E.2: Time-averaged flame temperature at various plane of combustor (unsteady RSM).

(Note: Blank/White flame region in the cutting plane at X=80mm above indicats that temperature in this region is higher than 2000K)

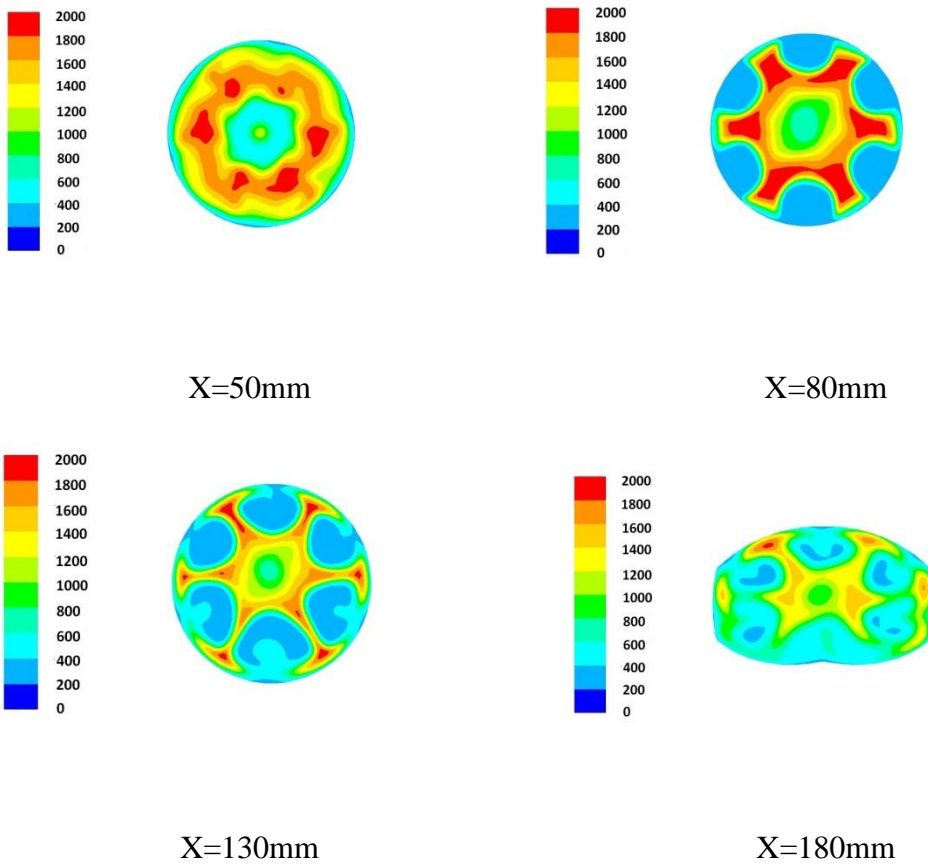
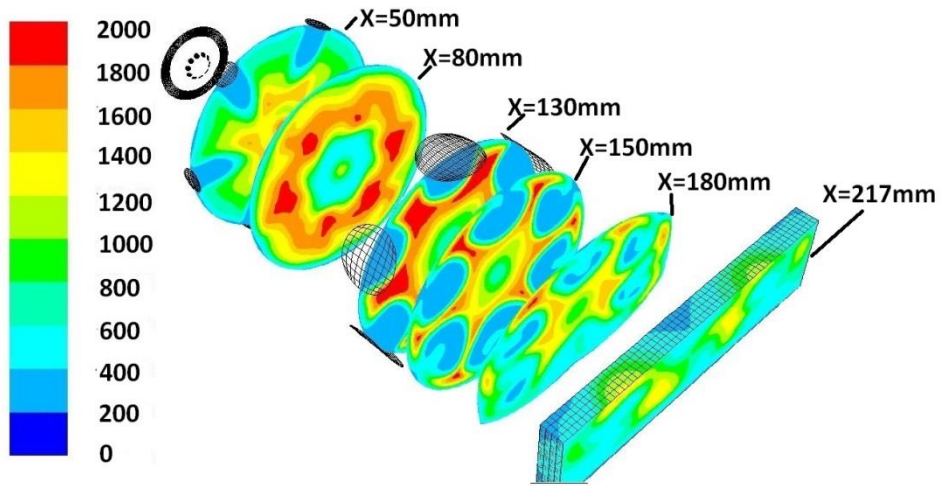
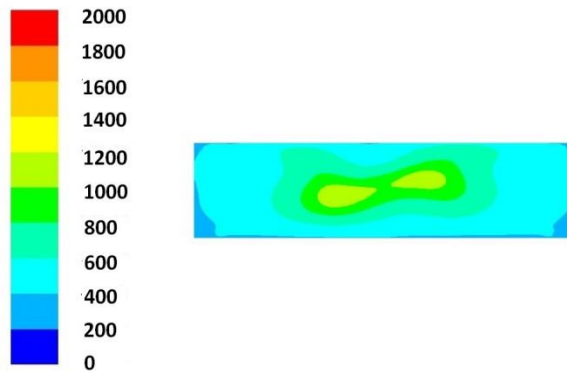
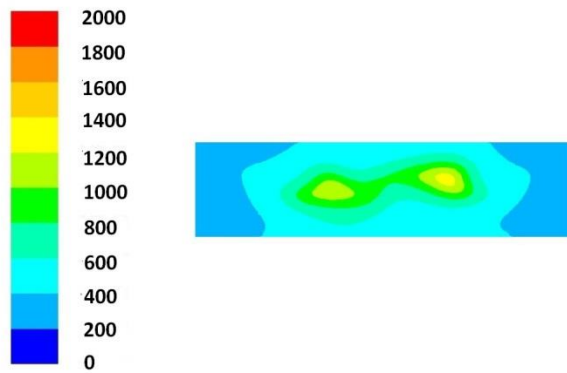


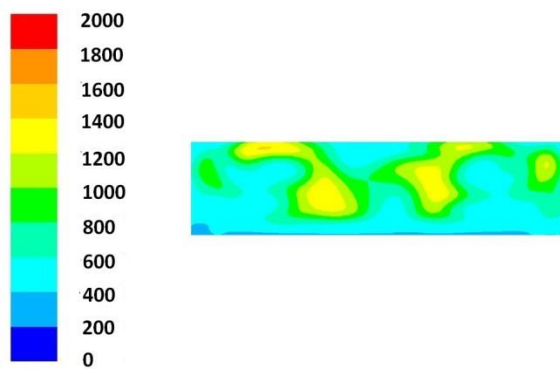
Figure E.3: Time-averaged flame temperature at various plane of combustor (unsteady SSTKWSAS).



(a) Unsteady SSTKW

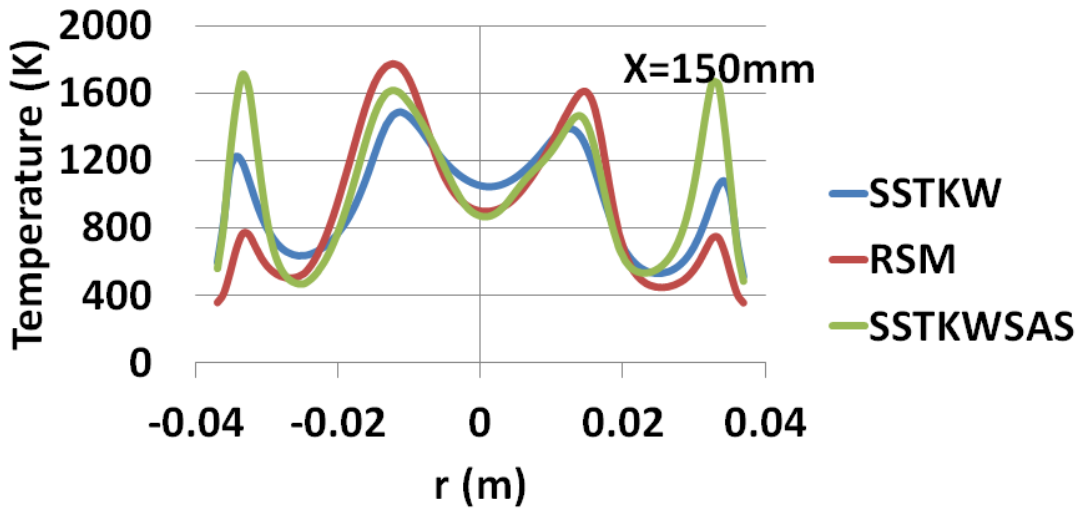


(b) Unsteady RSM

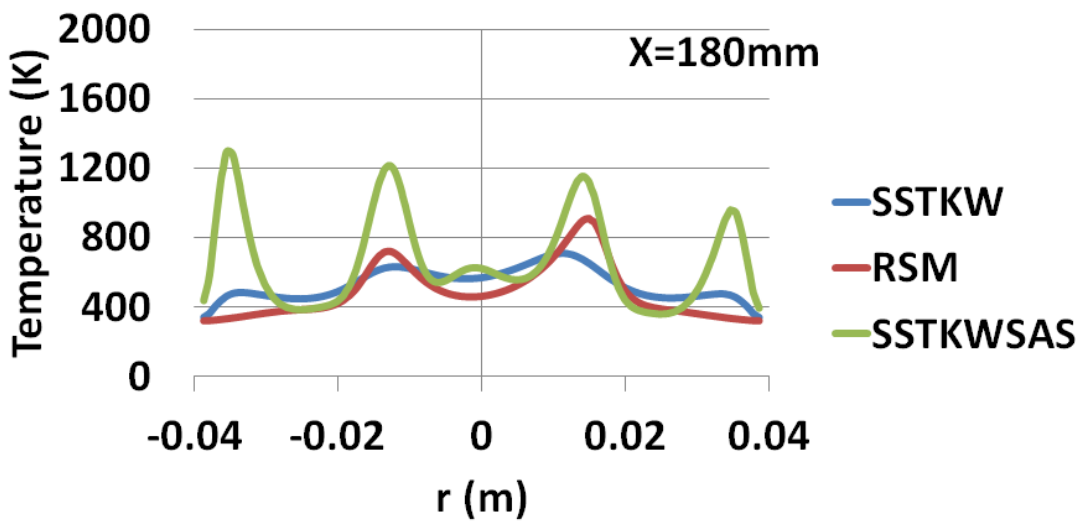


(c) Unsteady SSTKWSAS

Figure E.4: Time-averaged flame temperature at exit of combustor.



(a) X=150mm



(b) X=180mm

Figure E.5: Time-averaged flame temperature comparisons at downstream combustor (near transmission nozzle).